UC San Diego
UC San Diego Electronic Theses and Dissertations

Title
Dynamic Behaviors of Nano-Cellular Silica

Permalink
https://escholarship.org/uc/item/1rq613t6

Author
Zhao, Cang

Publication Date
2015

Peer reviewed|Thesis/dissertation

UNIVERSITY OF CALIFORNIA, SAN DIEGO

Dynamic Behaviors of Nano-Cellular Silica

A dissertation submitted in partial satisfaction of the requirements for the degree

Doctor of Philosophy

in

Structural Engineering

by

Cang Zhao

Committee in charge:

> Professor Yu Qiao, Chair
> Professor Jiun-Shyan Chen
> Professor Hyonny Kim
> Professor Marc A. Meyers
> Professor Vitali F. Nesterenko

2015

The dissertation of Cang Zhao is approved, and it is acceptable in quality and form for publication on microfilm:

_____

_____

_____

_____

_____
Chair

University of California, San Diego

2015

DEDICATION

To my parents

EPIGRAPH

"Life is either a daring adventure or nothing at all."

-- Helen Keller

TABLE OF CONTENTS

LIST OF ABBREVIATIONS

CDZ = cell deformation zone under dynamic indentation

CPG = controlled pore glass

NCM = nano-cellular materials

PEG = polyethylene glycol

PU = polyurethane

PVC = polyvinyl chloride

PVG = porous VYCOR glass

SEM = scanning electron microscope

SiC = silicon carbide

RCM = regular cellular materials

SCC = subcritical calcination of cellular silica monoliths

SDZ = shear deformation zone

SPH = split Hopkinson bar

SPSR = shear-promotion support ring

TC = tungsten carbide

TMOS = tetramethyl orthosilicate

TWC = thick-walled cylinder, used to generate shear localization via geometrical instability

TZ = transition zone under dynamic indentation

XRD = x-ray diffraction

LIST OF SYMBOLS

A	=	cross section area; interface area to volume ratio in the derivation of the Grady Model in the case of SPSR
A_b	=	cross-section area of the Hopkinson bars
c	=	heat capacity; speed of sound
C_b	=	speed of sound of the Hopkinson bars
C_p	=	heat capacity per unit mass
d	=	cell size
D	=	diameter of the moving rod under shear tests
D_1	=	distance between adjacent SEM scanning points
D_{50}	=	median grain size of a granular material
D_r	=	inner diameter of the support ring in SPSR
$E(A)$	=	total energy density in the derivation of the Grady Model in the case of SPSR
E_b	=	Young's modulus of the Hopkinson bars
f	=	a certain function in the dimensional analysis
F	=	measured peak loading at the onset of shear failure under quasi-static shear tests
F_{max}	=	maximum loading under quasi-static indentation
H	=	effective dynamic indentation resistance
H_0	=	effective quasi-static indentation resistance
$\tilde{H}$	=	normalized dynamic indentation resistance
H_{sq}	=	effective quasi-static indentation resistance of solid material
k	=	system constant for CPG approach

K	=	impact energy of the striker
K_{Ic}	=	fracture toughness
L	=	fragment diameter under dynamic loading
m	=	sample mass; system constant for CPG approach
n	=	system constant for CPG approach
p	=	cell volume fraction
p_2	=	nominal two-dimensional cell volume fraction
p_2^*	=	nominal two-dimensional cell volume fraction of a pristine cellular sample
P_{Hg}	=	infiltration pressure of mercury
P_i	=	average incident wave pressure of the Hopkinson bars
P_{t0}	=	equivalent maximum normal stress under quasi-static shear tests, equaling to the maximum force on the loading rod divided by the cross-sectional area
P_{tc}	=	maximum transmitted wave pressure under dynamic compression
P_{ts}	=	maximum transmitted wave pressure under dynamic shearing
P_{w}	=	wave pressure in the Hopkinson bars
r	=	radius of the moving rod under shear tests; radius of indenter;
R	=	indentation radius measured from the indented surface of a cellular or a solid silica sample
S	=	material strength
S_0	=	quasi-static shear strength
t	=	time required for the formation of a shear band; sample thickness
T	=	temperature; temperature in a shear band; pulse duration in the Hopkinson bars, determined by the materials and length of the striker; local kinetic energy density under dynamic shear tests
T'	=	kinetic energy within the shear deformation zone

T_0	=	reference temperature in a shear band
T_g	=	glass transition point of amorphous silica
T_s	=	SCC temperature for cellular silica monoliths
U	=	stress wave energy
U_i	=	energy carried by the incident stress wave
U_k	=	kinetic energy associated with local particle velocity of the Hopkinson bars
U_r	=	energy carried by the reflected stress wave
U_s	=	strain energy associated with local deformation of the Hopkinson bars
U_t	=	energy carried by the transmitted stress wave
v	=	Impact rate of the striker; local velocity at the location of r under dynamic shear tests; specific cell volume of a cellular material
v_0	=	global shear velocity
V	=	volume of a material that undergoes structural changes
V_0	=	initial volume of the material
V_t	=	sample volume
w	=	shear band thickness or width
X	=	strength, toughness or stiffness of a cellular material
X'	=	strength, toughness or stiffness of a nano-cellular material
z	=	acoustic impedance of a cellular silica sample
α	=	system parameter for a cellular material
α_s	=	thermal softening rate
β	=	energy dissipation factor, used to describe the capacity of energy dissipation of a cellular material
γ_0	=	interface energy consumed during the shear localization process

γ_*	=	shear strain inside a shear band
$\dot{\gamma}_*$	=	strain rate inside a shear band
Γ	=	interface energy density
ε	=	strain
$\dot{\varepsilon}$	=	strain rate
θ	=	contact angle of mercury
θ_*	=	temperature rise inside a shear band
λ	=	thermal conductivity inside a shear band; intensity weighted average wavelength of the $K_{\alpha 1}$ and $K_{\alpha 2}$ peaks of XRD
ξ	=	system constant of the SHB system
ρ	=	material density
ρ_b	=	mass density of the Hopkinson bars
ρ_n	=	mass density of solid amorphous silica
σ	=	flow stress; surface tension of mercury
Σ	=	energy dissipation density
τ_*	=	shear stress inside a shear band
χ	=	dimensionless material parameter in the dimensional analysis of the size of the shear deformation zone
ϑ	=	critical local cell volume fraction change ratio, used to define the boundary of the shear deformation zone
$\lvert\varsigma\rvert$	=	pressure reduction factor, used to identify the boundary where the homogenization of a HNHH stress wave starts
ς^+	=	maximum transmitted wave pressure is higher than P_{t0}; used to define the Regular Region of cellular materials
ς^-	=	maximum transmitted wave pressure is lower than P_{t0}; used to define the Nano Region of cellular materials

LIST OF FIGURES

LIST OF TABLES

ACKNOWLEDGEMENTS

Tzehan Chen, Mr. Brian J. Chow, Mr. Meng Wang, Mr. Daniel Noelle, and Mr. Kiwon Oh and Mr. Jacky Cheung. Dr. Aijie Han was instrumental in the introduction to the cellular materials; Dr. Weiyi Lu assisted on the modification of the Hopkinson bar system; Dr. Gang Wang provided assistance on the processing of porous polymer materials; Mr. Brian J. Chow helped when I had trouble in English, cultural and social issues.

Words cannot express my thanks to my father Liufa Zhao, my mother Tianni Shang, and my sister Dongge Zhao for their unconditional love and encouragement.

Chapter 2, in part, has been submitted for publication in Materials & Design, and co-authored by Meng Wang, Yang Shi, Jianguo Cao, and Yu Qiao. The dissertation author was the primary investigator and author of this work.

Chapter 4, in part, is currently being prepared for submission for publication of the material, and co-authored by Yu Qiao. The dissertation author was the primary investigator and author of this work.

Chapter 5, in part, has been submitted for publication in Physical Review Letters, and co-authored by Meng Wang, Yang Shi, Jian Luo, and Yu Qiao; in part, is currently being prepared for submission for publication of the material, and co-authored by Yu Qiao. The dissertation author was the primary investigator and author of this work.

Chapter 6, in part, has been submitted for publication in Nature, and co-authored by Yu Qiao; in part, is currently being prepared for submission for publication of the material, and co-authored by Yu Qiao. The dissertation author was the primary investigator and author of this work.

VITA

01/2012-09/2015   University of California, San Diego (UCSD)
                  Ph.D. in Structural Engineering, 2015

09/2009-12/2011   University of Science and Technology of China (USTC)
                  M.S. in Condensed Matter Physics, 2011

09/2005-07/2009   University of Science and Technology Beijing (USTB)
                  B.S. in Material Science and Engineering, 2009
                  Bachelor of Financial Engineering (Minor), 2009

FIELDS OF STUDY

Major: Material Science and Engineering; Condensed Matter Physics;
              Structural Engineering

Minor: Financial Engineering

LIST OF PUBLICATIONS

Lim, H., Zhao, C., Qiao, Y., 2014. Performance of thermally-chargeable supercapacitors in different solvents. Physical Chemistry Chemical Physics 16, 12728-12730.

Zhao, C., Wang, M., Shi, Y., Cao, J., Qiao, Y., Accepted. High-temperature post-processing treatment of silica nanofoams of controlled pore sizes and porosities. Materials & Design.

Zhao, C., Wang, M., Shi, Y., Luo, J., Qiao, Y., Submitted. Homogenization of Highly Nonlinear, Highly Heterogeneous Stress Wave in Fast-Condensing Cellular Medium. Physical Review Letters.

Zhao, C., Qiao, Y., Submitted. Nanocellular silica harder than solid silica under dynamic loading. Nature.

Zhao, C., Qiao, Y., In preparation. Quantitative SEM Image Analysis of Nanofoams.

Zhao, C., Qiao, Y., In preparation. Loading Rate Effects on Stress-Wave Mitigation

Properties of Silica Nanofoams.

Zhao, C., Qiao, Y., In preparation. Cell Volume Fraction Effects on Stress-Wave Mitigation Properties of Silica Nanofoams.

Zhao, C., Qiao, Y., In preparation. Loading Rate Effects on the Indentation Resistance of Silica Nanofoams.

Zhao, C., Qiao, Y., In preparation. Cell Volume Fraction Effects on the Indentation Resistance of Silica Nanofoams.

Zhao, C., Qiao, Y., In preparation. Diagram of Cell Size Effects in Silica Nanofoams.

ABSTRACT OF DISSERTATION

Dynamic Behaviors of Nano-Cellular Silica

by

Cang Zhao

Doctor of Philosophy in Structural Engineering

University of California, San Diego, 2015

Professor Yu Qiao, Chair

The dynamic behaviors of cellular silica were experimentally investigated. The factors of cell size, cell volume fraction, strain rate, and loading mode were analyzed systematically. Under dynamic shearing, the shear localization in nano-cellular silica could be significantly suppressed. Under dynamic indentation, the effective indentation resistance of nano-cellular silica could be higher than that of solid silica. These unique phenomena of nano-cellular silica could be attributed to the local hardening caused by the fast compaction of the small cells.

Based on dimensional and theoretical analyses, two models were developed to describe the cell size effect on the deformation zone size in dynamic shearing and on the

effective indentation resistance in dynamic indentation, respectively. They agree well with the experimental results. A diagram of cell size effect, accounting for the three factors of cell size, cell volume fraction, and kinetic energy, was drawn to distinguish the nano-cellular materials from the regular cellular materials.

CHAPTER 1

INTRODUCTION

1.1.   Project Motivation

Dynamic behavior of materials has been extensively investigated for decades (Achenbach, 2012; Clifton, 1983; Clifton, 1974; Daraio et al., 2005; Davison and Graham, 1979; Dodd, 1992; Field et al., 2004; Kinslow, 2012; Kolsky, 1963; Lu and Yu, 2003; Meyers, 1994; Meyers and Murr, 1981; Nesterenko et al., 2005a; Nesterenko, 2001; Zukas, 1982). Two comprehensive books, "Dynamic Behavior of Materials" written by Professor Marc Meyers (1994) and "Dynamics of Heterogeneous Materials" written by Professor Vitali Nesterenko (2001), well summarized the previous results for metallic, ceramic, granular, and porous materials.

When a material is subjected to a high-strain-rate loading, the material responses can be significantly different from those under quasi-static conditions (Meyers, 1994). A

few classic examples were discussed in the book of Meyers (1994): A sand bag can capture a bullet, but cannot withstand a stab; a solid steel plate can be penetrated by a bullet, but never by a knife. Under dynamic loadings, materials respond to external forces through mechanisms that involve dislocation generation and motion, twinning, phase transformation, fracture, viscous glide of polymer chains, among others (Meyers and Chawla, 2009). Based on experimental observations, a couple of empirical and semi-empirical models were developed to predict the flow stress of strain-rate dependent materials, such as the Johnson-cook model (Johnson and Cook, 1983), the Klopp model (Klopp et al., 1985), the Meyers model (Meyers et al., 1994), and the Andrade model (Andrade et al., 1994). In general, the flow stress (Meyers and Chawla, 2009)

$$\sigma = f(\varepsilon, \dot{\varepsilon}, T, deformation\ history) \tag{1.1}$$

where ε is the strain, $\dot{\varepsilon}$ is the strain rate, T is the temperature, and f represents a certain function.

Compared with homogeneous materials, the microstructural effects in highly heterogeneous materials are critical under intense dynamic loadings (Nesterenko, 2001). In one study, thick-walled cylinder (TWC) method (Nesterenko, 1994; Nesterenko et al., 1989; Nesterenko et al., 1997; Nesterenko et al., 1994b; Xue et al., 2003) was developed to investigate the shear behaviors of granular silicon carbide (SiC) and pre-fractured SiC. The results show that the shear band spacing in granular SiC is much smaller than that in pre-fractured SiC (Shih et al., 1998a; Shih et al., 1998b).

While dynamic responses of solid and granular materials have received considerable attention and earlier efforts have brought about a sound understanding of many fundamental issues (Balch et al., 2005; Carretero-González et al., 2009;

Dannemann and Lankford, 2000; Daraio et al., 2005; Daraio et al., 2006; Dauchot et al., 2005; Deshpande and Fleck, 2000; Meyers et al., 2001; Nesterenko et al., 2005a; Nesterenko, 2001; Sen et al., 2008; Tan et al., 2005; Xue et al., 2002), more research needs to be conducted on cellular materials, particularly nano-cellular materials with the cell sizes on the nanometer (nm) or sub-micron (μm) scale.

Much of the attention of earlier work on cellular materials has been paid to quasi-static conditions, and the cell sizes were typically at the microscopic or millimeter (mm) level (Dannemann and Lankford, 2000; Deshpande and Fleck, 2000; Gibson and Ashby, 1999; Meyers and Chawla, 2009; Queheillalt and Wadley, 2005; Scheffler and Colombo, 2006). Physically speaking, a cellular material is characterized by two major parameters: the cell size (d) and the cell volume fraction (p). According to classic theory, under a quasi-static loading, the material behavior is only related to the cell volume fraction and independent of the cell size (Gibson and Ashby, 1982; Gibson and Ashby, 1997)

$$X \propto (1 - p)^{\alpha} \qquad (1.2)$$

where X could be the stiffness, the strength, the hardness, or the toughness of a cellular material, and α is a system constant. The increase in the cell volume fraction tends to weaken the materials.

As mentioned at the beginning of this chapter, the dynamic and the quasi-static behaviors of a material could differ significantly. Moreover, in Equation (1.2), the factor of cell size, as one of the two most critical parameters of a cellular material, does not show up, indicating that there must be something missing. The motivation of this work is to systematically investigate the dynamic behaviors of nano-cellular materials, and to shed light on developing advanced projectile protection and shock mitigation materials.

1.2. Literature Review

1.2.1. Shear Localization

Due to the long and flat plateaus in stress-strain curves, cellular materials, such as foams and honeycombs, are often used for protection against impact and/or shock loadings (Gibson and Ashby, 1999; Meyers and Chawla, 2009; Scheffler and Colombo, 2006). Under compression loadings, they can dissipate a considerable portion of the input energy (Balch et al., 2005; Dannemann and Lankford, 2000; Deshpande and Fleck, 2000; Tan et al., 2005); however, under shearing especially dynamic shearing, the energy dissipation tends to occur in a number of narrow bands, with the majority of the protection capacity of the materials being essentially wasted. Currently, dynamic shearing in foams and honeycombs is relatively under-investigated.

A.   Definition of Shear Band

A shear band is a thin layer in between two parallel discontinuity surfaces of velocity gradient (Hill, 1962; Rice, 1976). The distance between the two discontinuity surfaces is defined as the shear band thickness or width (Mühlhaus and Vardoulakis, 1987; Roscoe, 1970). In the framework of the classical continuum mechanics, there is no internal length scale associated with the thickness of shear band (Bardet and Proubet, 1992; Mühlhaus and Vardoulakis, 1987; Tejchman and Wu, 1993). Yet in general, shear

band thickness is on the microscopic scale (Dodd and Bai, 2012; Hutchinson, 2000; Mühlhaus and Vardoulakis, 1987; Meyers et al., 2001).

B.   Initiation of Shear Localization

Shear localization can be caused by either material instability or geometrical instability (Nesterenko, 2001). For the material instability, in ductile materials, such as metals and polymers, it is associated with thermal softening under high strain and high strain rate (Bai, 1981; Bai et al., 1994; Culver, 1973; Dodd, 1992; Fressengeas and Molinari, 1987; Meyers, 1994; Meyers et al., 2001; Poirier, 1980; Recht, 1964; Semiatin et al., 1984; Xu et al., 2001; Zener and Hollomon, 1944; Zurek, 1994); while in hard materials, such as boron carbide (BC) and metallic glass, recent researches suggested stress-driven mechanisms (Argon, 1979; Falk and Langer, 1998; Huang et al., 2002; Ketov and Louzguine-Luzgin, 2013; Reddy et al., 2013; Spaepen, 1977, 2006; Wright et al., 2003). For the geometrical instability, shear localization is related to geometry changes of testing samples or setups which may be promoted by hat-shaped sample (Hartmann et al., 1981; Meyer et al., 1994; Meyers et al., 1992; Meyers et al., 2003; Nesterenko, 2001; Xu et al., 2008) and thick-walled cylinder (TWC) techniques (Nesterenko, 1994; Nesterenko et al., 1989; Nesterenko et al., 1997; Nesterenko et al., 1994b; Xue et al., 2003), as shown in Figure 1.1. The two mechanisms, material instability and geometrical instability, may accompany with each other (Nesterenko, 2001).

C.   Evolution of Shear Localization

The evolution of shear localization was a gradual process in a number of metals, such as steel, Ti-6Al-4V alloy, etc. (Bai et al., 1994; Marchand and Duffy, 1988; Nesterenko et al., 1997; Xu et al., 2001). In Figure 1.2, a series of interrupted tests were performed on Al-Li alloy with the average strain rate of ~2250 s^{-1} (Xu et al., 2001). When the strain is ~0.10, the deformation appeared to be homogeneous, and there was no shear localization, as shown in Figure 1.2 (a); when the strain increased to 0.17, localized deformation occurred, as shown in Figure 1.2 (b); when the strain continued to increase, the localization became more pronounced, as shown in Figure 1.2 (c); eventually, a narrow shear band was formed, as shown in Figure 1.2 (d).

Shear localization of granular materials under dynamic loadings is of different characteristics. As shown in Figure 1.3, with the increase of shear strain, mainly through internal friction the particles comminute, rearrange and rotate, promoting the growth of shear bands (Meyers et al., 2001; Nesterenko, 2001; Shih et al., 1998a; Shih et al., 1998b). Since the granular material is porous, the local comminution and rearrangement are sufficient to accommodate the large shear strain, resulting in a regular shear band structure (Nesterenko, 2001; Shih et al., 1998b).

D.   Characteristic Length Scale of Shear Localization

As shear banding occurs, the external energy is dissipated only in a number of narrow bands; the energy dissipation is closely related to the thickness and the number of the shear bands. Typically, the thickness of a shear band in metals is 10-100 μm, and is

~10 nm in bulk metallic glass (Dodd and Bai, 2012; Donovan and Stobbs, 1981; Jiang et al., 2009; Jiang and Atzmon, 2006; Kim et al., 2008; Masumoto and Maddin, 1971; Pekarskaya et al., 2001). Selected data of shear band thicknesses of various materials are listed in Table 1.1. In silica sands with the average grain size in the range of 0.22-1.60 mm, the shear band thickness (w) is proportional to D_{50} (Alshibli and Sture, 1999),

$$w \propto D_{50} \tag{1.3}$$

However, as the grain size further reduces, the shear band thickness converges. In granular SiC, when the grain size varies from 50 μm to 0.4 μm, the shear band thickness changes only slightly (Meyers et al., 2001; Shih et al., 1998a); in granular Al_2O_3, as the grain size changes from 4 μm to 0.4 μm, the shear band thickness remains at about 10 μm (Meyers et al., 2001; Nesterenko et al., 1996).

Theoretically, to estimate the thickness of an adiabatic shear band under confined stresses, Dodd and Bai developed an empirical equation (Dodd and Bai, 1989)

$$w = 2 \left(\frac{\lambda \theta_*}{\tau_* \dot{\gamma}_*} \right)^{1/2} \tag{1.4}$$

where λ is the thermal conductivity, θ_* is the temperature rise inside the band, σ_* is the shear stress, and $\dot{\gamma}_*$ is the strain rate. The temperature rise can be obtained by assuming that 90% of the deformation work is transformed into heat

$$\theta_* = \frac{0.9 \tau_* \gamma_*}{\rho c} \tag{1.5}$$

where γ_* is the strain, ρ is the material density, and c is the heat capacity. Combining Equations (1.4) and (1.5), the time required for the formation of shear band can be obtained as

$$t = \frac{\gamma_*}{\dot{\gamma}_*} = \frac{\rho c}{3.6\lambda} w^2 \tag{1.6}$$

Equation (1.4) does not contain a thermal softening term. Grady assumes a linear relationship between the flow stress and the relative temperature (Grady, 1992, 1994; Grady and Kipp, 1987)

$$\tau_* = \tau_0 (1 - \alpha_s \theta_*) \tag{1.7}$$

where τ_0 is the strength at a reference temperature T_0, α_s is the thermal softening rate, and θ_* is the relative temperature $T - T_0$ inside the band. He then gives a modified equation of the shear band thickness

$$w = \left(\frac{9\rho^3 C_p^2 \lambda^3}{\tau_*^3 \alpha_s^2 \dot{\gamma}_*} \right)^{1/4} \tag{1.8}$$

where C_p is the heat capacity per unit mass.

For brittle materials under dynamic loading, based on the equilibrium condition of kinetic energy and surface energy, as shown in Figure 1.4, Grady (Grady, 1982; Grady and Olsen, 2003) developed an analytical model to predict the nominal fragment diameter (L).

$$L \propto \left(\frac{K_{Ic}}{\rho c \dot{\varepsilon}} \right)^{2/3} \tag{1.9}$$

where K_{IC} is the fracture toughness; ρ is the mass density; c is the speed of sound; and $\dot{\varepsilon}$ is the strain rate. Grady (Grady, 1982) extended this concept to uniform one-dimensional shear deformation. If the fracture area is interpreted as the interface area of the shear bands, γ is the interface energy consumed during the shear banding process, and w is the thickness of shear band:

$$w \propto \left(\frac{\gamma}{\rho\dot{\varepsilon}^2}\right)^{1/3} \qquad (1.10)$$

Furthermore, it is assumed that all the energy dissipation occurs in the shear bands; the energy dissipation density (Σ) can be estimated as

$$\gamma = \Sigma \cdot w \qquad (1.11)$$

Combination of Equations (1.10) and (1.11) leads to

$$w \propto \sqrt{\frac{\Sigma}{\rho\dot{\varepsilon}^2}} \qquad (1.12)$$

This model captures the effects of strain rate and the resistance to shear (Shih et al., 1998a). More importantly, it provides an approach to group physical parameters (Nesterenko, 2001).

1.2.2. Cellular Materials

Cellular materials are referred to as assembly of cells with solid ligaments (Gibson and Ashby, 1997). When the cells pack in two dimensions, the materials are called honeycombs; when the cells are in the form of three-dimension arrays, they are called foams. In this thesis, we focus on monolithic foams. The two most critical parameters of a cellular material are the average cell size (d) and the cell volume fraction (p). Cellular materials can be made of polymers, metals/alloys, and/or ceramics (Hedrick et al., 1999; Nakanishi, 2010; Tappan et al., 2010). They are widely used in packaging, thermal/acoustic insulation, protection and damping, energy storage, and chemical engineering systems, due to their unique micro-structures and properties (Asefa et al.,

2009; Ashley et al., 2011; Lee et al., 2010; Md Jani et al., 2013; Misra et al., 2009; Rahman et al., 2014; Schmid et al., 1999).

A.   Cellular Ceramics

Commonly used cellular ceramics include silica (SiO_2), alumina (Al_2O_3), etc. Here we focus on cellular silica. The processing techniques of cellular silica have been well developed (Brinker and Scherer, 1990). They can be processed through CPG, sol-gel method, templating, to name a few (Elmer, 1991; Haller, 1965; Kiefer and Sura, 1986; Miyamoto et al., 2013; Nakanishi, 2010; Reinhardt et al., 2012; Shoup, 1976). As shown in Table 1.2, the cell size can span from a few nm to hundreds of microns. In the CPG approach, the cell size can be controlled via changing the heat treatment time and temperature (Schnabel and Langer, 1991; Wolfgang, 1970)

$$d^n = k \cdot t \cdot e^{-m/T} \tag{1.13}$$

where d is the cell size (Å); T is the temperature of heat treatment (K); t is the time of heat treatment (hr); and k, m, n are system constants. In the sol-gel methods, the cell size is mainly tailored via changing the mass ratio of PEG to TMOS or colloidal silica to potassium silicate (Nakanishi, 2010; Shoup, 1976); a larger PEG or colloidal silica amount would lead to a smaller cell size. In the templating method, the cell size is mainly controlled by the initial grain size of inorganic salt (Kiefer and Sura, 1986; Reinhardt et al., 2012). Compared with the approaches of CPG and templating, sol-gel methods help to improve uniformity of cellular silica samples; the so-produced cell size can span from tens of nm to a few microns.

B.   Cellular Polymers

Cellular polymers with the average cell sizes ranging from tens of nm to a few microns to a fraction of mm can be synthesized via co-polymering, gas dissolution foaming, extrusion, etc. (Hedrick et al., 1999; Kanazawa et al., 2010; Pinto et al., 2014; Svec and Frechet, 1995). Selected data of cellular polymers are listed in Table 1.3. The green background indicates a similar cell volume fraction but different average cell sizes.

C.   Cellular Metals

Cellular metals with the average cell sizes varying from tens of nm to a few microns may be synthesized by using platinum, gold, copper, etc., through dealloying, templating, nanosmelting, combustion synthesis, among others (Hayes et al., 2007; Nyce et al., 2007; Tappan et al., 2010; Vukovic et al., 2013). Selected data of cellular metals are listed in Table 1.4.

1.3.   Objective and Approach

The objective of the current study is to experimentally investigate the dynamic behaviors of cellular materials. It is expected to observe some unique phenomena, and apply these unique phenomena on impact protection. As mentioned in Section 1.1, we need to find the missing part, the role of the cell size in the material behaviors. To achieve these, a Split Hopkinson Bar (SHB) system will be built up to conduct dynamic

tests; the investigated materials are chosen to be cellular silica. The parameters under investigation include: the cell size (d) and the cell volume fraction (p) of cellular silica, the strain rate ($\dot{\varepsilon}$), and the loading mode (shear verses compression). The properties of cellular material (X') can be written as

$$X^{'} = f(d, p, \dot{\varepsilon}, loading\ mode) \tag{1.14}$$

where the cell size will range from tens of nm to a few microns; the cell volume fraction will vary from ~50% to ~70%; the strain rate is related with the impact rate of the striker; and the loading mode will include compression, shearing and indentation.

Chapter 2 describes the subcritical calcination (SCC) technique that we developed to precisely and independently control the cell size and the cell volume fraction. Chapter 3 provides the details of the testing conditions: Section 3.1 describes the SHB system; Section 3.2 describes the shear promotion support ring (SPSR) system; Section 3.3 describes the indentation system. Chapter 4 describes the quantitative image analysis technique, which we developed to connect the dynamic behaviors of cellular silica samples to the changes in the cell structures.

Chapter 5 presents the results of dynamic shearing of cellular silica. In Section 5.1-5.4, the cell volume fraction and the shear strain rate are nearly constant, and the only variable is the cell size. In Section 5.5, the cell volume fraction is nearly constant, and for a specific cell size, the only variable is the shear strain rate. In Section 5.6, the shear strain rate is nearly constant, for a specific cell size, the only variable is the cell volume fraction. In Section 5.7-5.8, a modified version of Grady model is derived.

Chapter 6 discusses the results of dynamic indentation of cellular silica. In Section 6.1-6.4, the cell volume fraction and the shear strain rate are nearly constant, and

the only variable is the cell size. In Section 6.5, the cell volume fraction is nearly constant, and for a specific cell size, the only variable is the strain rate. In Section 6.6, the cell size and shear strain rate are nearly constant, and the only variable is the cell volume fraction. In Section 6.7, a model is built up to characterize the dynamic indentation behaviors of cellular silica. In Section 6.8, a diagram of the cell size effect is drawn to distinguish nano-cellular materials from regular cellular materials.

Finally, Chapter 7 presents the summary and our conclusions.

Table 1.1: Shear band thicknesses of various materials

	Materials	Shear band thickness	Source
Metal	Low C steel	0.13-0.17 mm	(Dodd and Bai, 2012)
	Tool steel	0.1 mm	
	Ti alloy	0.06-0.1 mm	
	Cu alloy	0.34 mm	
	C steel	0.19 mm	
Granular materials	Al_2O_3 (0.4 μm and 4 μm)	~10 μm	(Nesterenko et al., 1996)
	SiC (0.4 μm, 3 μm and 50 μm)	(15 μm, 25 μm and 40 μm)	(Shih et al., 1998a)
	Ultra-fine copper grains (200-500 nm)	~60 μm	(Mishra et al., 2008)
	Sand (0.22 mm, 0.55 mm, 1.60 mm)	~10 d_{50}	(Alshibli and Sture, 1999)
Pre-fractured materials	SiC	150 μm	(Shih et al., 1998a)
Metal glass	$Pd_{80}Si_{20}$	20 nm	(Masumoto and Maddin, 1971)
	$Fe_{40}Ni_{40}B_{20}$	10-20 nm	(Donovan and Stobbs, 1981)
	$Zr_{56.3}Ti_{13.8}Cu_{6.9}Ni_{5.6}Nb_{5.0}Be_{12.5}$	$\leq$ 10 nm	(Pekarskaya et al., 2001)
	$Al_{90}Fe_5Gd_5$; $Al_{86.8}Ni_{3.7}Y_{9.5}$	10-15 nm	(Jiang and Atzmon, 2006)
	$Cu_{47.5}Zr_{47.5}Al_5$	~10 nm	(Kim et al., 2008)

Table 1.2: List of cellular glass reported in the literature

Approaches		Cell size	Cell volume fraction	Highest treatment temperature	Source
Phase-separated alkali borosilicate glasses	Porous VYCOR glass (PVG)	<6 nm	<40%	~1500 °C	(Elmer, 1991)
	Controlled pore glass (CPG)	7.5-400 nm	50%-70%	~1500 °C	(Haller, 1965; Scheve, 1982; Schnabel and Langer, 1991; Wolfgang, 1970)
Sol-gel process	PEG-TMOS	500 nm-10 µm	85%-90%	~100 °C	(Miyamoto et al., 2013; Nakanishi, 2010)
	Silica-silicate	50-300 nm	80%-85%	~100 °C	(Shoup, 1976; Shoup and Wein, 1980)
Templating	Sodium borosilicate glass-inorganic salt	20-150 µm	40%-74%	~ 1500 °C	(Kiefer and Sura, 1986; Reinhardt et al., 2012)

Table 1.3: List of cellular polymers reported in the literature

No.	Materials	Cell size	Specific cell volume (cm³/g)	Source
1	Poly(glycidyl methacrylate-co-ethylene dimethacrylate)	0.47-1.9 um		(Chambers et al., 2011b) (Chambers et al., 2011a)
2	BMA and PEGDA	0.71 um		(Fang et al., 2010)
3	Butyl methacrylate (BMA) and glycidyl methacrylate (GMA)	0.1-1 um	63-75% (cell volume fraction)	(Xin et al., 2010)
4	Enzyme immobilization	140-2900 nm		(Vlakh and Tennikova, 2013)
5	Glycidyl methacrylate (GMA) and ethylene dimethacrylate	0.25 um		(Yang et al., 2005)
6	M41S	1.5-10 nm		(Barton et al., 1999)
7	Metal organic framework polymer	0.2-1.3 um		(Huang et al., 2013)
8	Methacrylate	0.4 um		(Danquah and Forde, 2008)
9	Poly(ethyleneglycol) diacrylate	0.48-1.1 um	2.4-3.4	(Dario Arrua et al., 2013)
10	Poly(glycidyl methacrylate-co-ethylene dimethacrylate)	50-1700 nm	1.23-1.58	(Svec and Frechet, 1995)
11	Poly(N-isopropylacrylamide)	4.8-10 um	3.5-5.8	(Grant et al., 2010)
12	Poly(styrene-co-divinylbenzene)	20 um, 1-4 um	2.4, 1.5	(Peters et al., 1997)
13	Polyacrylamide	50-1000 nm	1.43-1.51	(Xie et al., 1997)
14	Polymethacrylate	0.6-3.8 um	1.2-1.9	(Nordborg et al., 2005)
15	Polystyrene	4-19 um	0.21-1.68	(Nevejans and Verzele, 1985)
16	PS-DVB	0.1 um		(Penner et al., 1999)

Table 1.4: List of cellular metals reported in the literature

No.	Materials	Cell size	Source
1	Ag	1-2 um	
2	Au	1-3 um	
3	Ni	~300 nm	
4	Cu/Co/Ag	1-2 um	(Tappan et al., 2006; Tappan et al., 2010)
5	Pd	100-200 nm	
6	Pt	10-200 nm	
7	Ti	~400 nm	
11	Au	5-126 nm	(Hakamada and Mabuchi, 2007)
12	Ag	150-350 nm	(Du and Kang, 2008)
13	Ag	10 um	(Walsh et al., 2003)
16	Ag	25 nm	
17	Cu	60-100 nm	(Cheng and Hodge, 2013)
18	Pd	30 nm	
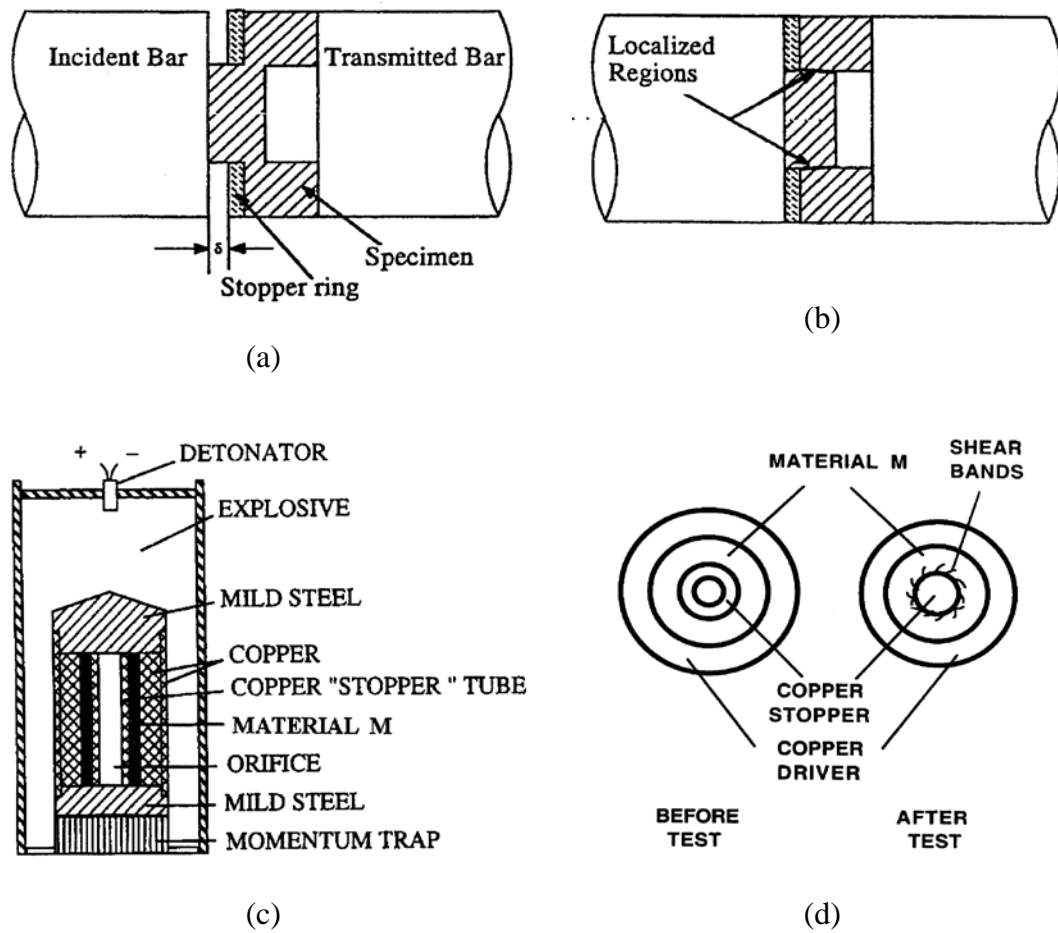
Figure 1.1: Two experimental techniques causing shear localization via geometrical instability mechanisms under high-strain-rate loadings. (a) Initial and (b) final hat-shaped specimen; (c) thick-walled cylinder method; (d) initial and final configurations of thick-walled cylinder specimen (Meyers et al., 2001; Nesterenko, 2001).
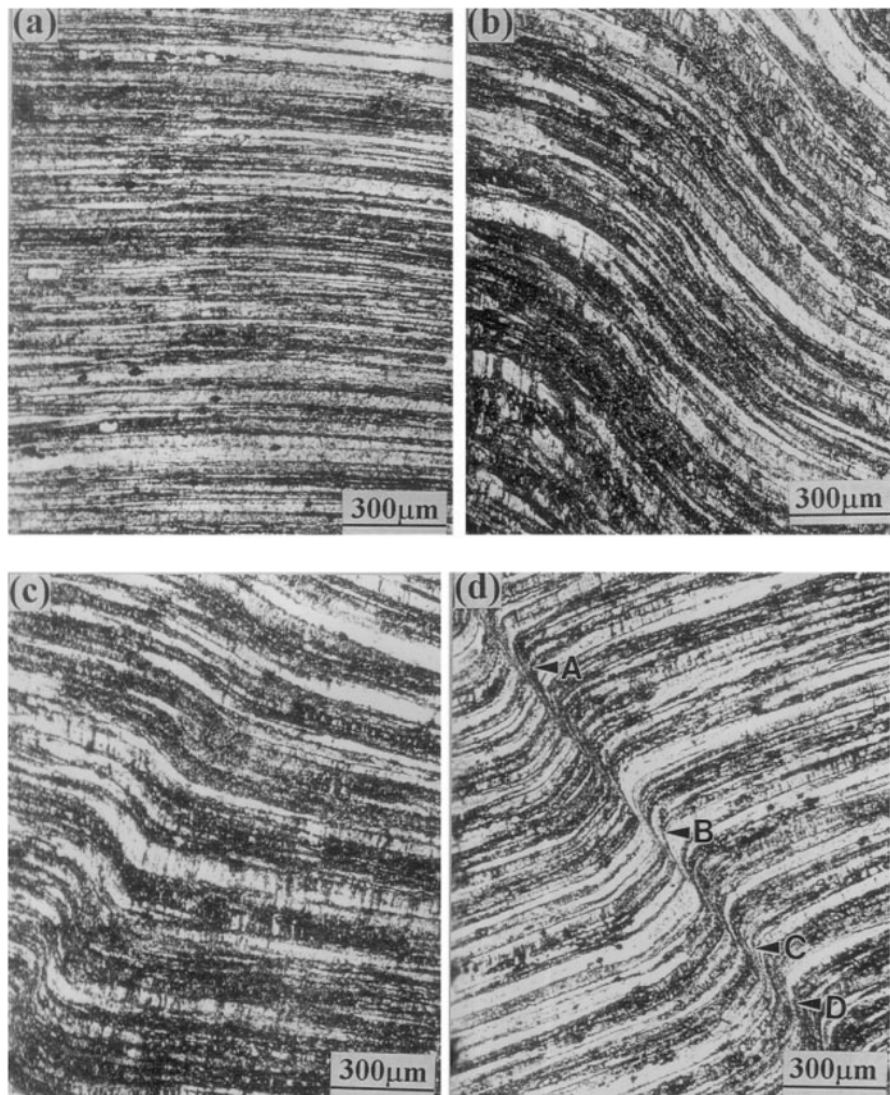
Figure 1.2: Evolution of localized deformation in Al-Li alloy as strain is increased under the strain rate of ~2250 s^{-1} (Nesterenko et al., 1997; Xu et al., 2001).

Medium powder

Coarse powder
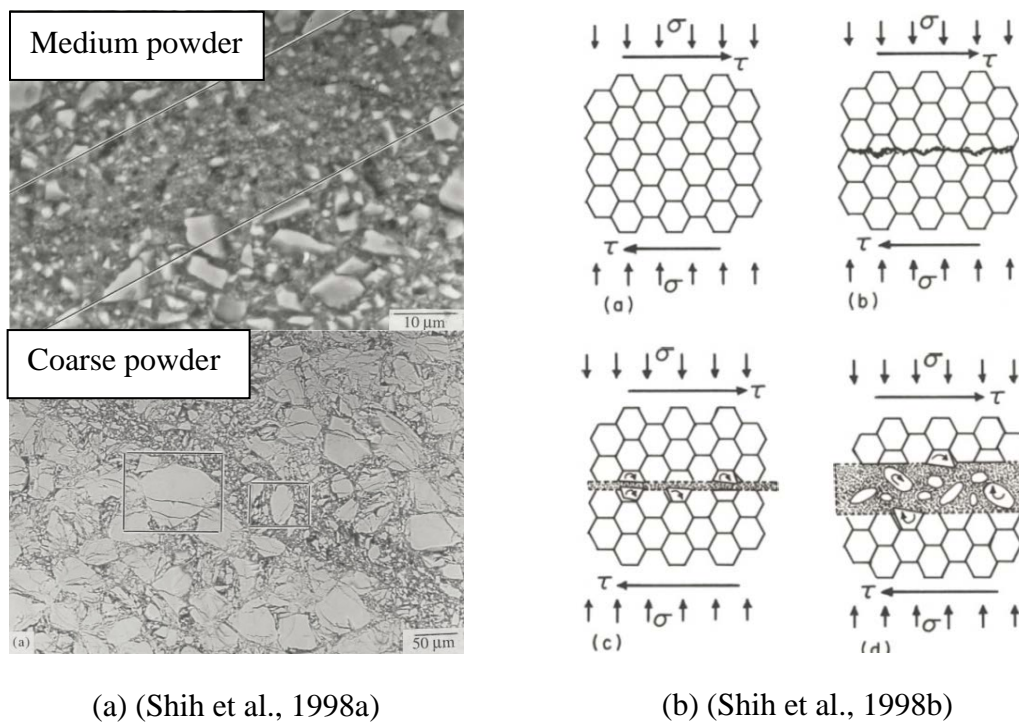
(a) (Shih et al., 1998a)   (b) (Shih et al., 1998b)

Figure 1.3: High-strain-rate deformation of granular SiC. (a) Microstructure of shear bands. (b) Diagram of shear-band formation.
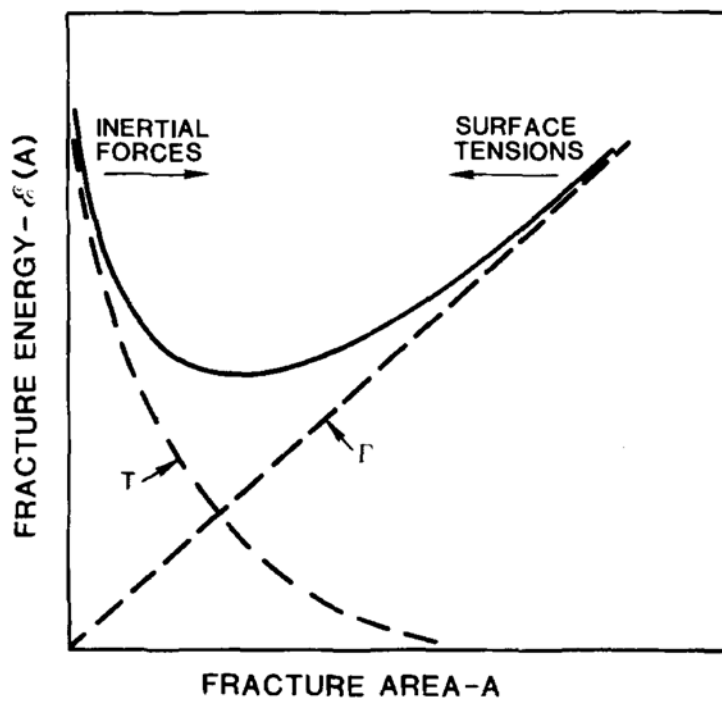
Figure 1.4: Grady model for dynamic fragmentation (Grady, 1982). The terms of kinetic energy and surface energy determine the conditions of equilibrium fragmentation.

CHAPTER 2

PROCESSING OF CELLULAR SILICA

2.1. Introduction

Cellular materials are widely used in packaging, thermal/acoustic insulation, protection and damping, energy storage, and chemical engineering systems (Asefa et al., 2009; Ashley et al., 2011; Lee et al., 2010; Md Jani et al., 2013; Misra et al., 2009; Rahman et al., 2014; Schmid et al., 1999). A cellular material may be in particle form, in membrane form, or in monolithic form.

Processing techniques of cellular silica have been well developed (Brinker and Scherer, 1990). Their average cell sizes could be reduced to a few nm (Levitz et al., 1991), and their cell volume fractions could be increased to more than 90% (Schmidt and Schwertfeger, 1998). They can be processed through phase separation of alkali borosilicate glasses, sol-gel method, and templating (Elmer, 1991; Haller, 1965; Kiefer and Sura, 1986; Miyamoto et al., 2013; Nakanishi, 2010; Reinhardt et al., 2012; Shoup,

1976). Compared with the approaches of CPG and templating, sol-gel methods help to improve uniformity of cellular silica samples; the so-produced cell size can span from tens of nm to a few microns. However, a major problem is that, as the cell size is adjusted by changing the ratios of different components, it would inevitably affect the cell volume fraction (Nakanishi, 1997; Shoup, 1976; Tokudome et al., 2007). In another word, the cell size and the cell volume fraction are coupled. As shown in Figure 2.4 (a), the cellular silica samples synthesized via Shoup's method (Shoup, 1976) have a wide range of average cell size; the silica with the cell size of ~300 nm has a cell volume fraction of ~76% (density ~0.52 g/cm^3); while the silica with the cell size of ~50 nm has a cell volume fraction of ~86% (density ~0.32 g/cm^3).

Based on a unique phenomenon that when the treatment temperature is slightly higher than the glass transition point of amorphous silica, ~1200 °C, the cell size and the cell volume fraction have different sensitivities to the temperature, we developed the subcritical calcination (SCC) technique for cellular silica, to adjust the cell size in a wide range while keep the cell volume fraction nearly constant.

2.2. Preparation of Silica Monoliths

Silica monoliths with various average cell sizes were first synthesized through sol-gel methods, following the work of (Shoup, 1976) for samples with the average cell size smaller than 500 nm and the works of (Miyamoto et al., 2013; Nakanishi, 2010) for samples with the average cell size larger than 1 µm, respectively.

For the former (smaller cells), as shown in Figure 2.1 (a), Sigma-Aldrich Ludox HS-40 colloidal silica was mixed with PQ Kasil-1 potassium silicate solution in a flask under magnetic stirring for 30 min, with the mass ratio in the range from 1:99 to 40:60. A larger colloidal silica amount tended to cause a reduced cell size. A 25 wt% formamide solution, which was diluted in water with the mass ratio of 40:60, was slowly added into the silica-silicate mixture and vigorously mixed by a magnetic stirrer for 30 min.

For the latter (larger cells), as depicted in Figure 2.1 (b), Sigma-Aldrich tetramethyl orthosilicate (TMOS, 98%) was added to a 0.01 M aqueous solution of acetic acid, and was thoroughly mixed in a flask under magnetic stirring for 30 min. In the acetic acid solution, Sigma-Aldrich polyethylene glycol (PEG, with the average molecular weight of 10,000) had been dissolved. The TMOS to PEG mass ratio varied from 3.0 to 7.2, so as to tailor the cell size.

The mixture was then transported into a polypropylene plastic vial, either a smaller one with the inner diameter of 35.6 mm and the height of 16.3 mm (for smaller cells) or a larger one with the inner diameter of 46.2 mm and the height of 21.6 mm (for larger cells). After aging and rinsing, the silica gels were dried in a VWR 1330GM oven at 80 °C for 72 h. The initial component mass ratios were listed in Table 2.1. The sol-gel synthesis setups were shown in Figure 2.2.

2.3. Subcritical Calcination of Silica Monoliths

The obtained silica monoliths had different average cell sizes and cell volume fractions. The cell size and the cell volume fraction were highly correlated, as shown in

Figure 2.4 (a). In order to uncouple these two important parameters, specifically to vary the cell size in a broad range and simultaneously keep the cell volume fraction around 60%, a subcritical calcination (SCC) treatment was carried out in a MTI GSL-1700X horizontal tube furnace at selected temperatures (T_s) for 1 h. The SCC temperatures ranged from 850 °C to 1265 °C. The ramp rate was initially set as 3 °C/min to keep the total heating time relatively short; and when the temperature was less than 100 °C away from T_s, was reduced to 1 °C/min, to minimize over-shooting. In order to reduce the residual stress, the cooling rate was set to be 3 °C/min.

In Figure 2.3, it can be seen that, when the temperature is slightly higher than the glass transition point of amorphous silica, ~1200 ^{o}C (Mackenzie, 1964), compared with the cell size, the cell volume fraction is much more sensitive to the treatment temperature. When the temperature is at the vicinity of the glass transition point, the viscosity of silica is highly dependent on temperature, resulting in the steep variation of the cell volume fraction (Brinker and Scherer, 1990). The relatively mild change in average cell size should be attributed to the balance between the reduction in smaller cells and the shrinkage of larger cells (Brinker and Scherer, 1990; Iler, 1979). Table 2.1 and Figure 2.4 (b) shows that as the treatment temperatures were optimized for silica monoliths of various initial component mass ratios, their cell volume fractions could be adjusted to a similar level, e.g. 60%.

2.4.   Polishing of Cellular Silica

To obtain homogeneous samples, the surface layers (Diao et al., 2011; Kawaguchi et al., 1986) of SCC-treated cellular silica samples were removed by a set of silicon carbide sandpapers. Before the SCC treatment, the thickness of silica gel samples was 10-14 mm. After the SCC treatment, the thickness shrank to about 8-9 mm. Nearly 1.5 mm thick surface layers from the top and the bottom of the samples were first removed by 320-grit sandpapers, followed by further polishing with 600-grit sandpapers until the sample thickness was around 5 mm. Then, the sample thickness was reduced to about 4.75 mm by 1200-grit sandpapers and finally to about 4.50 mm by 2500-grit sandpapers. During the polishing, a self-made sample fixture, as shown in Figure 2.5, was used to guarantee that the two sides of the sample disk were flat and in parallel, and that the final thickness had the accuracy of ±0.05 mm.

2.5. Characterization of Cellular Silica

2.5.1. Cell Volume Fraction

The cell volume fractions of the cellular silica samples were calculated from their mass densities (Gibson and Ashby, 1999): $p = 1-\rho/\rho_n$, where ρ is the sample density and $\rho_n = 2.2$ g/cm^3 is the density of solid amorphous silica (Brinker and Scherer, 1990). The specific cell volume is estimated using $v = p \cdot V_t/m$ (Gibson and Ashby, 1999), where V_t is the sample volume and m is the sample mass.

The dimensions and the cell volume fractions of SCC-treated silica samples are listed in Table 2.2. After being treated at different optimized SCC temperatures, the

samples have a similar cell volume fraction of ~60%, corresponding to a specific cell volume of ~0.7 cm^3/g.

2.5.2. Cell Size

The cell size (d) was characterized by the well-established Washburn method (Pirard et al., 2005; Washburn, 1921): $d = 4\sigma\cos\theta/P_{Hg}$, where P_{Hg} is the infiltration pressure, $\sigma = 0.484$ N/m is the surface tension of mercury, and $\theta \sim 140°$ is the contact angle. Figure 2.6 shows typical mercury porosimetry curves of cellular silica samples. The profile of the infiltration plateau, P_{Hg}, indicates the distribution of cell size. The width of the infiltration plateau is associated with the cell volume. The beginning and the ending points of the infiltration plateau are defined by dP/dV, as shown in Figure 2.7. The beginning point is taken as the location where dP/dV abruptly drops, associated with the large decrease in effective system compressibility. The ending point is determined by the point where dP/dV becomes relative large. From the infiltration plateau, the cell size range was calculated, and the average cell size was taken as the median value.

The mercury porosimetry results are summarized in Table 2.1. With the cell volume fraction of ~60%, the average cell size of cellular silica samples in the investigation ranges from tens of nm to more than 1 µm.

2.5.3. Speed of Sound

Longitudinal wave velocities of cellular silica samples with various average cell sizes were measured with a 38DL PLUS gage and a M112-RM transducer (10 MHz

longitudinal wave). As shown in Figure 2.8, the longitudinal wave velocity is not sensitive to the cell size. For the cell volume fraction of 60%, the longitudinal wave velocity is ~2.35 km/s, about 40% of that of solid silica ~5.97 km/s (Kaye and Laby, 1921).

2.5.4. X-Ray Diffraction Analysis

The SCC-treated cellular silica samples were analyzed through powder x-ray diffraction (PXRD), by using a Bruker D8 Advance Diffractometer at 40 kV and 40 mA for Cu Kα (λ= 1.5418 Å). The scan speed was 0.1 sec/step; the step size was 0.02°; the 2θ range was 10° to 80°.

As shown in Figure 2.9, the broad peaks around $2\theta \approx 22°$ suggest that the SCC-treated silica samples all exhibit a short range order; that is, the SCC temperature, T_s, in this investigation does not influence their amorphous nature.

2.5.5. Microscopy Analysis

The cellular silica samples were observed under a FEI-XL30 environmental scanning electron microscope (SEM) at 20kV, with a spot size of 3.0. The SEM samples had been coated with iridium using an Emitech K575X sputter coater at 85 mA for 6 seconds prior to the observation.

Figure 2.10 confirms that the cellular configurations of SCC-treated silica samples are similar. As the cell size changes in a broad range, neither the cell volume

fraction nor the cell structure is affected. All the cells are interconnected and open. The ligament length is correlated with the cell size, as it should be.

2.6.   Summary and Conclusion

Sol-gel method is a powerful approach for synthesis of silica-based cellular monoliths. However, the cell size and the cell volume fraction may be highly correlated. Based on a unique phenomenon that when the treatment temperature is slightly higher than the glass transition point of amorphous silica, compared with the cell size, the cell volume fraction of silica gel is much more sensitive to the temperature, we developed a subcritical calcination (SCC) technique to uncouple the relationship between the cell size and the cell volume fraction. As the SCC temperatures are optimized for silica gels of various initial component mass ratios, their cell volume fractions can be tailored to a similar level, while the final cell sizes ranges from tens of nm to more than 1 µm. The measurement of speed of sound suggests that the longitudinal wave velocity is mainly a function of the cell volume fraction. The powder x-ray diffraction (PXRD) analysis shows that all the SCC-treated silica samples are amorphous. The SEM observation indicates that all the SCC-treated silica samples have interconnected and open cell structures.

Chapter 2, in part, has been submitted for publication in Materials & Design, and co-authored by Meng Wang, Yang Shi, Jianguo Cao, and Yu Qiao. The dissertation author was the primary investigator and author of this work.

Table 2.1: Results of mercury porosimetry

Component mass ratio	TMOS to PEG	Colloidal silica to potassium silicate							
	5.5:1.0	1.3:98.7	7.5:92.5	12.5:87.5	17.0:83.0	22.5:77.5	27.5:72.5	35:65	40:60
SCC temperature (°C)	1230	1260	1262	1260	1258	1254	1251	1239	1228
Mercury infiltration pressure range (MPa)	[0.75,1.89]	[3.85,6.21]	[5.06,8.01]	[6.71,10.20]	[8.45,11.87]	[10.96,14.93]	[14.77,20.55]	[19.37,26.80]	[24.45,32.91]
Cell size range (nm)	[780,1980]	[240,390]	[190,290]	[150,220]	[130,180]	[100,140]	[70,100]	[60,80]	[40,60]

Table 2.2: Material parameters of SCC-treated cellular samples

Average cell size (nm)	1380	315	240	185	155	120	85	70	50
Cell volume fraction (%)	59.6±2.7	62.7±0.9	61.6±0.9	60.7±1.2	59.5±0.8	62.4±1.4	59.1±2.0	60.0±1.5	60.0±1.3
Diameter (mm)	22.9±0.9	22.6±0.1	22.3±0.3	22.6±0.4	22.6±0.2	23.5±0.3	23.0±0.3	23.7±0.5	24.2±0.3
Thickness (mm)	4.51±0.02	4.51±0.01	4.53±0.01	4.51±0.01	4.53±0.01	4.53±0.01	4.51±0.01	4.52±0.01	4.52±0.01
Specific cell volume (cm^3/g)	0.71±0.12	0.76±0.03	0.73±0.03	0.70±0.04	0.67±0.02	0.76±0.05	0.66±0.06	0.68±0.04	0.68±0.04
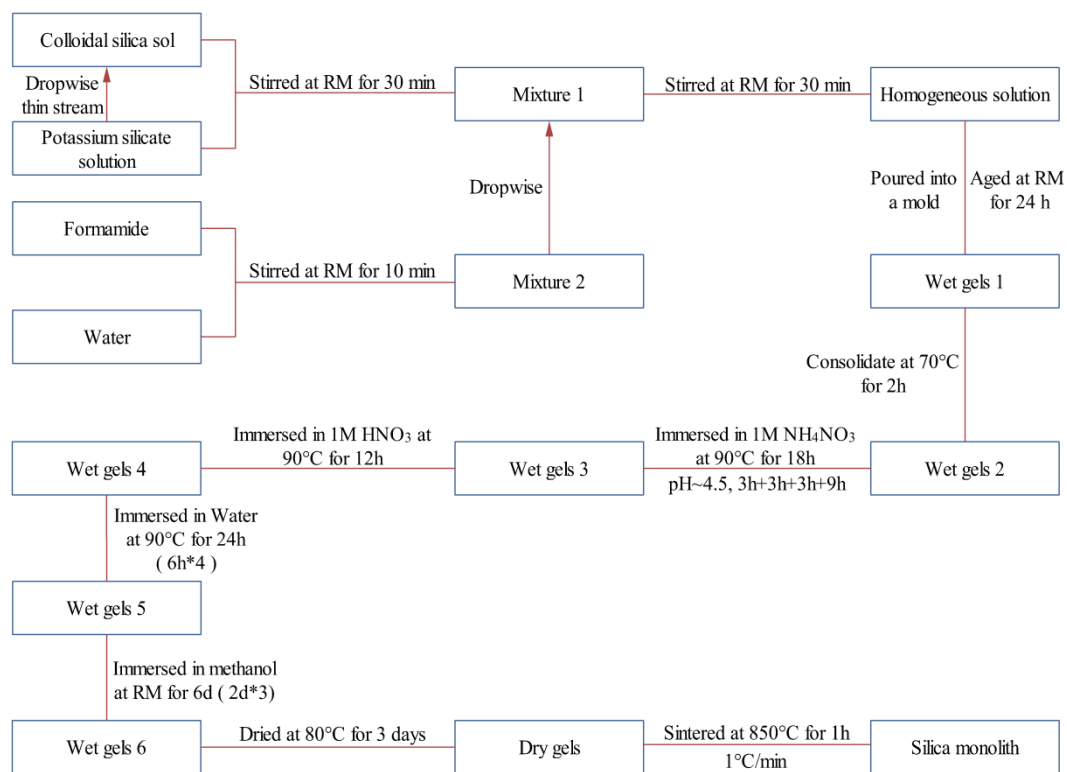
(a) Smaller cells
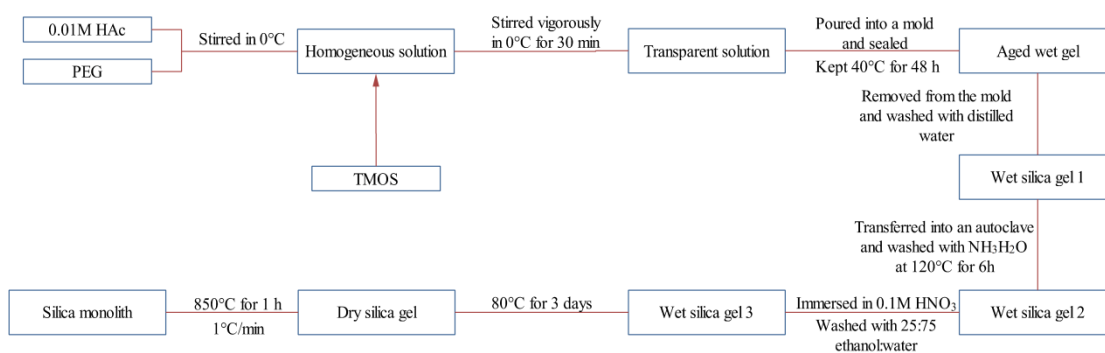
(b) Larger cells

Figure 2.1: Flow charts of silica monolith processing.

(a) Sol-gel synthesis   (b) Plastic molds and silica monoliths
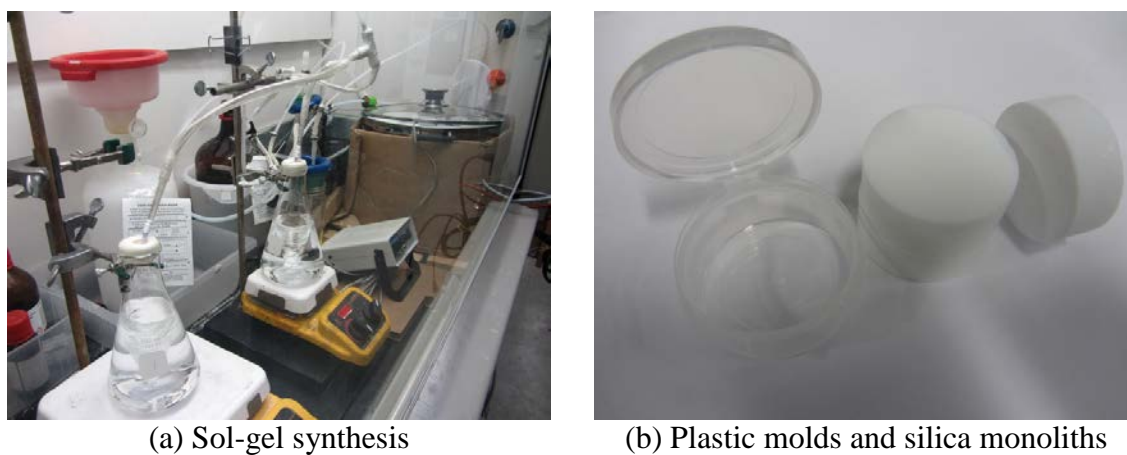
Figure 2.2: Setups for processing silica monoliths.
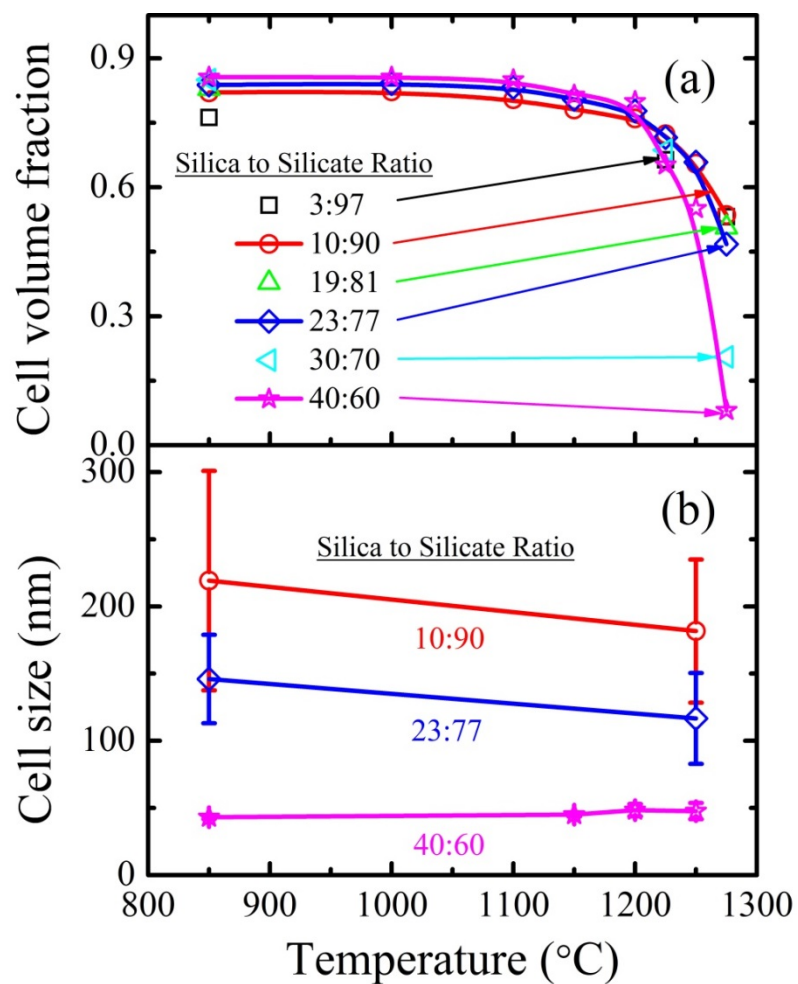
Figure 2.3: Effects of the SCC temperature, T_s, on (a) the cell volume fraction and (b) the average cell size of silica monoliths.
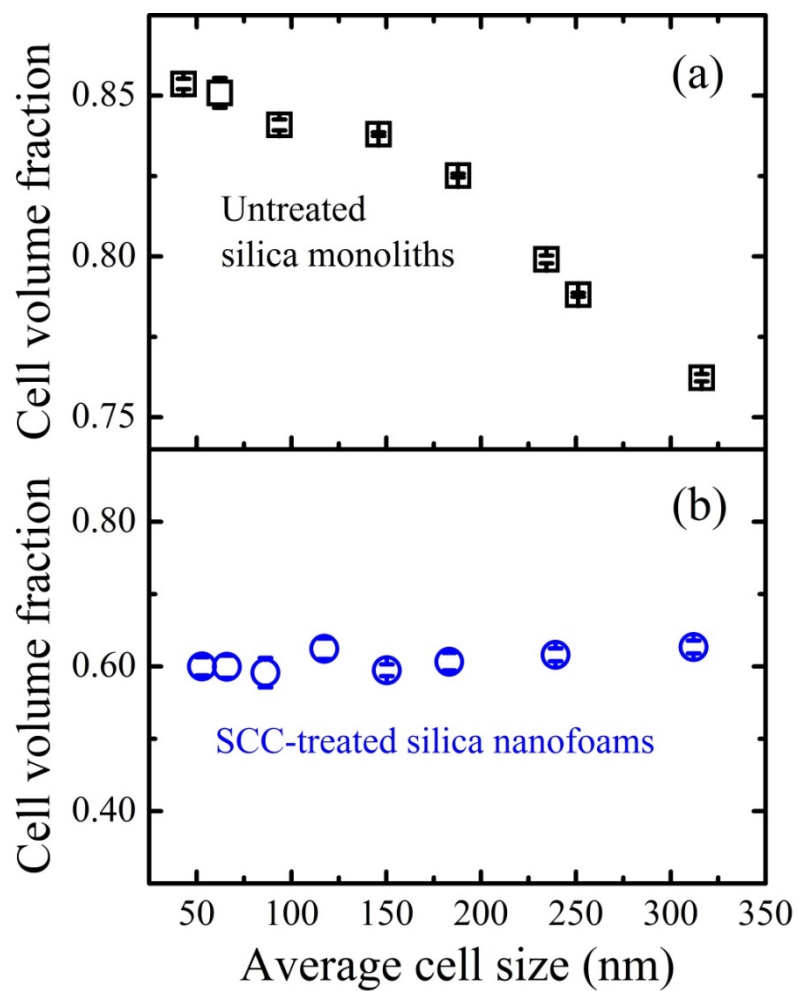
Figure 2.4: Relationships between cell size and cell volume fraction of treated and untreated silica samples.
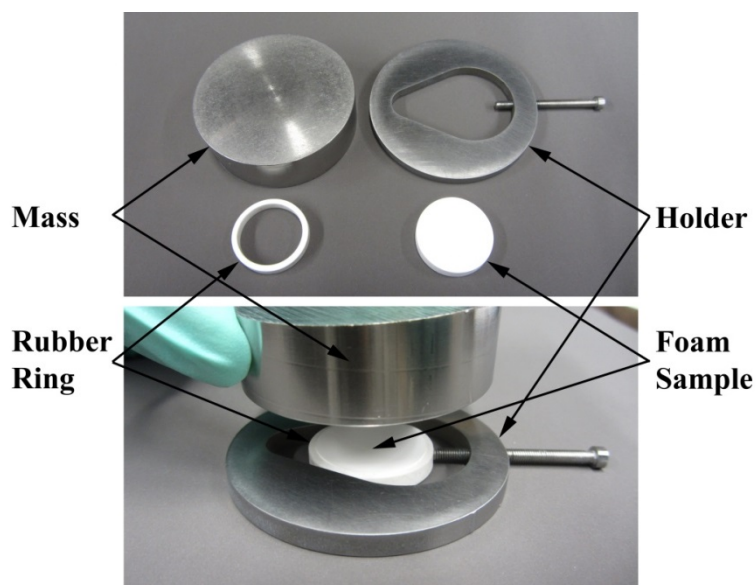
Figure 2.5: Sample fixture for polishing.
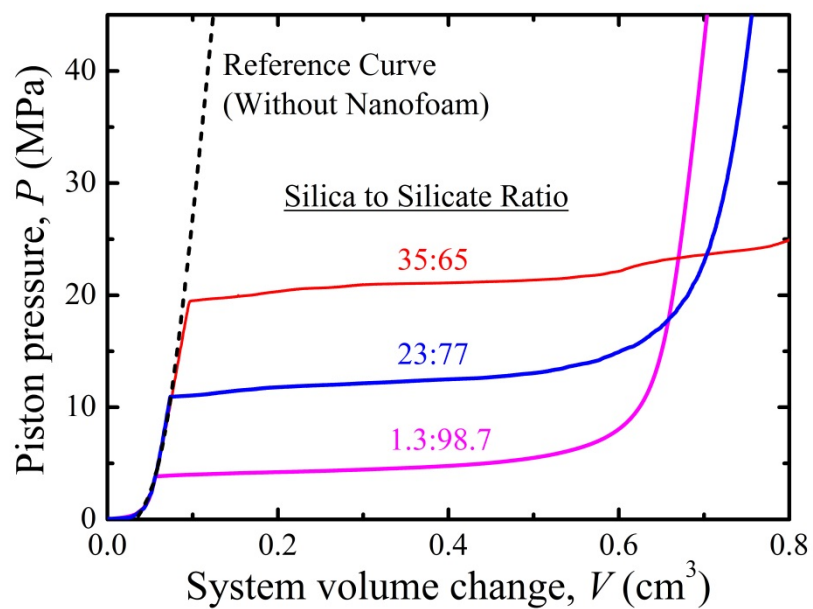
Figure 2.6: Typical sorption isotherm curves of mercury porosimetry. The dashed curve is for the reference compression test on mercury, without any cellular silica sample.
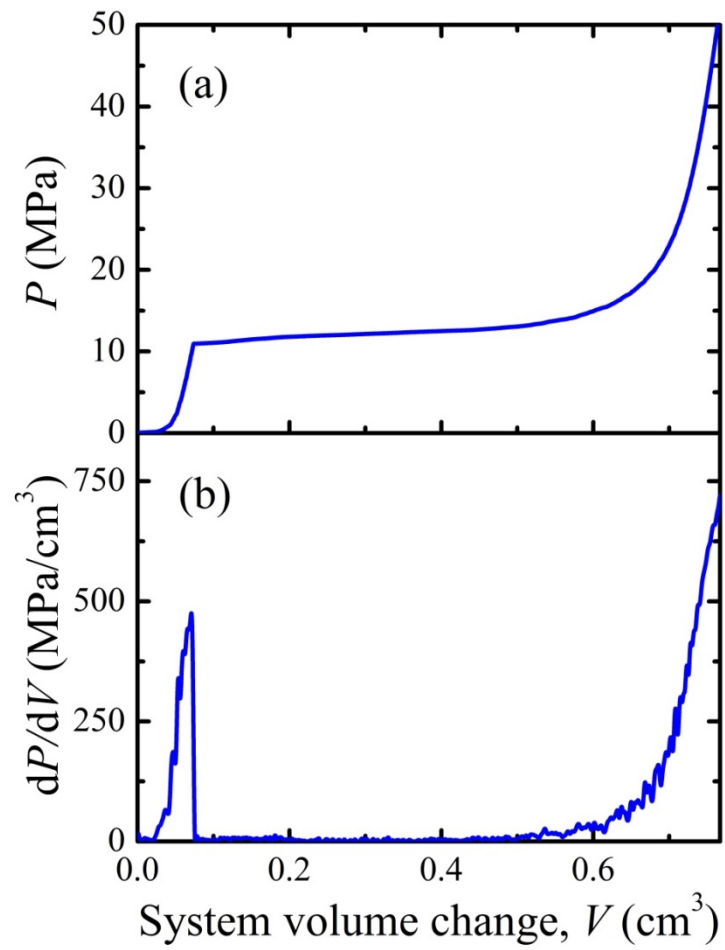
Figure 2.7: Definition of the infiltration plateau: (a) a typical sorption isotherm curve showing the relationship between P and V; (b) dP/dV.
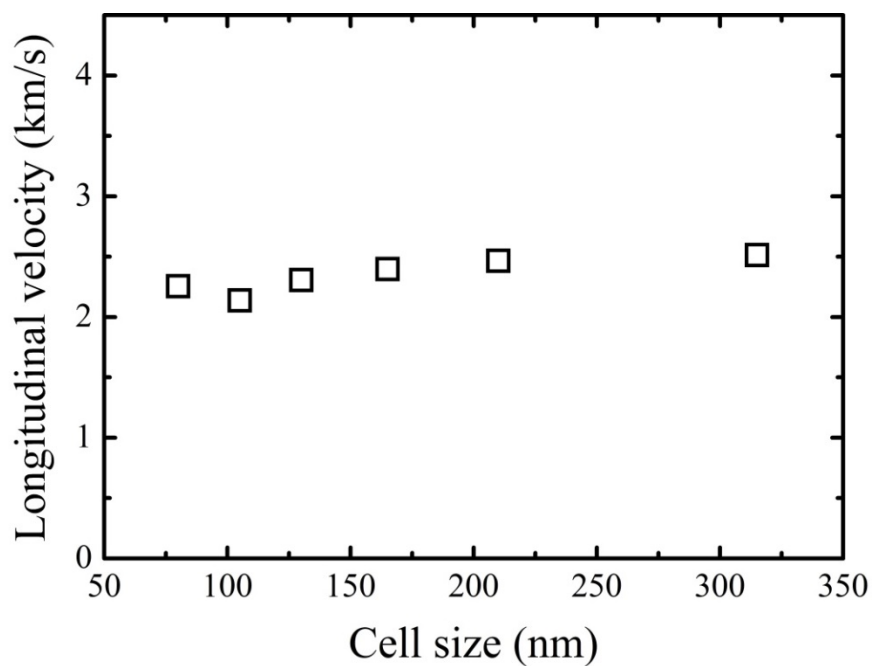
Figure 2.8: Speed of sound of cellular silica samples with various cell sizes. The cell volume fractions of all the samples are of ~60%.
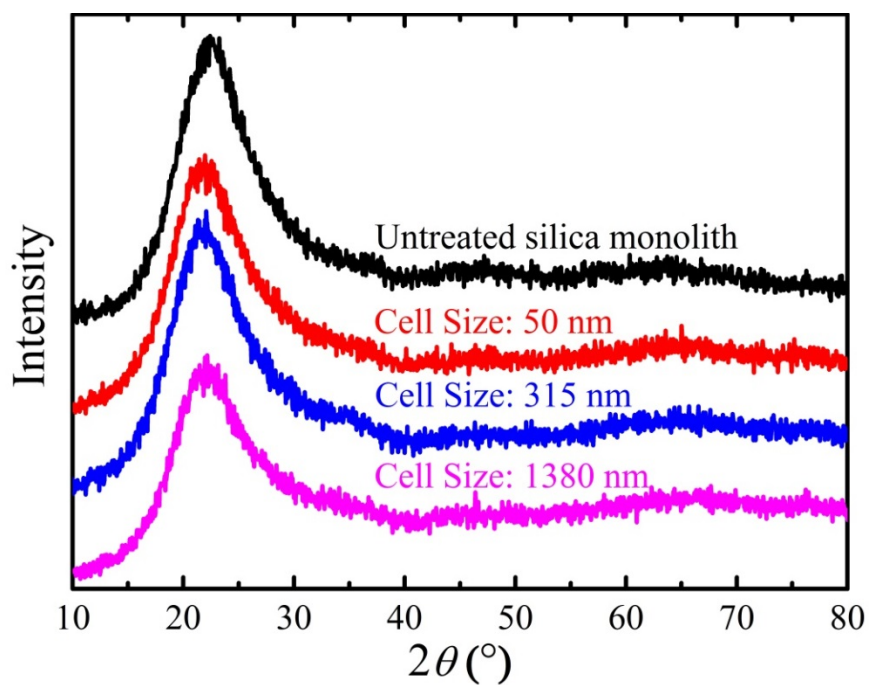
Figure 2.9: Typical XRD analysis results. The top curve is for an untreated silica monolith, and the bottom three are for SCC-treated cellular silica samples.
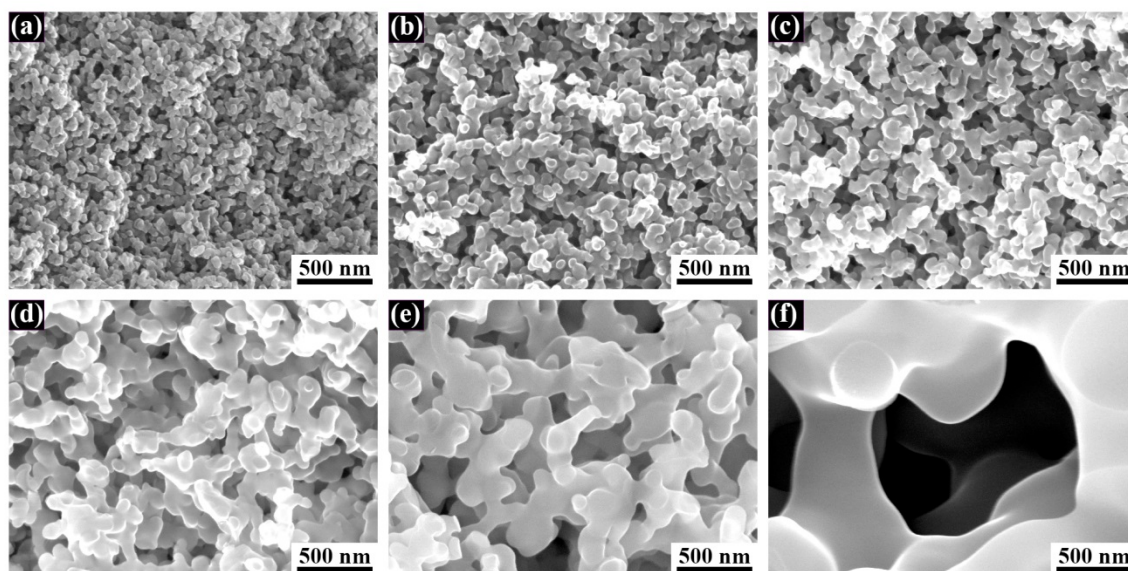
Figure 2.10: Typical SEM images of SCC-treated cellular silica samples, with the average cell sizes of (a) 50 nm; (b) 85 nm; (c) 120 nm; (d) 185 nm; (e) 315 nm, and (f) 1380 nm. The cell volume fractions of all the silica samples are ~60%.

CHAPTER 3

TESTING APPARATUS AND APPROACHES

3.1. Split Hopkinson Bar System

The dynamic responses of cellular silica disks were characterized by a Split Hopkinson Bar (SHB) system (Chen and Song, 2010; Kolsky, 1963), as depicted in Figure 3.1(a). By using a gas chamber, a Grade 9 titanium (Ti) tube striker was projected onto the impact end of the stainless steel incident bar. The outer diameter, the inner diameter, and the length of the striker were respectively 12.7 mm, 11.4 mm, and 462.0 mm. The two ends of the Ti tube were sealed by two 17-4 PH H900 stainless steel endcaps, respectively. The endcaps were pressed into the tube with a tight fit, and fixed by two stainless steel pins across the tube wall, respectively. The thickness of the endcaps was 5.1 mm, and the pin diameter and length were 3.2 mm and 12.7 mm, respectively. The total mass of the striker was 62.8 g. The striker was hosted by an AeroMarine polyurethane foam sleeve inside the gas chamber. The striker speed was controlled via

changing the inner pressure in the gas chamber. For example, when the gas pressure was set to 15.0 psi, the striker speed was ~8.5 m/s. The striker speed was measured by a couple of OMRON EE-SPW421 photomicro sensors.

The diameters of the incident bar and the transmission bar were the same, $D = 12.7$ mm; the lengths of them were 178 cm and 152 cm, respectively. They were made of 17-4 PH H900 stainless steel. The Young's modulus was 196.5 GPa, and the mass density was 7750 kg/cm^3. At the center of the two bars, two sets of Vishay WK-13-250BF-10C strain gauges were respectively mounted to collect the stress wave signals through a Vishay 2310B data acquisition (DAQ) system.

To ensure that only a single pulse loading would be applied on the cellular silica sample, a momentum trapper was employed, following the works of Nemat-Nasser and Chen (Nemat-Nasser et al., 1991; Song and Chen, 2004), as shown in Figure 3.1 (c). It consisted of a rigid block, a flange attached to the far end of the incident bar, and a two-piece thread clamping locknut. There was a gap between the flange and the rigid block. The gap width was precisely controlled so that the motion of the flange would be stopped immediately after the entire tensile stress wave generated by the striker had entered into the incident bar. Thus, repeated pulse loadings were prevented.

3.1.1. Dynamic Compression Tests

Dynamic compression tests on cellular silica samples were conducted by using the SHB system. The titanium striker was projected by the gas chamber to the stainless steel incident bar. Upon impact, a compressive stress wave was generated and propagated

along the incident bar (Kolsky, 1963). In all the tests, the striker speed was kept at ~8.5 m/s. On the near end of the incident bar a cellular silica disk sample was firmly attached, supported by a stainless steel transmission bar from the back. The stress wave entered into the silica sample, and eventually transmitted to the transmission bar.

3.2.   Shear-Promotion System

The shear-promotion support ring (SPSR), as shown in Figure 3.2, included a front part, a rear part, and several mounting parts (e.g. cap screws, spring washers and hex nuts). The main body (rear and front parts) was made of 17-4 PH stainless steel. Figure 3.4 showed its configuration in the SHB system. In Figure 3.4 (a), the silica disk sample (#2) was mounted between the front part (#7, #8 and #9) and the rear part (#3, #4 and #6). The end of the incident bar (#1) was compressed against the surface of the sample. At the back of the silica disk, a stainless steel ring (#3) and a stainless steel disk (#4) were used to support the sample against the transmission bar (#5). The inner diameter of the ring (#3, D_r) was 13.1 mm; the outer diameter was 25.0 mm; the thickness was 3.0 mm. The diameter of the steel disk (#4) was 43.0 mm; the thickness was 3.0 mm. The centers of the incident bar (#1) and the support ring (#3) were accurately aligned with the help of the guiding parts (#6 and #9) and the tight fit between the six positioning holes (diameter 3.0 mm) on the edge of the SPSR with M3 screws, with the gap width between the outer surface of the incident bar (#1, D) and the inner surface of the support ring (#3, D_r) being 0.20 mm along all the directions. Parts #3 and #7 were designed to reduce the potential bending of the silica sample during the testing.

Figure 3.4 (b) depicts the working principle of the SPSR. With the forces of the incident bar and the support ring applied on the silica sample in the opposite directions, geometric instability would be generated, promoting shear deformation. The design of SPSR was inspired by the hat-shaped specimen used often by Marc Meyers and Vitali Nesterenko (Meyers et al., 1992; Meyers et al., 2003; Nesterenko, 2001). The lateral surface of silica sample was loosely confined by a compliant polyurethane ring, with the initial inner diameter of 19.1 mm and outer diameter of 22.2 mm.

3.2.1. Quasi-static Shear Tests

Quasi-static shear tests on cellular silica samples were conducted using an Instron 5582 machine. As shown in Figure 3.3, a disk sample was sandwiched in between a stainless steel loading rod and a stainless steel shear-promotion support ring (SPSR). The inner diameter of the SPSR was 13.1 mm, slightly larger than the outer diameter of the loading rod, $2r = 12.7$ mm. The shear gap width, the difference between the radius of the moving rod and the inner radius of the support ring, was 0.20 mm. On the Instron machine, the loading rod compressed the silica sample, with the loading/unloading rate of 0.01 mm/min. Shear instability was triggered by the geometrical change of the SPSR (Meyers et al., 2003; Nesterenko, 2001).

3.2.2. Dynamic Shear Tests

Dynamic shear tests were conducted on cellular silica disks by using the SHB system shown in Figure 3.1. As shown in Figure 3.4, a cellular silica sample was

compressed against the near end of the incident bar; at the back of the sample, a stainless steel ring and a stainless steel disk were used to support the sample against the transmission bar. The SPSR was the same as that in the quasi-static shear experiment. Due to the geometrical change, the shear instability was promoted (Meyers et al., 2003; Nesterenko, 2001). There were two main variables: striker speed and shear gap width, which affect the effective shear strain rate. In most of the experiments, the striker speed was maintained at ~8.5 m/s and the shear gap width was set as 0.20 mm to investigate the cell size effect. In order to analyze the rate effect, the striker speed was varied from ~5.0 m/s to ~9.5 m/s, and the shear gap width was changed from 0.40 mm to 0.10 mm.

3.3. Indentation System

The indentation test system, as shown in Figure 3.5 (a), consisted of a front part, a rear part, a hemispherical indenter, and several mounting parts (e.g. cap screws, hex nuts, and spring washers). The front and rear parts were made of 17-4 PH stainless steel, designed to minimize the bending deformation of the silica sample during testing. A tungsten carbide (TC) indenter with the diameter of 4.75 mm, the hardness of 91 HRA, and the surface roughness of 0.7 micro inch Ra maximum was employed. It was firmly attached to one end of a 17-4 PH stainless steel cylinder by VISHAY M-Bond 200 adhesive. The diameter and the length of the cylinder were 12.7 mm and 25.4 mm, respectively. A cellular or solid silica sample was sandwiched in between the indenter and the steel substrate on the rear part, as shown in Figure 3.5 (b). The far end of the steel cylinder would be subjected to either a quasi-static or a dynamic loading. The lateral

surface of the silica sample was confined by two rings: a compliant polyurethane (PU) inner ring, with the initial inner diameter of 19.1 mm and the initial outer diameter of 22.2 mm; and a stiff polyvinyl chloride (PVC) heat-treated outer ring, with the initial inner diameter of 25.4 mm and the shrinking ratio of 2:1.

3.3.1. Quasi-static Indentation Tests

Quasi-static indentation tests were conducted on cellular and solid silica samples using an Instron 5582 machine, as shown in Figure 3.6. A silica sample was sandwiched in between a hemispherical indenter and a steel substrate. The hemisphere indenter was compressed into the sample. There were three parameters here: loading/unloading rate, maximum force, and indenter diameter. In this project, the loading /unloading rate was 0.01 mm/min; the maximum force was 300 N; and the indenter diameter, $2r = 4.75$ mm.

3.3.2. Dynamic Indentation Tests

Dynamic indentation tests were performed on a similar set of cellular and solid silica samples using the SHB system. As shown in Figure 3.7, as the striker was projected by a gas chamber to impact the incident bar, the incident bar compressed a tungsten carbide hemispherical indenter into the silica sample. The silica sample was firmly supported by a stainless steel substrate, followed by the transmission bar. The diameter of the indenter was 4.75 mm. The loading mode was similar with that in the quasi-static indentation experiment, while the loading rate was much higher.
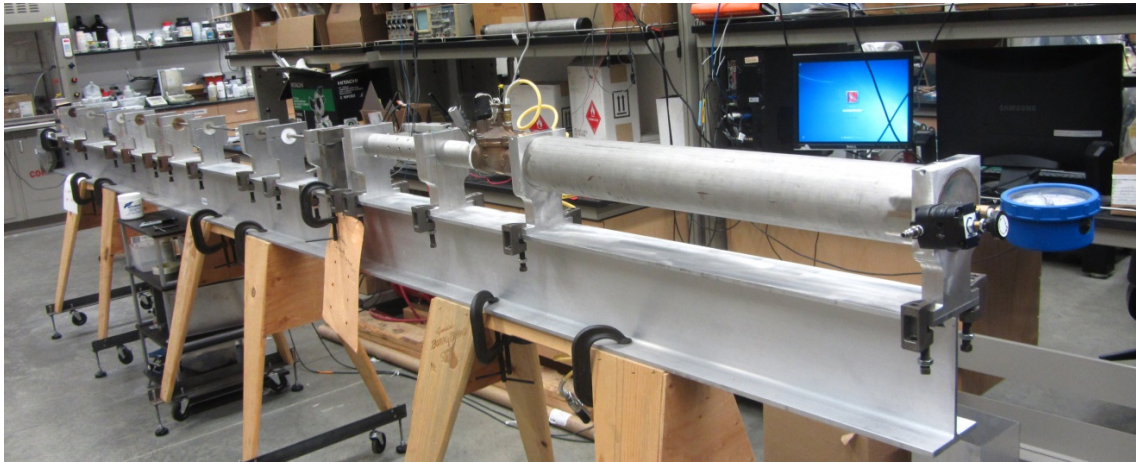
(a)

(b)
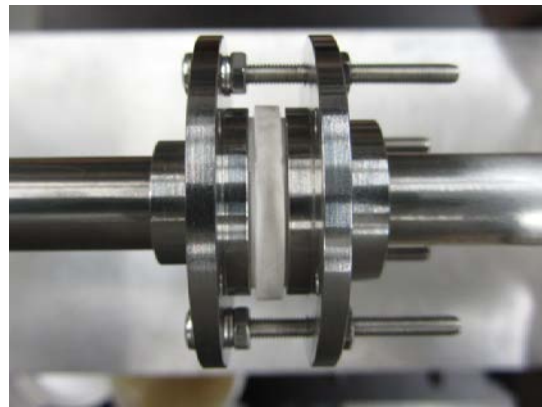
(c)

Figure 3.1: Split Hopkinson Bar Systems: (a) the overall configuration; (b) the shear-promotion system; and (c) the momentum trapper.

Figure 3.2: The shear promotion support ring and a cellular silica disk sample.
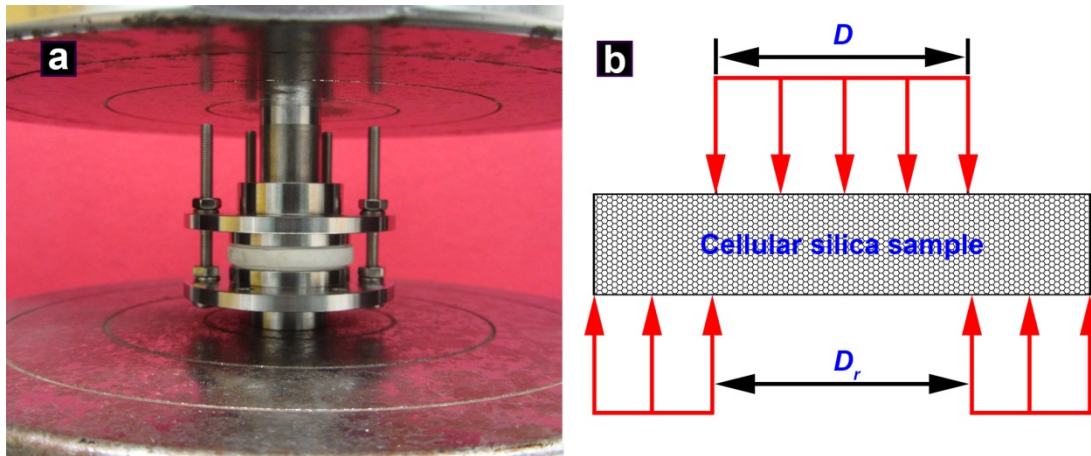
Figure 3.3: Quasi-static shearing. (a) Experimental setups. (b) Schematic of forced-shearing.
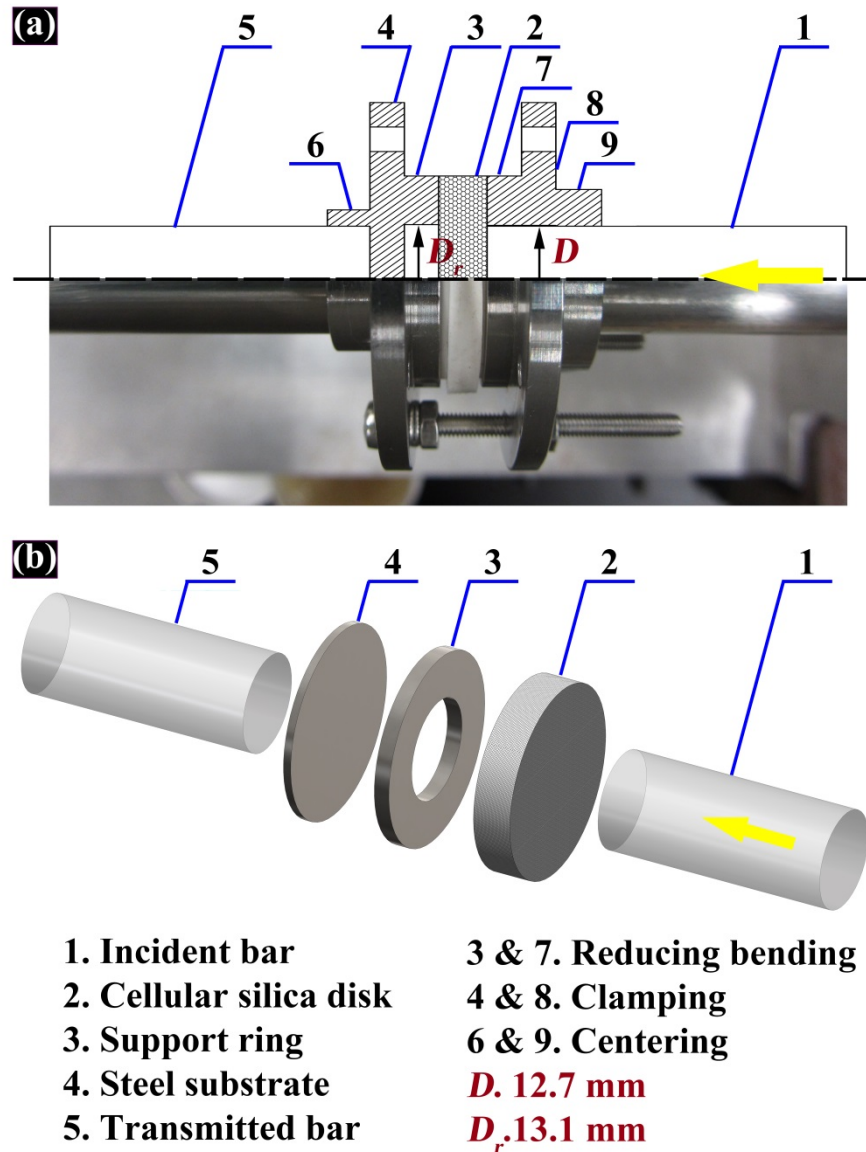
Figure 3.4: Configuration of shear promotion support ring in the split Hopkinson bar system: (a) half-section view of SPSR; (b) diagram of forced shearing. The shear gap width here is 0.20 mm. The yellow arrow indicates the impact direction of the striker (not shown here).

Figure 3.5: Photos of the indentation test system. (a) The system components and a cellular silica sample. (b) A cellular silica sample mounted on the indentation test system.
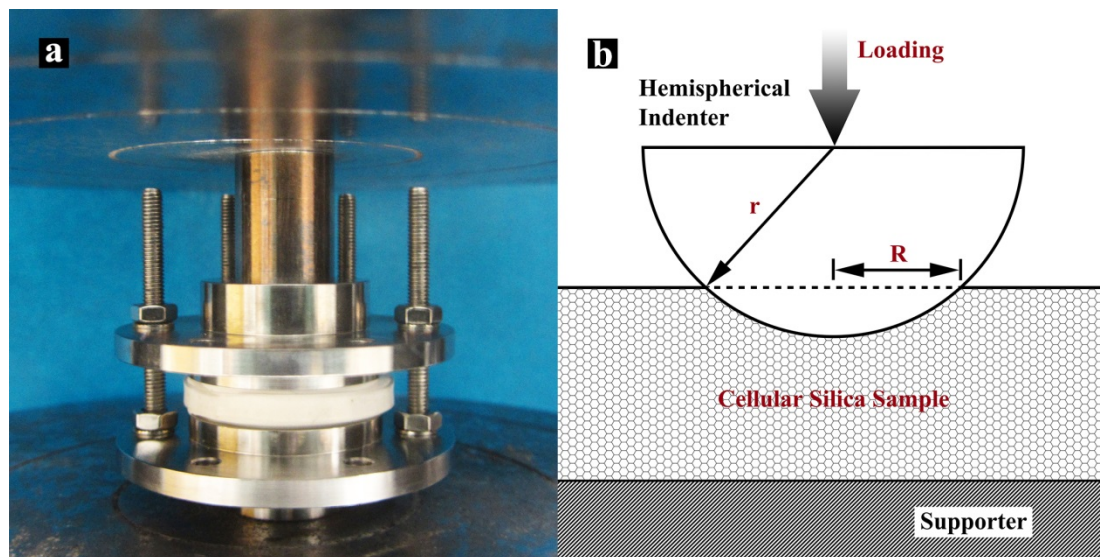
Figure 3.6: Quasi-static indentation. (a) Experimental setups. (b) Schematic of indentation.
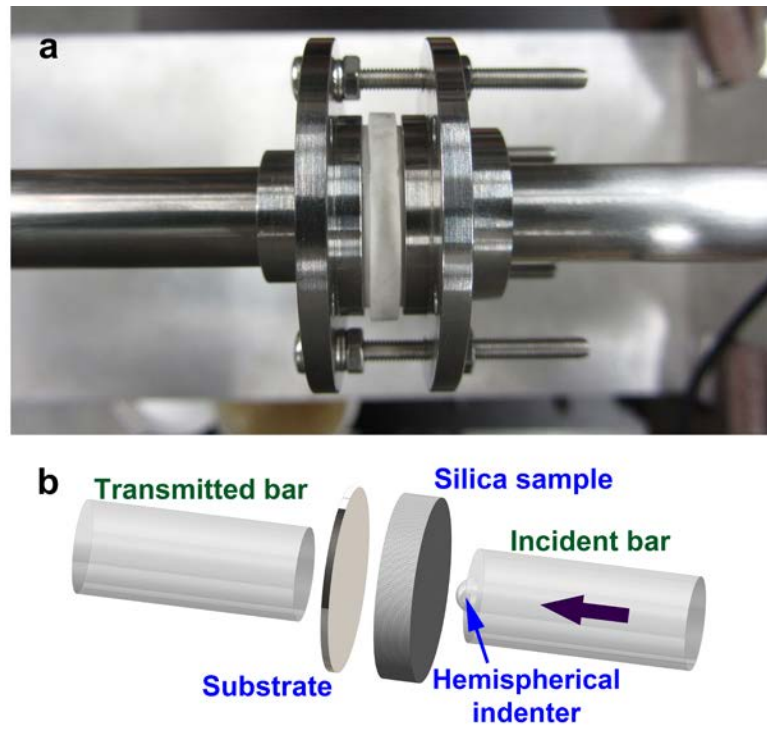
Figure 3.7: Dynamic indentation. (a) Experimental setups and (b) Schematic of indentation.

CHAPTER 4

QUANTITATIVE SEM IMAGE ANALYSIS

4.1.   Introduction

To associate the macroscopic shear behavior of cellular silica with its microstructural changes, a quantitative image analysis technique was developed, by using Matlab and Image-Pro Plus. Two-dimensional nominal cell volume fractions of pristine and tested cellular samples were measured.

The pristine cell structures were uniform, providing a reliable reference for the analysis of deformed cell structures. The SEM samples were harvested appropriately and well preserved. A relatively large number of SEM images were processed to obtain statistically meaningful results.

Below, we will use a cellular silica sample with the average cell size of 255 nm as an example to show the procedure of the SEM image analysis technique. The cell volume

fraction was ~79%; the sample thickness was 5.0 mm. It was dynamically sheared with a striker speed of ~4.0 m/s and the shear gap width of 0.20 mm.

4.2.   Two-dimensional Nominal Cell Volume Fraction

Because the depth of the SEM view field was larger than the investigated cell size, there would inevitably be shadows in the SEM images, as shown in Figure 4.1. In order to carry out a quantitative image analysis, image filtering was conducted through combination of the Shading Correction technique developed by Reyes-Aldasoro (Reyes-Aldasoro, 2009) and the Local Equalization function built in the Image-Pro Plus software (Media Cybernetics Manufacturing, Warrendale, PA, USA), as demonstrated in Figure 4.2. A SEM image was first enhanced by the Shading Correction, reducing the shadow of the cell structure. Then it was imported into Image-Pro Plus, and Local Equalization was employed to enhance its local contrast with the window size of 60 pixels, the step of 1 pixel, and the standard deviation of 0.5. Finally the Otsu's method (Otsu, 1975) was used to obtain the threshold (Matlab built-in function Graythresh) and the image was converted into binary format. On the converted image, a nominal two-dimensional cell volume fraction, p_2, was defined as the percentage of the black area. The measurement results of p_2 qualitatively matched the cell volume fraction data (p) calculated from the mass density of untested cellular silica samples, consistent for self-comparison purpose. The numbers of pixels in white and black areas were counted through the Matlab built-in function Bwarea.

4.3.   Uniformity of Pristine Cell Structure

Sol-gel methods were employed to process the cellular silica samples. The structure before firing should be uniform. After the gel was fired at different temperatures to achieve the desired cell volume fraction, there might be variations in cell structures from the surface to the interior. For the 255 nm cell-sized silica, the initial sample thickness was around 9~10 mm. We used sandpapers to remove the top and the bottom layers, and polished the final sample thickness to ~5.0 mm. The diameter of the disc sample was about 23 mm, and only the center part was used for the test. In Figure 4.3, around the center part, and along the thickness direction, the cell structures were scanned. The image analysis gave the two-dimensional nominal cell volume fractions of local areas. The results showed that the sample structure was quite uniform.

4.4.   Harvesting SEM Samples

4.4.1. Low Impact Rate Tests

After the dynamically shear test, a SEM sample was harvested from the impacted cellular silica disk. Under a relatively low impact rate of the striker, as depicted in Figure 4.4, the silica sample remained structurally integral after testing. Attention was primarily focused on the front side of the silica disk facing the incident bar. To best preserve useful information, a thin layer of epoxy was applied on the other side of the disk. From the back surface, in the center part of the disk and along a radius line, three holes with the diameter of 0.0236'' were drilled. A razor blade was placed in the middle hole, with the

sharp corner toward an adjacent hole, and carefully impacted by a hand hammer. A crack would be generated and propagate along the radius direction, splitting the silica disk into two parts. The exposed lateral fresh fracture surfaces were observed under a SEM.

4.4.2. High Impact Rate Tests

At a relatively high impact rate of the striker, after testing, the cellular silica disk would fragment into a number of smaller pieces, as shown in Figure 4.5. The parts of the lowest crack number density were chosen for the SEM analysis. The origin in the SEM image was offset, as the central part of the disk could be lost, as shown in Figure 4.5 (b). The diameter of the cellular silica sample was known; the diameter of the forced-shear ring facing the incident bar was 12.7 mm; along the radius direction of the SEM sample, the cutoff distance between the two circles could be determined as d_1; the length of the SEM sample was measured from the SEM image directly as d_2; the difference between d_1 and d_2 was the offset value of the origin in the X-Depth coordinate system. The origin offsetting was performed using the software of Photoshop.

4.5. Strategy of SEM Scanning

A relatively large number of SEM images were analyzed. To collect the information of the deformation zones effectively, the preserved sample surfaces were strategically scanned. First, we assessed the scanning range of the sample through visual inspection. The primary goal was to estimate the areas of deformed cells. As the cell size

was small and the number of cells was large, the boundaries of deformation zones could be identified only based on statistics. As shown in Figure 4.6 (a), the areas around the intersection of the outer edge of the incident bar and the front surface of the cellular disk should be scanned. Sections immediately adjacent to the sample-bar interface might have been compressed and were very often damaged; the outer fields were given a higher priority.

Second, we built up an X-D coordinate system, with "D" indicating the sample depth direction (parallel to the impact direction) and "X" the radius direction (normal to the impact direction). The origin was set at the intersection of the outer edge of incident bar and the front surface of cellular sample, based on the surface features shown in Figure 4.6 (c). The X-D coordinate helped to locate the scanning points and to coordinate the analysis results of different fields.

Third, we set a scanning map. For each SEM sample, a relatively large rectangular field ahead of the origin was scanned; typically, ~600 images were taken, corresponding to ~100 scanning points. Usually five or six scanning lines were needed to give an acceptable resolution of the boundary of the deformation zone, one of which was for the compressed area. About 20 points along each line were observed. The sample thickness was 5.00 mm or 4.50 mm. To cover a half of the thickness by 20 points, the distance between adjacent scanning points (D_1) should be about 125 µm. In our work, for the sake of convenience, D_1 was set to 186 µm at the magnification of 500X, the same as the height of a single SEM image. Cracked areas were skipped.

Then, we set the scanning path for each scanning point, so that the SEM view field would return to the starting spot after six images had been taken.

Finally, we took high-resolution SEM images following the pre-set path for each scanning point. This scanning strategy, specified in Table 4.1, must be strictly followed for all the scanning points for all the SEM samples.

4.6.   Quantitative Image Analysis

Using the developed quantitative image analysis technique, the distribution of local two-dimensional nominal cell volume fractions for each selected sample was measured. The cell structure along $X = 0$ undergoes the most severe deformation, and cell deformation is less pronounced in the far field. A critical local cell volume fraction change ratio, different from which the cell structure is considered deformed, is used to define the boundary of the shear deformation zone: ϑ = (local cell volume fraction)/(reference cell volume fraction), where the reference cell volume fraction is the average cell volume fraction of non-deformed areas in the far field. Due to the small cell size and the large cell number, the standard deviation is less than 2% of the average cell volume fraction.

Take the cellular silica sample with the average cell size of 255 nm as an example. Table 4.2 shows the original SEM images along the scanning lines: $X = 0$ µm, $X = 242$ µm and $X = 484$ µm. The image analysis results are listed in Table 4.3. The background cell volume fraction is measured as 0.5246, and the critical normalized cell volume fraction, ϑ, is 1.014. Table 4.4 gives the updated image analysis results, in which the deformed zone is marked by the red numbers.

Chapter 4, in part, is currently being prepared for submission for publication of the material, and co-authored by Yu Qiao. The dissertation author was the primary investigator and author of this work.

Table 4.1: SEM scanning strategy
(50 X 2.42 mm × 1.86 mm; 500 X 242 μm × 186 μm; 25000 X 4.84 μm × 3.72 μm)

	Non-compression zone				Starting Point			Compression zone
X D	968	726	484	242	0			-242
0					5	4	3	
					6	1	2	
186								
372								
558								
744								

Table 4.2: Original SEM images along the scanning lines
(Sample thickness 5.0 mm; cell size 255 nm; cell volume fraction 78.8%)
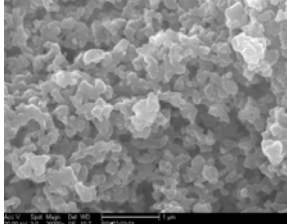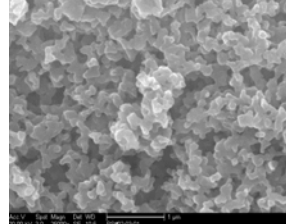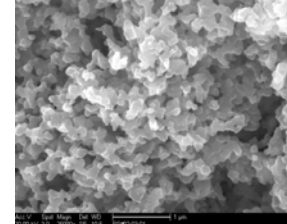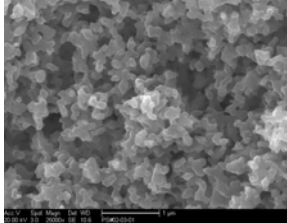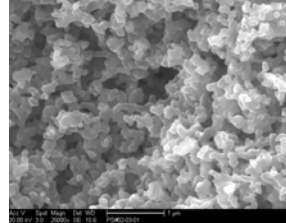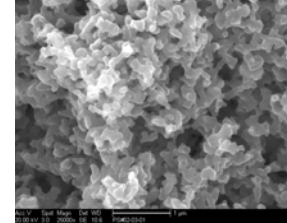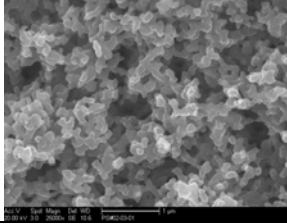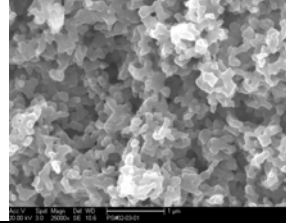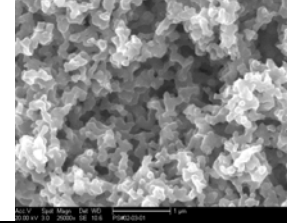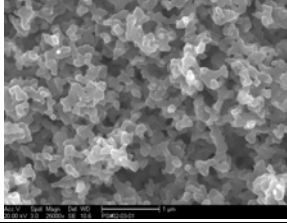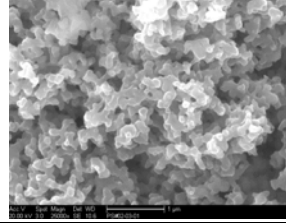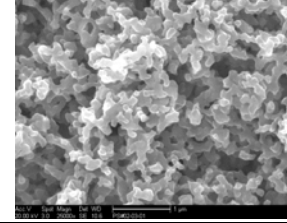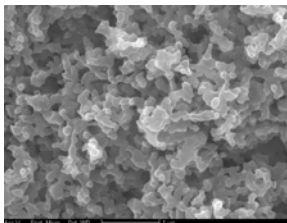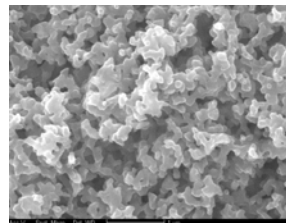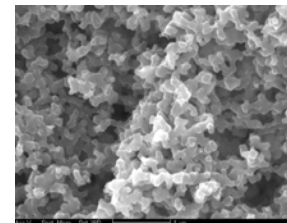
Unit: μm	X ←		
	484	242	0
0			
186			
372			
558			
Depth 744			

Table 4.2 (continued)

Unit: μm		X →		
		484	242	0
Depth ↓	930			
	1116			
	1302			
	1488			
	1674			

59

Table 4.2 (continued)
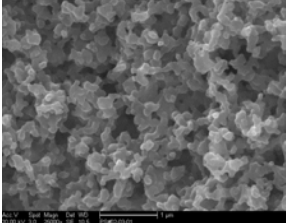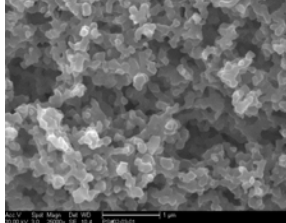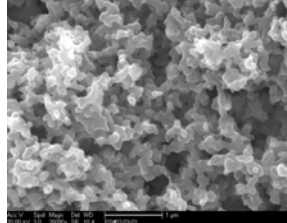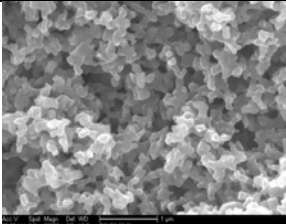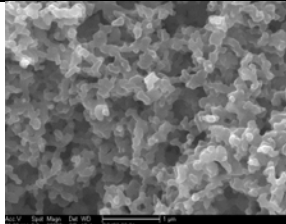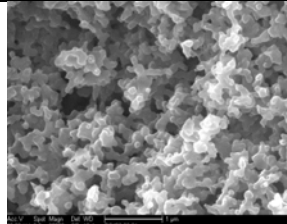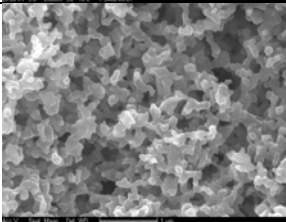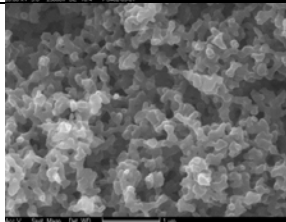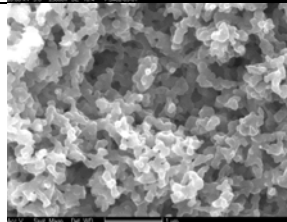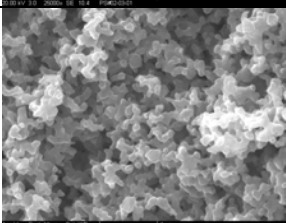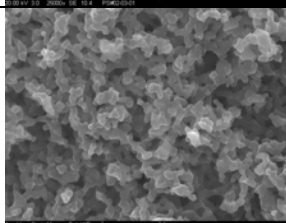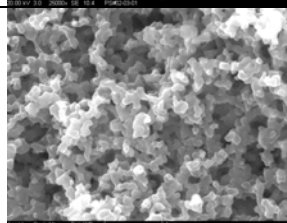
Unit: μm	X ←		
	484	242	0
1860			
2046			
2232			
Depth 2418			

Table 4.3: An example of the results of SEM image analysis
(Sample thickness 5.0 mm; cell size 255 nm; cell volume fraction 78.8%;
partition 3 × 3; critical value 0.532)

Unit: μm		X											
Depth		968	Stdev	726	Stdev	484	Stdev	242	Stdev	0	Stdev	-242	Stdev
	0	0.5375	0.0145	0.5399	0.014	0.5438	0.0172	0.5382	0.0138	0.5335	0.0114	0.5307	0.0143
	186	0.528	0.0171	0.531	0.0149	0.5281	0.011	0.54	0.0118	0.5304	0.0134	0.5241	0.0149
	372	0.5312	0.0153	0.5317	0.0146	0.5261	0.0126	0.5315	0.0111	0.5354	0.0136	0.5291	0.0174
	558	0.5239	0.0149	0.5252	0.0147	0.529	0.0127	0.5345	0.0177	0.5308	0.0194	0.5233	0.0132
	744	0.5236	0.0121	0.5292	0.0161	0.5227	0.0148	0.5383	0.0155	0.5195	0.012	0.5355	0.0205
	930	0.5305	0.0151	0.5305	0.0167	0.5232	0.0172	0.5221	0.0147	0.5306	0.0129	0.536	0.0115
	1116	0.5353	0.0118	0.5232	0.0147	0.5277	0.0171	0.5284	0.0189	0.5312	0.0121	0.5325	0.0135
	1302	0.5273	0.0128	0.529	0.0176	0.5242	0.0176	0.5209	0.0171	0.5223	0.015	0.5246	0.0171
	1488	0.5361	0.0156	0.5329	0.0143	0.5394	0.013	0.5283	0.0129	0.5394	0.0125	0.5244	0.0151
	1674	0.5285	0.0152	0.5266	0.0186	0.5363	0.0177	0.5246	0.0146	0.5233	0.011	0.529	0.017
	1860	0.5299	0.0163	0.5311	0.0184	0.5187	0.0171	0.5252	0.0193	0.5384	0.0137	0.5228	0.013
	2046	0.5273	0.0161	0.5329	0.0163	0.5253	0.0213	0.512	0.014	0.5199	0.013	0.5214	0.0123
	2232	0.5283	0.0147	0.5198	0.0112	0.5263	0.0153	0.5214	0.0205	0.532	0.0167	0.5311	0.0127
	2418	0.5226	0.0184	0.5268	0.0125	0.5331	0.0125	0.5213	0.0169	0.526	0.0165	0.5169	0.0146

Table 4.4: Updated results of SEM image analysis
(Sample thickness 5.0 mm; cell size 255 nm; cell volume fraction 78.8%;
partition 3 × 3; background cell volume fraction: 0.5246; critical value 1.014)

Unit: μm		X					
		968	726	484	242	0	-242
Depth	0	**1.0246**	**1.0292**	**1.0366**	**1.0259**	**1.0170**	**1.0116**
	186	1.0065	1.0122	1.0067	**1.0294**	**1.0111**	**0.9990**
	372	1.0126	1.0135	1.0029	**1.0132**	**1.0206**	**1.0086**
	558	0.9987	1.0011	1.0084	**1.0189**	**1.0118**	**0.9975**
	744	0.9981	1.0088	0.9964	**1.0261**	0.9903	**1.0208**
	930	1.0112	1.0112	0.9973	0.9952	**1.0114**	**1.0217**
	1116	1.0204	0.9973	1.0059	1.0072	**1.0126**	**1.0151**
	1302	1.0051	1.0084	0.9992	0.9929	**0.9956**	1.0000
	1488	1.0219	1.0158	1.0282	1.0071	**1.0282**	0.9996
	1674	1.0074	1.0038	1.0223	1.0000	**0.9975**	1.0084
	1860	1.0101	1.0124	0.9888	1.0011	**1.0263**	0.9966
	2046	1.0051	1.0158	1.0013	0.9760	**0.9910**	0.9939
	2232	1.0071	0.9909	1.0032	0.9939	**1.0141**	1.0124
	2418	0.9962	1.0042	1.0162	0.9937	**1.0027**	0.9853
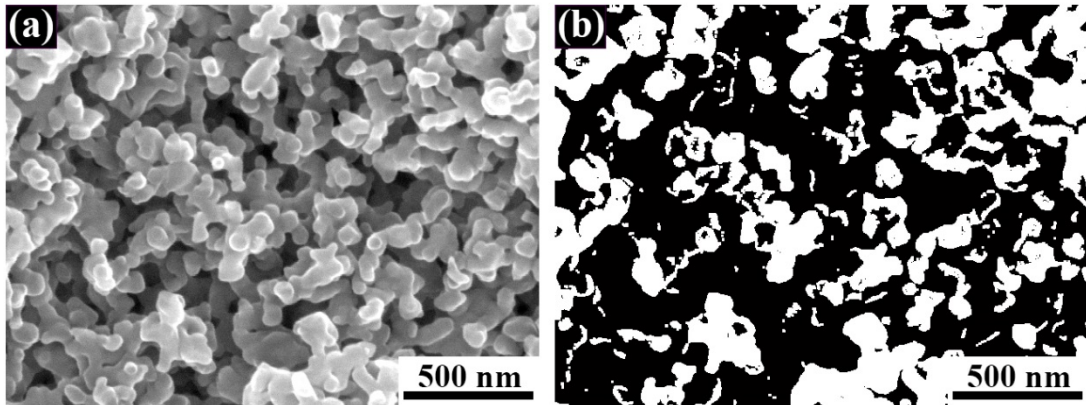
Figure 4.1: Shadow in the SEM image of a cellular silica sample. (a) Original SEM image. (b) Binary image derived from the Otsu's method.
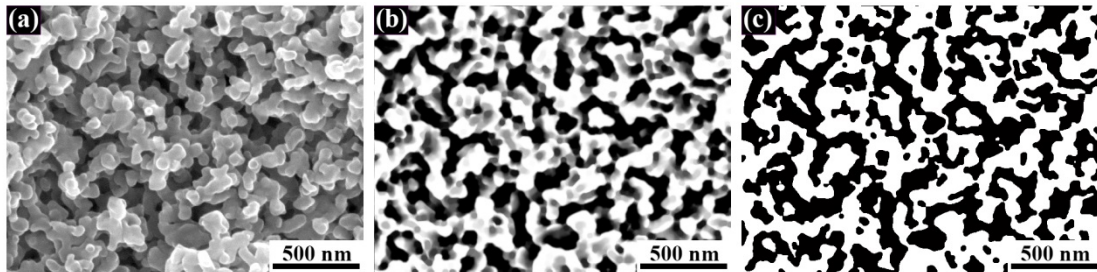
Figure 4.2: Two dimensional nominal cell volume fraction of a cellular silica sample. (a) Typical original SEM image. (b) Enhanced SEM image. (c) Binary image derived from the Otsu's method.
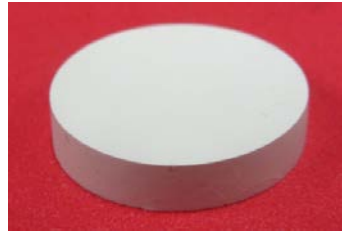
(a) Cellular silica sample
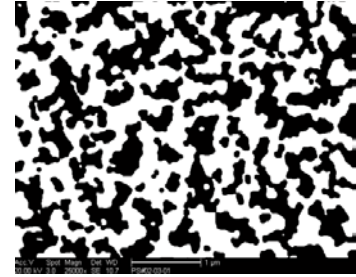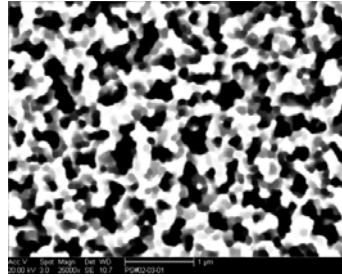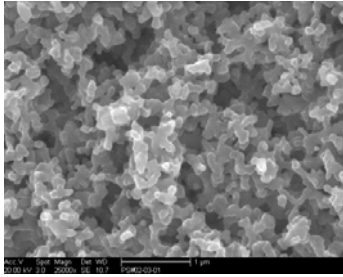
(b) Top, 52.5%
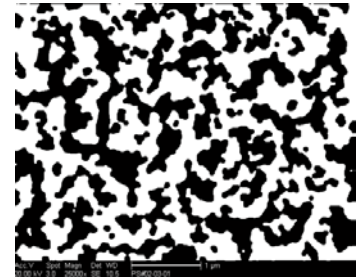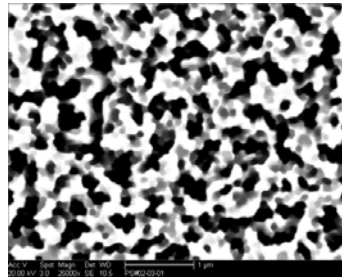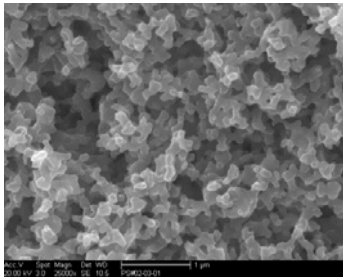
(c) Middle, 53.0%
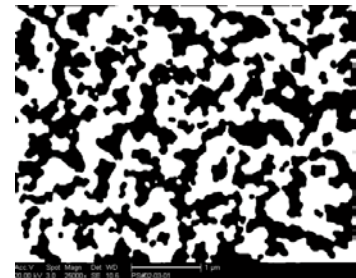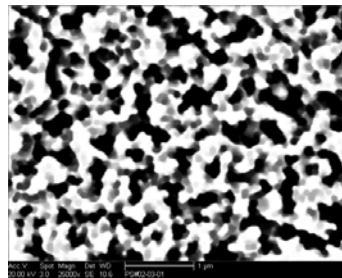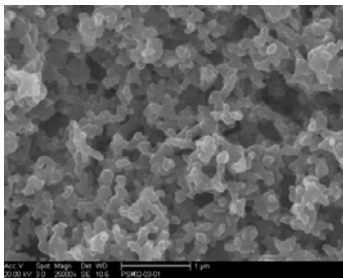
(d) Bottom, 52.7%

Figure 4.3: Morphology of a cellular silica sample. The percentages listed are the two-dimensional cell volume fractions of the scanned areas. The cell size is about 255 nm; the cell volume fraction is ~79%; the sample thickness is 5.0 mm.

(a) Before testing

(b) After testing

(c) Harvesting of a SEM sample
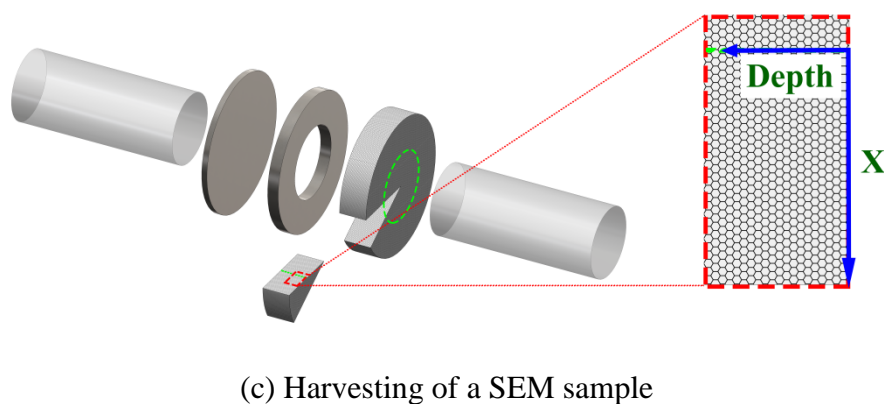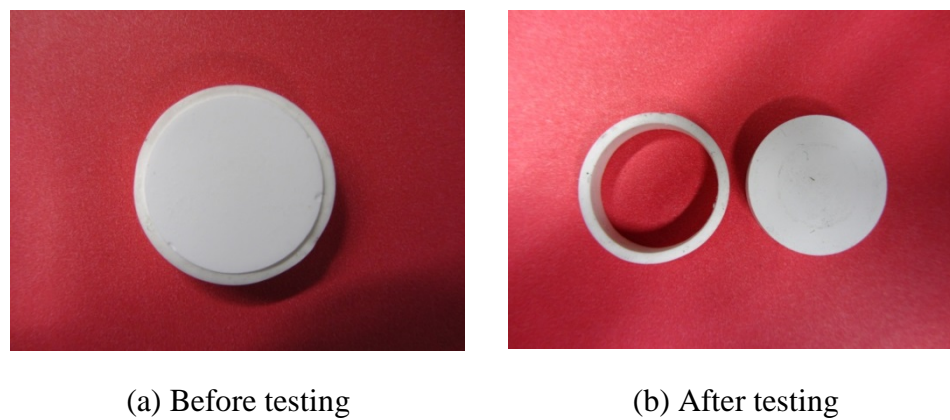
Figure 4.4: Forced-sheared cellular silica under the striker speed of 4 m/s.
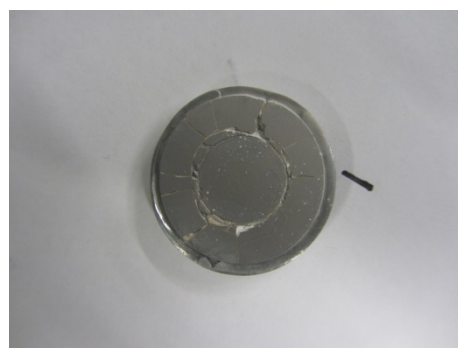
(a) Tested sample
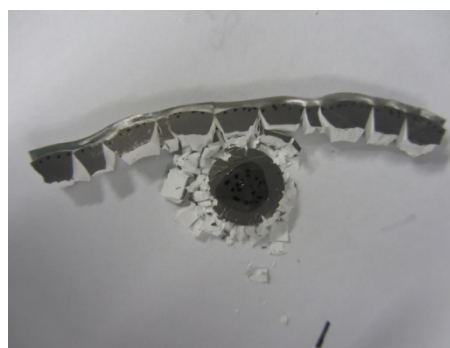
(b) After the rubber ring being removed

(c) Parts of interest
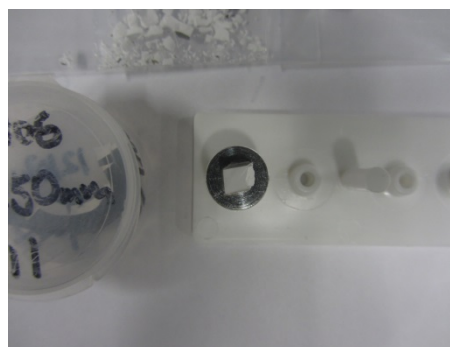
(d) Part #01
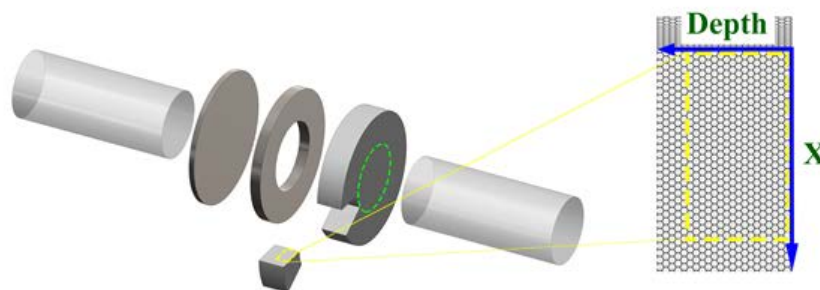
(e) Harvesting of SEM sample

Figure 4.5: Forced-sheared cellular silica under the striker speed of 8.5 m/s. The dark color on the surface of the SEM sample is caused by the iridium coating.
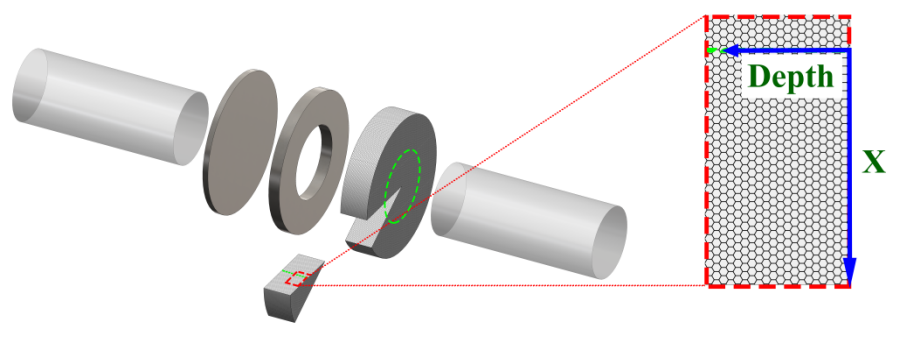
(a) Schematic of the scanning range
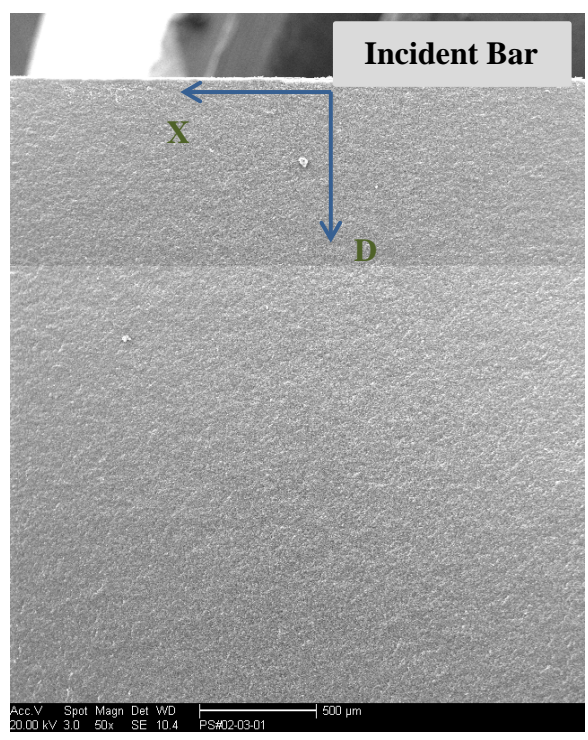
(b) A larger view
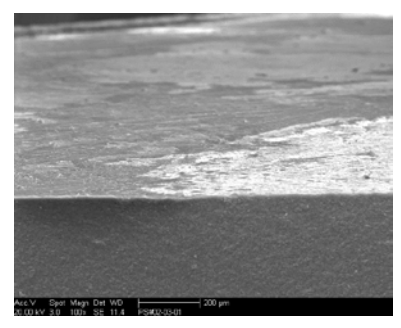
(c) Surface features
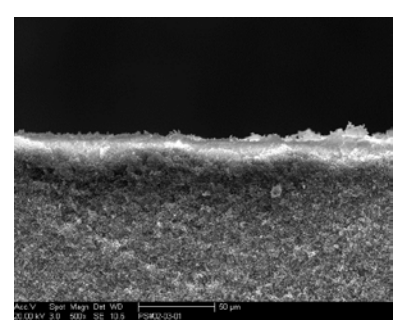
(d) A starting point

Figure 4.6: SEM scanning strategy.

CHAPTER 5

DYNAMIC SHEAR TESTS ON CELLULAR

SILICA

5.1.   Introduction

Under dynamic shear loadings, an intense stress wave can be highly nonlinear and highly heterogeneous (HNHH) (Meyers, 1994; Nesterenko, 2001). Its propagation, reflection, and transmission are coupled with the changes in the structure of the medium, and therefore, many concepts of linear wave theory, such as acoustic impedance and wave energy conservation, may break down. For example, as a HNHH stress wave advances in a solid material, it can cause plastic yielding, microcracking, and/or local phase transformation (Me-Bar and Shechtman, 1983; Meyers et al., 1994; Timothy and Hutchings, 1985; Xue et al., 2002); in a cellular material, it may trigger cell buckling and

ligament rupture (Balch et al., 2005); in a granular material, it can activate rearrangement of close-packed components (Daraio et al., 2006; Meyers et al., 2001). The nonlinearity is often associated with the heterogeneity (Pauly et al., 2010; Ritchie, 2011; Zener and Hollomon, 1944); that is, an initially uniform wave front may become heterogeneous and the wave energy is dissipated in a number of narrow zones, e.g. shear bands (Meyers et al., 2001; Meyers et al., 1994; Xu et al., 2008; Zhou et al., 1996). The instability of a HNHH stress wave can be caused by either material instability or geometrical instability (Nesterenko, 2001).

Cellular materials are solid materials having empty cells. A few examples of cellular materials include arrays of carbon nanotubes (Ajayan and Zhou, 2001) or nano/micro-wires (Rao and Govindaraj, 2011), ultra-lightweight microtrusses (Queheillalt and Wadley, 2005), and porous polymers, metals/alloys, and ceramics (Hedrick et al., 1999; Nakanishi, 2010; Tappan et al., 2010). In general, cellular materials are lightweight. They are widely applied for thermal insulation, acoustic damping, and impact protection (Gibson and Ashby, 1997; Scheffler and Colombo, 2006). In a cellular material, if a HNHH stress wave becomes unstable, catastrophic failure would take place, with the majority of the protection capacity being essentially wasted.

Over the years, the instability of HNHH stress wave was extensively investigated (Daraio et al., 2006; Leonard and Daraio, 2012; Meyers et al., 2001; Nesterenko, 2001; Nesterenko et al., 2005b; Porter et al., 2009; Starosvetsky and Vakakis, 2010; Theocharis et al., 2010) . Shear band nucleation, propagation, and morphology change were related to materials properties and loading modes. However, there is still no efficient way to stabilize and homogenize HNHH stress waves in cellular media.

For each material and loading condition, shear bands have a characteristic width, w, ranging from a few nm in metallic glass (Pekarskaya et al., 2001) to hundreds of μm in cellular materials (Balch et al., 2005) or granular materials (Alshibli and Sture, 1999; Nesterenko et al., 1996). According to the classic Grady model (Grady, 1982),

$$w \propto \sqrt{\frac{\Sigma}{\rho \dot{\varepsilon}^2}} \qquad (5.1)$$

where Σ is the energy dissipation density, ρ is the mass density of the medium, and $\dot{\varepsilon}$ is the strain rate. Equation (5.1) suggests that w is independent of the characteristic length of the medium.

In a regular cellular material where the cell size is relatively large (e.g. comparable with or larger than the characteristic shear-band width), the cell buckling at the HNHH stress wave front may be viewed as a process that reduces the resistance to shear banding; thus, wave energy dissipation tends to be limited within narrow bands. In the current study, we investigate cellular materials in which the cell sizes are relative small (e.g. much smaller than the characteristic size of shear deformation zone). Under this condition, cell buckling may become a fast condensation mechanism, which increases the effective local resistance. As the shear banding is suppressed, the wave front can be stabilized and homogenized.

5.2. Preparation of Cellular Silica Samples

The materials under investigation were a set of monolithic cellular silica samples with a similar cell volume fraction around 60%; their cell sizes were in the range from

tens of nm to more than 1 μm, as shown in Figure 5.1. Details of the material processing and characterization were documented in Chapter 2. The cell formation was achieved by sol-gel methods (Miyamoto et al., 2013; Nakanishi, 2010; Shoup, 1976); different templating agents were employed for small and large cells. Immediately after rinsing and drying, the material was subcritically calcinated at the temperatures slightly higher than the glass transition point. In this temperature range, the cell size and the cell volume fraction varied at distinct rates, and thus, were precisely and independently controlled. Moreover, the residual stresses were largely reduced. Through x-ray diffraction (XRD) analysis (Chapter 2), it was confirmed that all the samples were amorphous. The samples were processed as 4.5 mm thick disks, with the diameter ~23 mm, as listed in Table 5.1.

5.3. Experimental Measurements

5.3.1. Quasi-static Shear Tests

The cellular silica samples were first tested under quasi-static shear loading. A silica disk sample was sandwiched in between a stainless steel loading rod and a stainless steel shear-promotion support ring (SPSR). The inner diameter of the SPSR was 13.1 mm, slightly larger than the outer diameter of the loading rod, $2r = 12.7$ mm. By using a type 5582 Instron machine, the loading rod compressed the silica sample, with the loading rate of 0.01 mm/min. Shear instability was triggered by the geometrical change of the SPSR. Figure 5.2 shows typical load-displacement curves. The quasi-static shear strength is defined as $S_0 = F/(2\pi rt)$, where F is the measured peak loading at the onset of

shear failure and *t* is the sample thickness. Table 5.2 and Figure 5.3 show the quasi-static shear strength of cellular silica samples.

5.3.2. Dynamic Compression Tests

Dynamic compression tests on cellular silica samples were conducted by using the Split Hopkinson Bar (SHB) system described in Chapter 3. A 62.8 g titanium striker was projected by a gas chamber to a stainless steel incident bar. Upon impact, a high-pressure stress wave was generated and propagated along the incident bar (Kolsky, 1963). In all the tests, the striker speed was kept at ~8.5 m/s. On the other end of the incident bar, a cellular silica disk sample was firmly attached, supported by a stainless steel transmission bar from the back. The stress wave entered into the silica sample, and eventually transmitted to the transmission bar. The incident, reflected and transmitted wave profiles, as shown in Figure 5.4, were measured by the strain gauges mounted on the incident bar and the transmission bar, respectively. The incident wave profiles were similar in all the tests, and the transmitted wave pressures are summarized in Figure 5.5 and Table 5.2.

5.3.3. Dynamic Shear Tests

Dynamic shear tests were carried out by using a similar SHB system with the dynamic compression experiment. The striker, the incident bar, and the transmission bar were the same; the striker speed was maintained at ~8.5 m/s. The same SPSR in the quasi-static shear tests was employed; the shear gap width was set as 0.20 mm. This setup was inspired by the work of (Meyers et al., 1992; Meyers et al., 2001; Nesterenko, 2001):

While the stress wave in the incident bar was compressive, shear deformation would be promoted in a narrow circular band in between the outer surface of the incident bar and the inner surface of the SPSR. Due to the geometrical change, the stress wave in the silica sample was no longer homogeneous, but highly heterogeneous; i.e. its spatial distribution is non-uniform. Figure 5.6 shows the profiles of incident, reflected, and transmitted stress waves. Figure 5.7 and Table 5.2 summarize the measured transmitted wave pressure of cellular silica samples with different cell sizes.

To investigate the influence of the shear strain rate on the cell size effect, dynamic shear tests were also performed with different impact rates of the striker and different shear gap widths between the outer surface of the incident bar and the inner surface of the SPSR: with the shear gap width of 0.20 mm, the striker speed varied from ~5.0 m/s to ~9.5 m/s; with the striker speed of ~9.5 m/s, the shear gap width ranged from 0.10 mm to 0.40 mm. The testing results will be discussed in Section 5.5.

Finally, to investigate the influence of the cell volume fraction on the cell size effect, dynamic shear tests were conducted on cellular silica samples with the striker speed of ~9.5 m/s and the shear gaps width of 0.20 mm. The testing results will be discussed in Section 5.6.

5.3.4. Dynamic Shear Deformation Zone

After testing under the conditions of the striker speed of ~8.5 m/s and the shear gap width of 0.20 mm, the dynamically sheared silica samples were well preserved. Selected samples were cleaved along the radius direction, and the areas around the

circular bands of shear deformation in the exposed lateral surfaces were observed under a FEI-XL30 environmental scanning electron microscope (SEM), as depicted in Figure 5.8 (b). Figure 5.8 (c,d,e) show typical SEM images. According to the SEM image analysis algorithm, described in Chapter 4, the boundaries of shear deformation zones (SDZ) were determined. Outside SDZ, no permanent cell deformation could be detected. Inside SDZ, the cell volume fraction changed significantly. For self-comparison purpose, SDZ was defined as the areas where the local cell volume fraction differs from that in the far field by more than ~1 σ, with σ being the standard deviation. Table 5.3 listed the nominal two-dimensional cell volume fractions, $p_2{}^*$, of pristine cellular samples with various cell sizes.

5.4. Cell Size Effect

Figure 5.3 suggests that the quasi-static shear strength, S_0, is quite insensitive to the cell size, as predicted by the classic theory (Gibson and Ashby, 1997): The strength of a cellular material is determined by its cell volume fraction, p.

$$S_0 \propto (1-p)^2 \tag{5.2}$$

Since all the cellular silica disk samples in the current study have a similar cell volume fraction of ~60%, their shear strengths are at the same level.

In the dynamic SHB tests, because the striker speed is kept nearly constant, the incident wave profiles and pressures are similar for all the samples, as shown in Table 5.1. Under the incident wave pressure of ~31 MPa, in the dynamic compression tests, the cell deformation can be ignored; while in the dynamic shear tests, the cells collapse, and the stress wave is highly nonlinear.

The acoustic impedance (z) of a cellular silica sample is determined by

$$z = A \cdot \rho \cdot c \tag{5.3}$$

where A is the cross section area, ρ is the mass density, and c is the speed of sound. All the investigated cellular silica samples have a similar cell volume fraction, ~60%, indicating that their sample densities are similar. According to Figure 2.8 in Chapter 2, the speed of sound is almost a constant, regardless of the cell size. Thus, the acoustic impedance of cellular silica samples should be similar. On the other hand, dynamic compression tests were conducted, where the silica sample was sandwiched in-between the incident bar and the transmission bar directly. The stress wave in the incident bar is one-dimensional and homogeneous (Kolsky, 1963). When such a one-dimensional stress encounters an interface, part of it will get reflected and part of it will get transmitted. The extent of the impedance mismatch will determine the percentage of the energy that will get reflected or transmitted. In another word, we can check the reflected wave pressure or the transmitted wave pressure to confirm the acoustic impedance. As shown in Figure 5.5, the transmitted wave pressure is nearly constant in all the cellular silica samples, independent of the cell size. Therefore, the acoustic impedance of a cellular silica sample is not related with its cell size, d.

In the dynamic shear experiment, the stress wave is highly nonlinear and highly heterogeneous. Under this condition, as shown in Figure 5.7, the transmitted wave pressure becomes highly dependent on the cell size. As the cell size decreases from ~1.4 μm to ~300 nm, the transmitted wave pressure is lowered relatively mildly by nearly 1/3; as the cell size further decreases to ~100 nm, the transmitted wave pressure largely reduces by another ~30%. Overall, with the cell size around 100-200 nm, the transmitted

wave pressure is only ~1/3 of that of the large-cell-sized samples. In our experiment, the incident wave pressure and duration are maintained at the same levels; as the impedance of the material is unrelated to the cell size, the reflected wave profiles do not have a clear correlation with the cell size. The trend in transmitted waves must be associated with the structural changes in the cellular medium: As shown in Figure 5.8 (c,d,e), when the cell size decreases from above 300 nm to ~100 nm, the SDZ configuration undergoes a sharp transition. As the cell size is above 300 nm, the HNHH stress wave in the cellular silica exhibits typical unstable, concentrated characteristics. The cell deformation is focused in the narrow circular band between the outer surface of the incident bar and the inner surface of the SPSR. As the cell size is ~100-200 nm, the SDZ width abruptly increases. A much broader field of material is involved in the HNHH propagation, leading to a much larger volume of structural variation, V; that is, the HNHH stress wave propagation is stabilized and homogenized. Because more wave energy is dissipated, the transmitted wave pressure decreases with the cell size.

Under dynamic shear tests, the transmitted wave pressure is a function of the cell size. The homogenization of the HNHH stress wave occurs only when the cell size is relatively small. To identify the boundary where the homogenization starts, we define a pressure reduction factor (ς)

$$|\varsigma| = |P_{ts} - P_{t0}|/P_{t0} \qquad (5.4)$$

where P_{t0} is the equivalent maximum normal stress under quasi-static shear condition, equaling to the maximum force on the loading rod divided by the cross-sectional area. For the cellular silica with the cell volume fraction of ~60%, the measured P_{t0} is ~16.1 MPa. As shown in Figure 5.9, when $\varsigma > 0$ (ς^+), the maximum transmitted wave pressure

is higher than 16.1 MPa; this region is defined as the Regular Region; when $\varsigma < 0$ (ς^-), the maximum transmitted wave pressure is lower than 16.1 MPa; this region defined as the Nano Region. The boundary between the Regular Region and the Nano Region, ~200 nm, defines the point where the HNHH stress wave starts to be stabilized and homogenized with the striker speed of ~8.5 m/s and the shear gap width of 0.20 mm.

The capacity of energy dissipation may be described by the energy dissipation factor (β):

$$\beta = \frac{U_i - U_r - U_t}{U_i - U_r} \tag{5.5}$$

where U_i, U_r, and U_t are the energies carried by the incident, reflected, and transmitted waves, respectively. When a linear, one-dimensional (1D) stress wave propagates in an elastic medium, the stress wave energy (U) consists of two parts: the strain energy (U_s) associated with local deformation and the kinetic energy (U_k) associated with local particle velocity. The strain energy may be assessed as

$$U_s = A_b C_b / (2E_b) \cdot \int_0^T P_w^2 dt, \tag{5.6}$$

where A_b, C_b, E_b, P_w, and t are the cross-section area of the medium, the speed of sound, the Young's modulus of the medium, the wave pressure, and time, respectively (Song and Chen, 2006; Surani et al., 2005). The integration is performed over the pulse duration, T. The kinetic energy can be estimated as

$$U_k = \rho_b A_b C_b^3 / (2E_b^2) \cdot \int_0^T P_w^2 dt, \tag{5.7}$$

where ρ_b is the mass density. Thus, the stress wave energy (U)

$$U = U_s + U_k \tag{5.8}$$

$$= (A_bC_b/(2E_b) + \rho_b A_b C_b^3/(2E_b^2)) \cdot \int_0^T P_w^2 dt = \xi \cdot \int_0^T P_w^2 dt$$

where $\xi = A_bC_b/(2E_b) + \rho_b A_b C_b^3/(2E_b^2)$. For a linear elastic medium, $E_b = \rho_b C_b^2$; hence, $\xi = A_bC_b/E_b$. For the Split Hopkinson Bar (SHB) system used in the current investigation, $A_b = 126.7$ mm^2; $C_b = 5790$ m/s; $E_b = 196.5$ GPa. Therefore, the system constant $\xi = 3.73 \times 10^{-12}$ m^{5}N/s. Here, the definition of stress wave energy is only for self-comparison purpose.

The calculation results of the energy dissipation factor, β, were summarized in Figure 5.10 and Table 5.2. With a relatively large cell size above 1 μm, the energy dissipation is quite low; as the cell size decreases, β rapidly increases, and reaches the peak value as d is ~ 100 nm, consistent with the observed SDZ configurations.

The homogenization of the HNHH stress wave in small-cell-sized cellular silica should be attributed to the fast compaction of the cells. When a stress wave encounters a hard inclusion, its front may be dispersed to a broader field (Leonard and Daraio, 2012). The stress wave in the incident bar is homogeneous. Due to the geometrical change of this shear setup, the stress wave becomes highly heterogeneous. As the HNHH stress wave advances into the cellular sample, if the cell size is relative large (e.g. comparable with or larger than the characteristic size of the wave front), cell collapse leads to local "softening", which promotes wave instability (Dannemann and Lankford, 2000; Tan et al., 2005). If the cell size is relative small (e.g. much smaller than the characteristic size of the wave front), their collapse takes only a short period of time and effectively becomes a local compaction process. Therefore, shear localization is suppressed, and the wave front is stabilized and dispersed into the far field.

5.5.   Influence of Shear Strain Rate

Under quasi-static shearing, the shear strengths of all the SCC-treated cellular silica samples are similar; while under dynamic shearing, the transmitted wave pressure shows a remarkable cell size effect. Therefore, the shear strain rate must be an important factor. Effective shear strain rate equals to the difference between the particle velocities at both ends of the specimen, which is determined by the impact rate of the striker, divided by the shear gap width, which is determined by the difference between the outer radius of the incident bar and the inner radius of the support ring.

5.5.1.   Impact Rate of Striker

Figure 5.11 shows the relationship between the striker speed and the incident wave pressure. They are quite linear to each other, suggesting that the SHB system works well in the elastic domain. The slope of the regressed line is 3.83 MPa·m^{-1}·s. All the SCC-treated silica samples have a similar cell volume fraction, ~60%, and the shear gap width here is set to be 0.20 mm.

Figure 5.12 shows the transmitted wave pressure of cellular silica samples with various cell sizes, with the impact rate of the striker from ~5.0 m/s to ~9.5 m/s. As the impact rate is relatively low, there is no evident cell size effect, similar to the quasi-static shear test result. As the impact rate reaches ~6-8.5 m/s, evident cell size effect could be observed: As the cell size is reduced from above ~300 nm to below ~100 nm, the transmitted wave pressure significantly decreases, suggesting that the shear localization is effectively suppressed, and the front of the HNHH stress wave is stabilized and

homogenized. As the impact rate is ~9.5 m/s, the incident loading is so intense that some cellular silica samples have reached their capacity of energy dissipation; and thus, the information of cell size effect is partially lost.

The energy dissipation factor (β) is used to quantify the energy dissipation. The higher the energy dissipation factor, the more energy will be dissipated during the dynamic shearing process. As shown in Figure 5.13, with the impact rate increasing from ~5.0 m/s to ~9.5 m/s, the cell size effect is greatly influenced. Figure 5.14 and Table 5.4 show the results of silica samples with the average cell size of ~85 nm. As the striker speed increases from ~5.0 m/s to ~7 m/s, the energy dissipation factor rises somewhat linearly by more than 0.2 m^{-1}s, indicating that the homogenization of HNHH stress wave is a dynamic effect: Only when the stress wave is sufficiently intense, can the factor of cell size come in and affect the energy dissipation; when the loading rate is low, the behavior of the investigated cellular silica resembles that in a quasi-static test. When the striker speed further rises from ~8.5 m/s to ~9.5 m/s, the energy dissipation factor does not vary a lot, implying that the energy dissipation is close to saturation.

5.5.2. Shear Gap Width

Another parameter that affects the effective shear strain rate is the shear gap width, half of the difference between the outer diameter of the incident bar and the inner diameter of the SPSR. Here the impact rate of the striker is set to ~9.5 m/s, and the shear gap width varies from 0.10 mm to 0.40 mm. The SCC-treated cellular silica samples have a similar cell volume fraction of ~60%. As shown in Figure 5.15, when the gap width is

relatively large, there is no evident cell size effect, which is consistent with the previous results that under a low impact rate. When the gap width is 0.20 mm, the cell size effect becomes evident, but as discussed previously, the incident loading is so intense that the cell size effect is not fully reflected. When the gap width further decreases to 0.10 mm, the data scatter becomes large, suggesting that the sample alignment may be a major issue; thus, the measurement data of the transmitted wave pressure are non-conclusive. Nevertheless, the testing data for the gap widths of 0.40 mm and 0.20 mm agrees with the previous result that the cell size effect is promoted as the shear strain rate rises.

In Figure 5.16, with the decrease of the shear gap width from 0.4 mm to 0.2 mm, the energy dissipation factor shows the similar tendency that, at a higher shear strain rate, an evident cell size effect can be observed. When the gap width is 0.10 mm, the data scatter is large, probably owning to the difficulty in accurate alignment of the incident bar, the testing sample, the support ring, and the transmission bar.

5.6.   Influence of Cell Volume Fraction

The energy dissipation capacity (ϵ) can be estimated from *SV*, where *S* is the material strength and *V* is the volume of the material that undergoes structural changes. According to Equation (5.2), the strength of a cellular material is related to its cell volume fraction (*p*). The energy dissipation capacity caused by cell collapse can be written as

$$\epsilon \propto V_0 \cdot p \cdot (1-p)^2 \tag{5.9}$$

where V_0 is initial volume of the material. Thus, the energy dissipation density (Σ), energy dissipation per volume, can be assessed as

$$\Sigma \propto p \cdot (1 - p)^2 \tag{5.10}$$

On the one hand, the cell volume fraction should be as large as possible to increase the change in volume; on the other hand, the increased cell volume fraction will weaken the material. If it is assumed that the material strength is a constant during the collapse of the cells, then the optimum cell volume fraction associated with the maximum energy dissipation density is ~33%.

The above analysis is based on the classical quasi-static theory in which the deformation of the cells is uniform, and the cell size effect is not taken into consideration. According to the experimental data, for the cellular silica with the cell volume fraction of ~60%, as the cell size is relatively small (e.g. much smaller than the characteristic length of the wave front), the shear localization could be effectively suppressed owning to the local hardening ahead of the wave front, which should be related to the cell volume fraction. When the cell volume fraction ahead of the wave front is relative high, it might be difficult to fully achieve local hardening since the local compaction process takes a longer period of time; when the cell volume fraction is relative low, the time for the cell collapse becomes shorter, but the compressibility also decreases.

The cellular silica samples used for the cell volume fraction study were processed through the similar procedure described in Chapter 2, but were fired at different temperatures slightly higher than the glass transition point to obtain different cell volume fractions, ranging from ~50% to ~70%. As discussed in Chapter 2, compared with the cell volume fraction, the cell size was much less sensitive to the calcination temperature.

Thus, the cell sizes of silica samples with the same initial component mass ratio remained similar, regardless of the large difference in cell volume fraction. The shear gap width was set to 0.20 mm, and the impact rate of the striker was maintained at ~9.5 m/s.

Figure 5.17 shows the transmitted wave pressure of cellular silica samples with various cell sizes and various cell volume fractions. Overall, for the silica samples with a similar cell size, the transmitted wave pressure reduces with the increase in cell volume fraction; for the silica samples with a similar cell volume fraction, the transmitted wave pressure reduces with the decrease in cell size. When the cell size is within the range from ~70 nm to ~175 nm and the cell volume fraction is within the range from ~60% to ~70%, there is a valley (dark red) in the contour of the transmitted wave pressure, with the lowest value of ~10 MPa, suggesting that more energy has been dissipated.

Figure 5.18 shows the energy dissipation factor of cellular silica samples with various cell sizes and various cell volume fractions. The pattern is consistent with the transmitted wave pressure shown in Figure 5.17. When the cell size is within the range from ~70 nm to ~175 nm, and when the cell volume fraction is within the range from ~60% to ~70%, there is a peak in the contour of the energy dissipation factor, with the peak value slightly higher than 90%. The existence of this peak indicates that: (1) there is an optimal cell volume fraction to achieve the maximum energy dissipation; and (2) the cell volume fraction effect and the cell size effect are coupled.

5.7.   Grady Model in SPSR

Based on the equilibrium condition of dissipated energy and kinetic energy, Grady developed an analytical model to predict the width of shear deformation zone (Grady, 1982).

$$w \propto \sqrt{\frac{\Sigma}{\rho \dot{\varepsilon}^2}} \tag{5.1}$$

where Σ is the density of dissipated energy, ρ is the mass density of the medium, and $\dot{\varepsilon}$ is the strain rate. Following Grady's idea, we derived an equation in the case of SPSR. As shown in Figure 5.19, the diameter of the incident bar is D_b, the shear gap width is w, the global shear velocity is v_0, and the sample thickness is t. Before shear localization, it is assumed that a uniform velocity gradient exists across the shear deformation region: at $r = w + D_b/2$, the local velocity is zero; at $r = D_b/2$, the local velocity is v_0; at a location within the range of $[D_b/2, w + D_b/2]$, the local velocity is

$$v = \dot{\gamma} \cdot (\frac{D_b}{2} + w - r) \tag{5.11}$$

where the effective shear strain rate is

$$\dot{\gamma} = \frac{v_0}{w} \tag{5.12}$$

The local kinetic energy within the region of $[r, r+dr]$ is

$$dT' = \frac{1}{2} v^2 \cdot dm \tag{5.13}$$

where

$$dm = 2\pi r \cdot \rho \cdot t \cdot dr \tag{5.14}$$

The kinetic energy within the shear deformation zone is given by the integral,

$$T' = \int_{\frac{D_b}{2}}^{\frac{D_b}{2}+w} dT' = \pi t \rho \dot{\gamma}^2 \cdot \left(\frac{w^4}{12} + \frac{D_b \cdot w^3}{6}\right) \tag{5.15}$$

Here the width of the shear deformation zone is much smaller than the diameter of the incident bar,

$$\frac{w}{2} \ll D_b \tag{5.16}$$

Thus, the kinetic energy can be rewritten as

$$T' = \frac{\pi t \rho \dot{\gamma}^2 \cdot D_b \cdot w^3}{6} \tag{5.17}$$

In the framework of continuum mechanics, the local kinetic energy density is

$$T = \frac{T'}{D_b \pi t w} \tag{5.18}$$

and the interface area to volume ratio, A, is

$$A = \frac{2D\pi t}{D\pi t w} = \frac{2}{w} \tag{5.19}$$

Consequently, the local kinetic energy density can be

$$T = \frac{2\rho \dot{\gamma}^2}{3A^2} \tag{5.20}$$

The interface energy density is

$$\Gamma = \gamma_0 \cdot A \tag{5.21}$$

where γ_0 is the interface energy consumed during the shear localization process. The total energy density is given by

$$E(A) = \frac{2\rho \dot{\gamma}^2}{3A^2} + \gamma_0 \cdot A \tag{5.22}$$

The energy terms are plotted in Figure 5.20. Clearly, the kinetic energy term results in inertial forces that tend to increase the interface area; while the interface energy term

provides driving forces that tend to suppress the formation of interface area. At equilibrium, the system free energy reaches the minimum value:

$$\frac{\mathrm{d}E(A)}{\mathrm{d}A} = 0 \tag{5.23}$$

The associated interface area is

$$A^3 \propto \frac{\rho\dot{\gamma}^2}{\gamma_0} \tag{5.24}$$

and the width of shear deformation zone is

$$w \propto \left(\frac{\gamma_0}{\rho\dot{\gamma}^2}\right)^{1/3} \tag{5.25}$$

If we assume that the energy dissipation occurs within the shear deformation zone, the energy dissipation density (Σ) can be estimated from

$$\gamma_0 = \Sigma \cdot w \tag{5.26}$$

Combination of Equations (5.25) and (5.26) leads to Equation (5.1).

5.8.   Dimensional Analysis for Shear Deformation Zone Size

For the nano-cellular silica under investigation, the testing data showed clearly that the cell size, d, has important effects on the size of the deformation zone. However, in Grady model, there is no such a length scale. Here the factor of the cell size is introduced, and we have

$$w = f(\Sigma, \rho, \dot{\varepsilon}, d) \tag{5.27}$$

where f is a certain function. According to the Π theorem (Bridgman, 1922),

$$w/d = f(\frac{\Sigma}{\rho \dot{\varepsilon}^2 d^2}) \tag{5.28}$$

If f is set to a power law form, Equation (5.28) becomes

$$w/d = \alpha \left(\frac{\Sigma}{\rho \dot{\varepsilon}^2 d^2}\right)^{\chi} \tag{5.29}$$

where α and $\chi \geq 1/2$ are two dimensionless material parameters. Equation (5.29) can be rewritten as

$$w = \alpha \left(\frac{\Sigma}{\rho \dot{\varepsilon}^2}\right)^{\chi} \cdot d^{1-2\chi} \tag{5.30}$$

When $\chi = 1/2$, Equation (5.30) converges to Grady model, and the cell size effect vanishes. As $\chi > 1/2$, the deformation zone size, w, increases as the cell size, d, decreases, agreeing with our experimental observation. As shown in Figure 5.21, through data fitting, the value of χ can be determined as 1.6 ± 0.1, or ~1.5. In Figure 5.21, the shear deformation zone (SDZ) sizes were measured from the SEM images in Figure 5.8.

5.9. Summary and Conclusion

We investigated the transmission of intense stress waves across subcritically calcinated cellular silica, with the cell size ranging from ~50 nm to ~1 μm and the cell volume fraction of ~60%. The experimental results showed that as the cell size was relatively large, the stress wave energy was dissipated in narrow bands, fitting well with classic theory; as the cell size was below ~200 nm, however, the stress wave was homogenized, and consequently, the transmitted wave pressure was significantly reduced. We attribute this unique phenomenon to the fast compaction of the small cells at the

wave front. With the shear localization being suppressed by the local hardening ahead of the wave front, the HNHH stress waves were stabilized and bulk energy dissipation is promoted.

The influence of the shear strain rate was also investigated. The results suggested that the homogenization of HNHH stress wave is a dynamic effect: Only when the shear strain rate is sufficiently high, can the factor of cell size come in and affect the energy dissipation; when the shear strain rate is low, the behavior of the investigated cellular silica resembles that in a quasi-static test.

The experiments on the influence of cell volume fraction showed that under a specific shear strain rate, there is an optimal cell volume fraction at which the energy dissipation is maximized. Only when the cell volume fraction is appropriate can the local hardening ahead of the wave front be fully achieved.

Grady model was modified via using dimensional analysis to include the cell size effect. In the new model, the size of the shear deformation zone increases as the cell size is reduced, matching well with the experimental observation.

Chapter 5, in part, has been submitted for publication in Physical Review Letters, and co-authored by Meng Wang, Yang Shi, Jian Luo, and Yu Qiao; in part, is currently being prepared for submission for publication of the material, and co-authored by Yu Qiao. The dissertation author was the primary investigator and author of this work.

Table 5.1: Key parameters of the cellular silica samples

Cell size (nm)	1380±600	315±75	240±50	185±35	155±25	120±20	85±15	70±10	50±10
Diameter (mm)	22.9±0.9	22.6±0.1	22.3±0.3	22.6±0.4	22.6±0.2	23.5±0.3	23.0±0.3	23.7±0.5	24.2±0.3
Thickness (mm)	4.51±0.02	4.51±0.01	4.53±0.01	4.51±0.01	4.53±0.01	4.53±0.01	4.51±0.01	4.52±0.01	4.52±0.01
Cell Volume Fraction (%)	59.6±2.7	62.7±0.9	61.6±0.9	60.7±1.2	59.5±0.8	62.4±1.4	59.1±2.0	60.0±1.5	60.0±1.3
Incident Wave Pressure (MPa)	32.7±0.6	32.3±0.6	31.4±1.2	31.1±0.4	31.3±0.6	32.7±0.6	29.1±0.3	31.3±0.5	31.6±0.2

Table 5.2: Testing results of cellular silica samples

Cell size (nm)	1380±600	315±75	240±50	185±35	155±25	120±20	85±15	70±10	50±10
p (%)	59.6±2.7	62.7±0.9	61.6±0.9	60.7±1.2	59.5±0.8	62.4±1.4	59.1±2.0	60.0±1.5	60.0±1.3
P_i (MPa)	32.7±0.6	32.3±0.6	31.4±1.2	31.1±0.4	31.3±0.6	32.7±0.6	29.1±0.3	31.3±0.5	31.6±0.2
S_0 (MPa)	10.8	12.7	11.7	10.5	9.8	10.8	9.0	14.6	12.0
P_{tc} (MPa)	29.9	30.0	30.1	29.6	30.6	28.6	29.4	28.3	28.5
P_{ts} (MPa)	29.3±4.1	17.8±1.9	16.4±1.5	11.9±0.9	13.4±0.1	10.5±0.8	11.2±1.0	11.0±1.4	13.8±1.0
β	0.35±0.14	0.75±0.04	0.82±0.02	0.87±0.02	0.85±0.01	0.90±0.01	0.89±0.02	0.89±0.01	0.82±0.01

Table 5.3: Image analysis results of pristine cellular silica samples

Cell size (nm)	315±75	240±50	185±35	155±25	120±20	85±15
p (%)	63.0	62.1	62.9	60.6	63.5	62.4
p_2^* (%)	52.4±0.8	50.8±1.0	50.7±1.3	50.4±0.6	52.4±0.8	50.4±0.8

Table 5.4: Influence of the impact rate of striker on the cell size effect.

Impact velocity (m/s)	5.2±0.1	6.0±0.1	6.9±0.3	8.6±0.1	9.3±0.2
Impact energy (J)	0.84±0.02	1.14±0.04	1.50±0.11	2.33±0.55	2.67±0.12
Incident wave pressure (MPa)	18.6±0.4	23.1±0.4	24.9±1.0	29.1±0.3	35.0±0.6
Transmitted wave pressure (MPa)	17.4±1.4	14.5±1.0	9.2±0.9	11.2±1.0	12.0±1.1
Energy dissipation factor, β	0.39±0.04	0.56±0.06	0.82±0.09	0.89±0.02	0.91±0.01
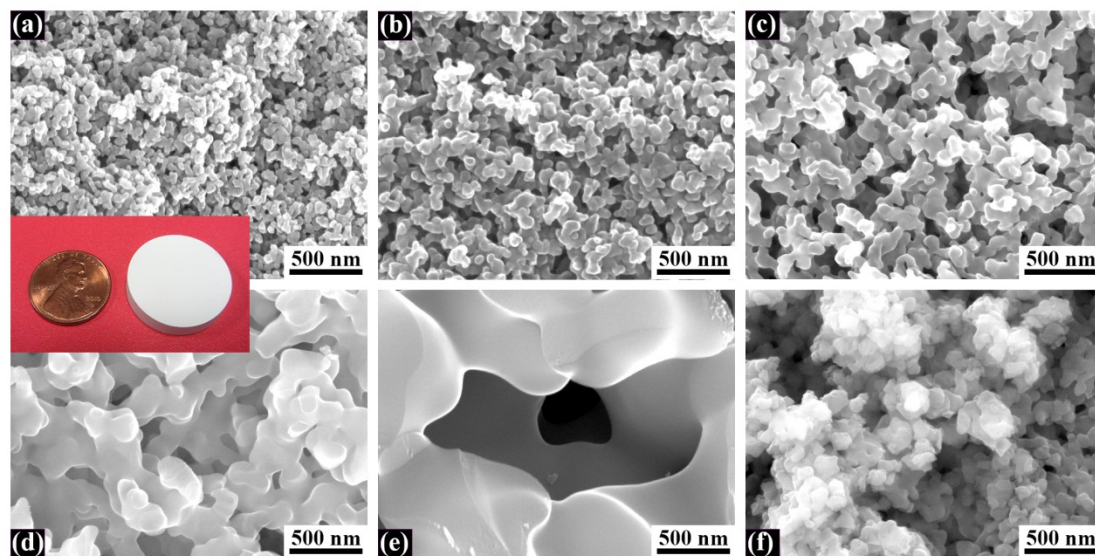
Figure 5.1: SEM images of cellular silicas with the average cell sizes of (a) 50 nm, (b) 85 nm, (c) 155 nm, (d) 315 nm and (e) 1.4 μm, respectively. The cell volume fraction of all the samples is around 60%. The inset between (a) and (d) shows a photo of a cellular silica disk sample. (f) SEM image of typical deformed cells after dynamic shear testing; the initial cell size is 155 nm.
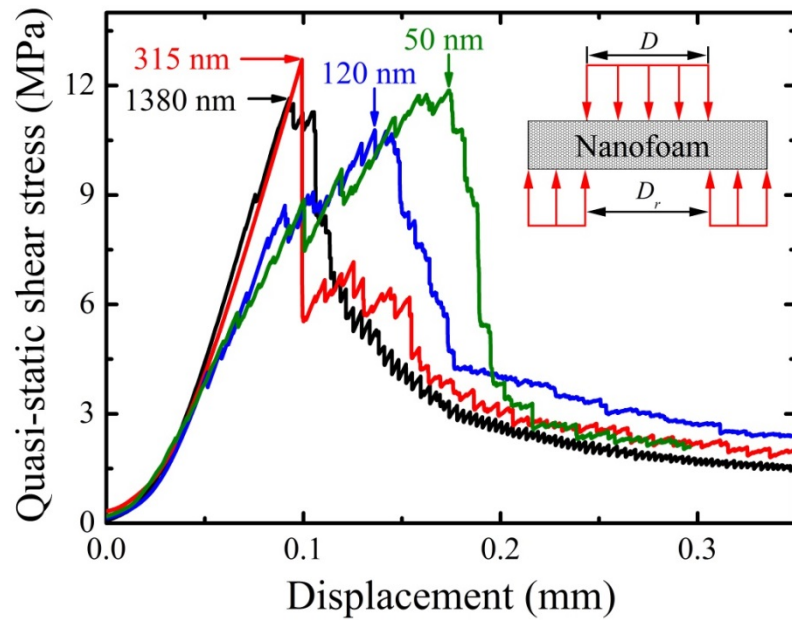
Figure 5.2: Typical quasi-static load-displacement curves; the arrows indicate the average cell sizes. The outer diameter of the loading rod is $D = 12.7$ mm; the inner diameter of the support ring is $D_r = 13.1$ mm. The loading/unloading rate is 0.01 mm/min. The cell volume fraction is ~60%.
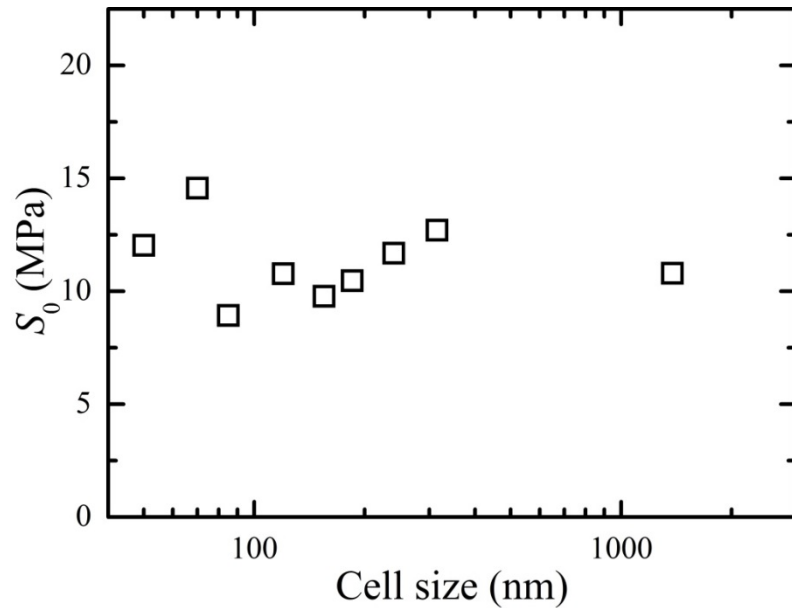
Figure 5.3: Quasi-static shear strength, S_0, as a function of the average cell size. The loading/unloading rate is 0.01 mm/min. The cell volume fraction is ~60%.
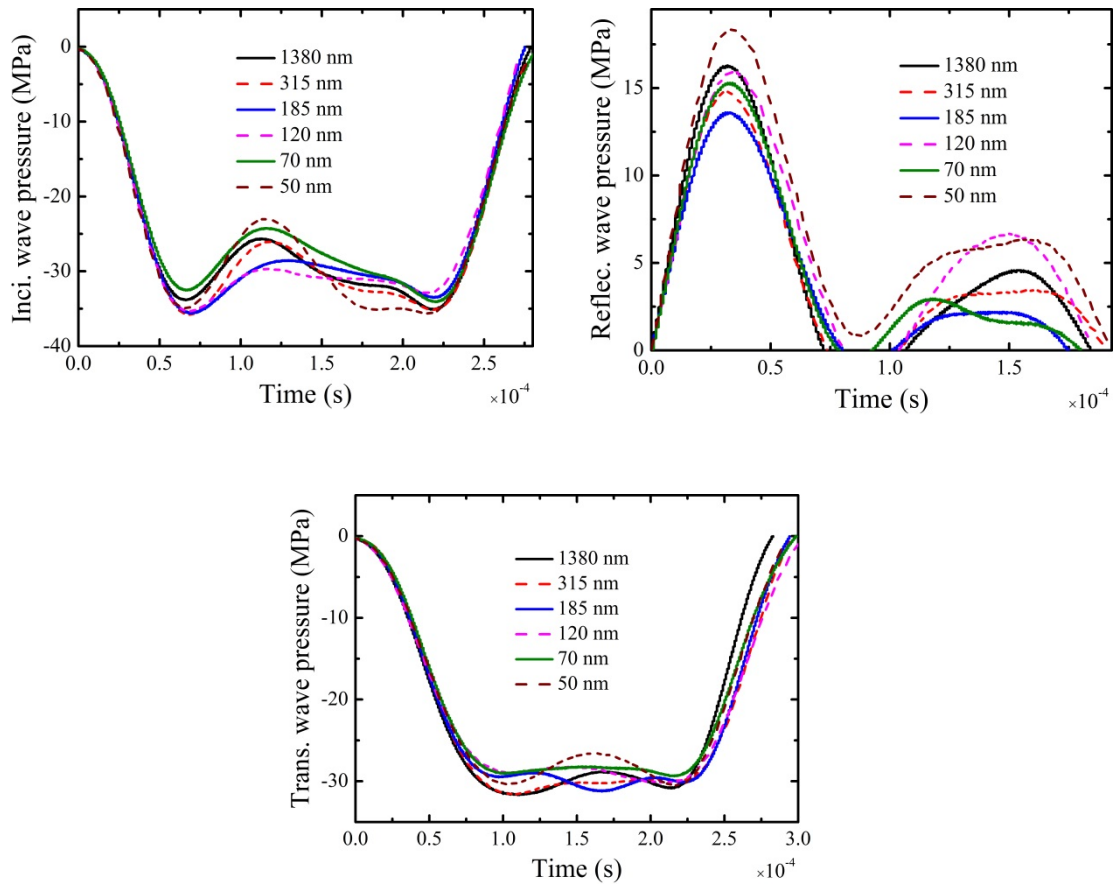
Figure 5.4: Typical incident (upper left), reflected (upper right) and transmitted (bottom) stress waves measured in the dynamic compression tests. The legends show the average cell sizes. The impact rate of striker is ~8.5 m/s. The cell volume fraction is ~60%.
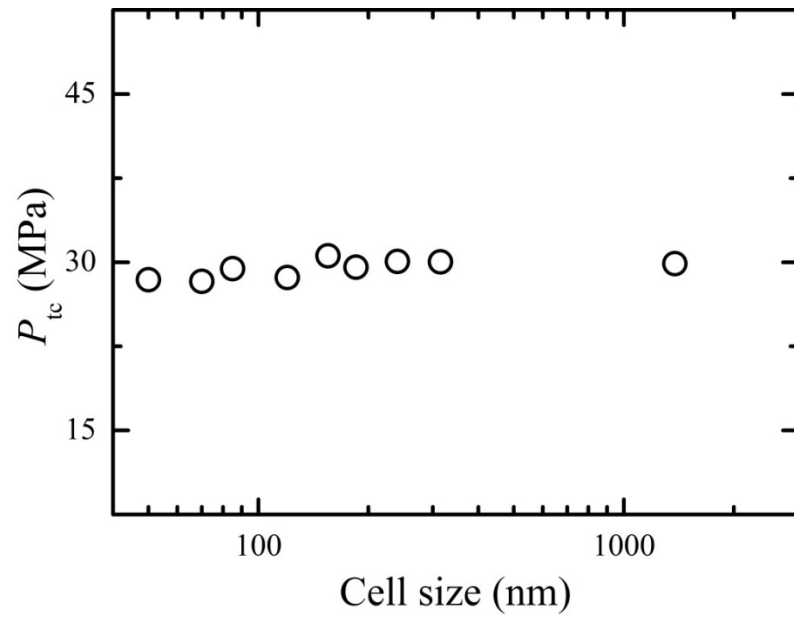
Figure 5.5: The transmitted compressive wave pressure, P_{tc}, as a function of the average cell size. The impact rate of striker is ~8.5 m/s. The cell volume fraction is ~60%.
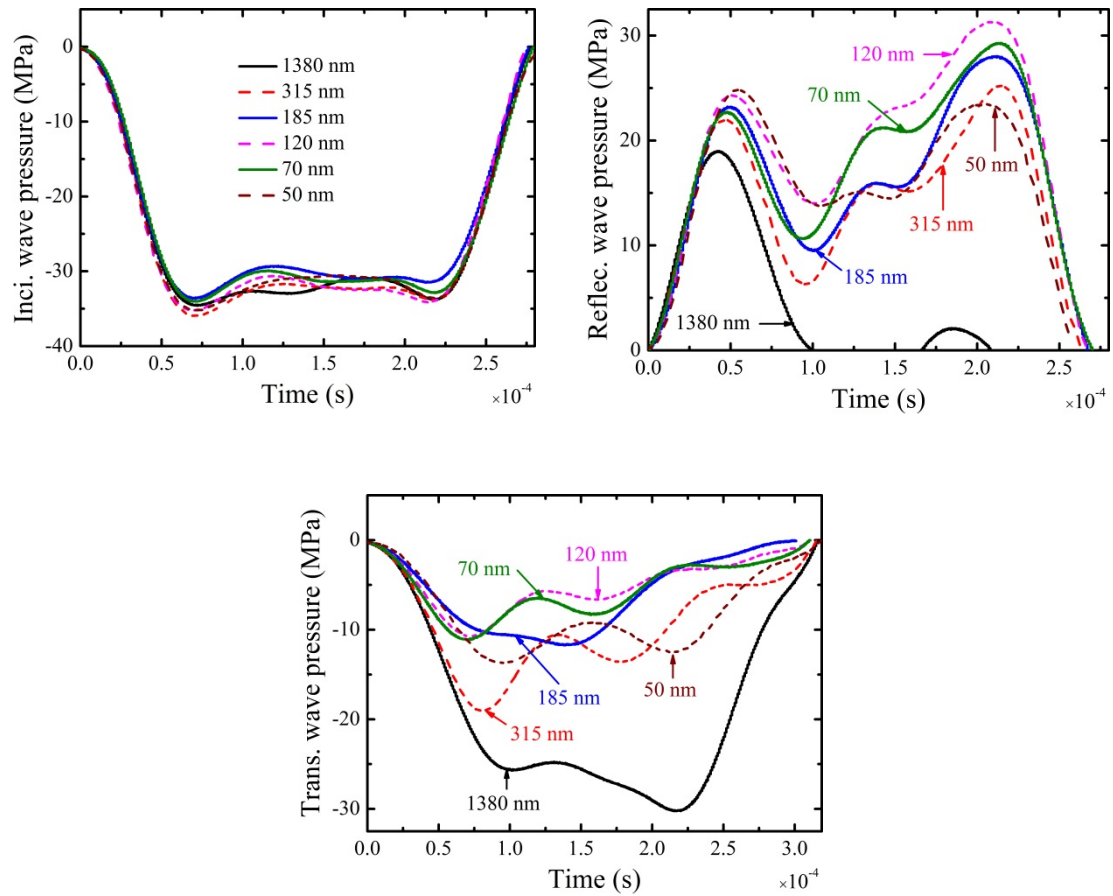
Figure 5.6: Typical incident (upper left), reflected (upper right) and transmitted (bottom) stress waves measured in the dynamic shear tests. The legends show the average cell sizes. The shear gap width is 0.20 mm. The impact rate of striker is ~8.5 m/s. The cell volume fraction is ~60%.
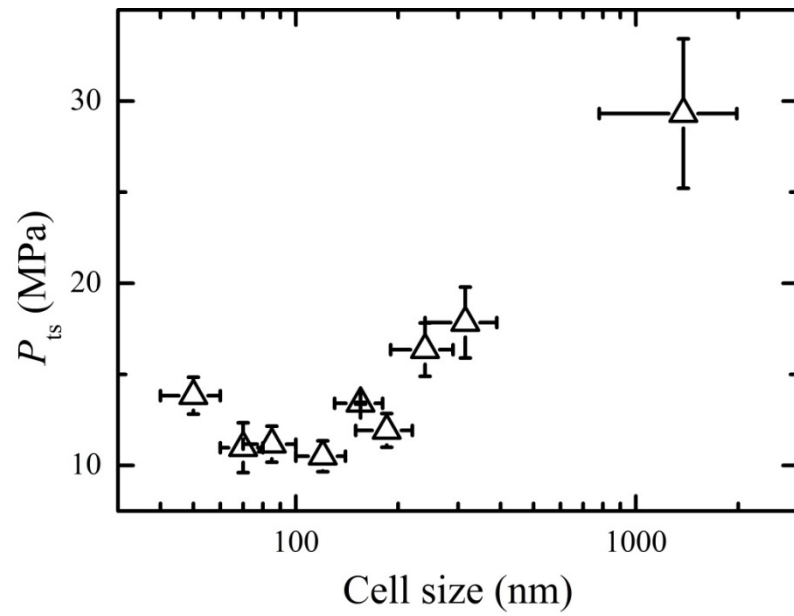
Figure 5.7: The transmitted wave pressure, P_{ts}, as a function of the average cell size. The shear gap width is 0.20 mm. The impact rate of striker is ~8.5 m/s. The cell volume fraction is ~60%.

(a)

(b)

(c)

(d)

(e)
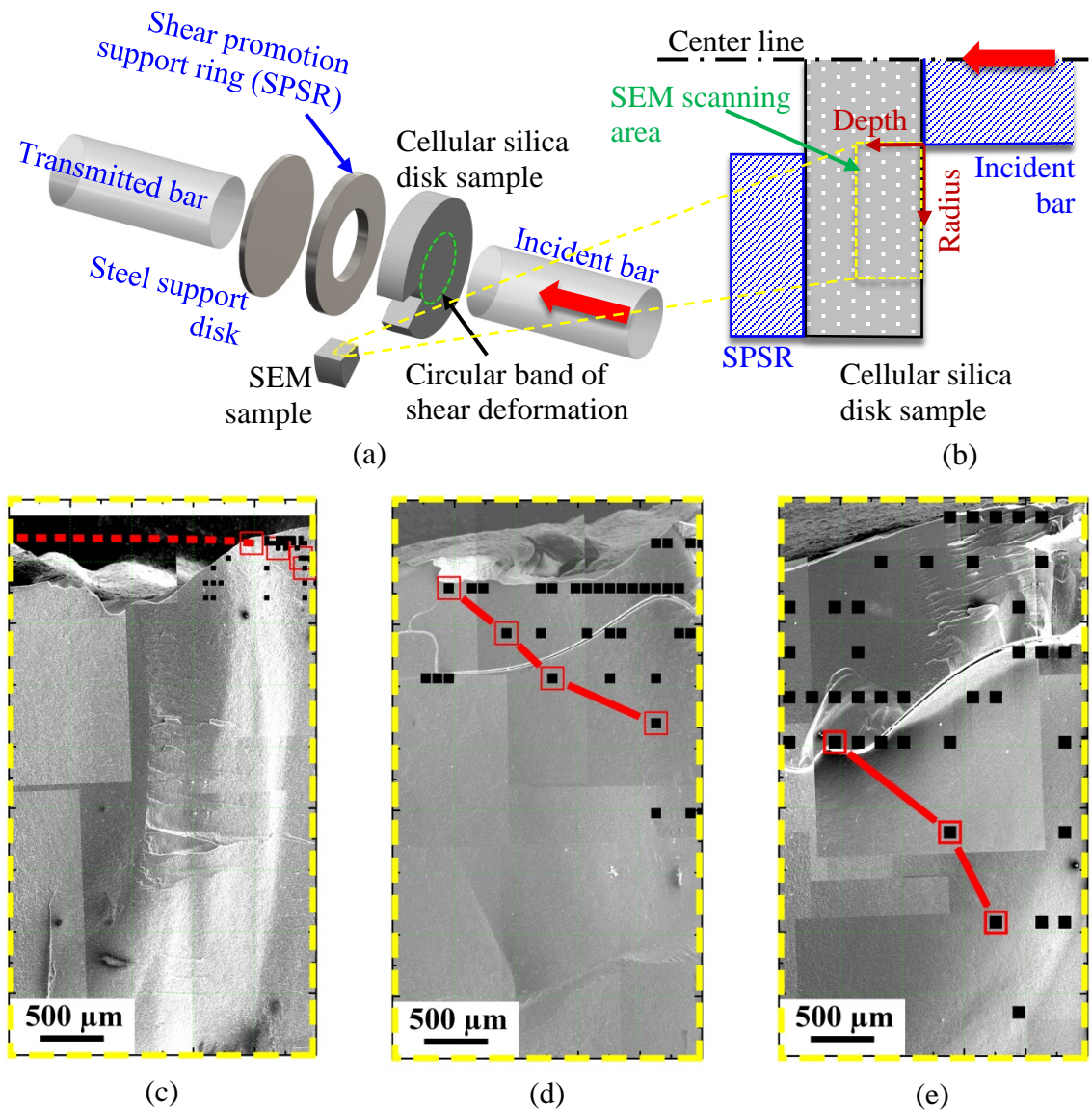
Figure 5.8: Schematics of (a) the SHB experimental setup for the dynamic shear test, and (b) the scanning area (yellow dashed rectangle) in a SEM sample harvested from a tested cellular silica disk. SEM images of tested cellular silica samples with the average cell sizes of (c) 315 nm, (d) 155 nm, and (e) 120 nm, respectively. The black squares indicate the local areas of deformed cells; the red squares and the red lines define the boundaries of the shear deformation zones (SDZ). The shear gap width is 0.20 mm. The impact rate of striker is ~8.5 m/s. The cell volume fraction is ~60%.
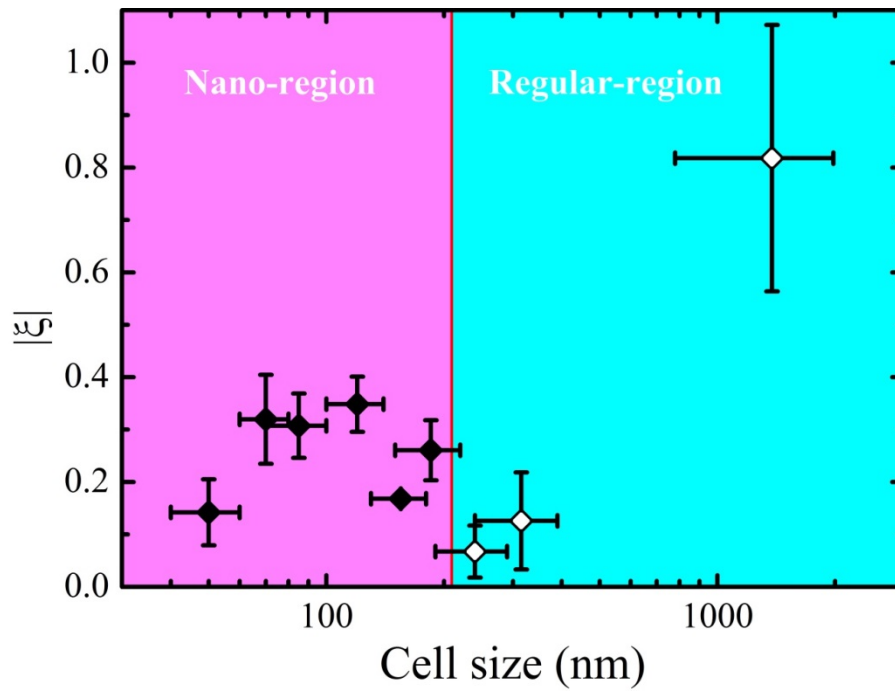
Figure 5.9: Pressure reduction factor under the dynamic shear tests. The shear gap width is 0.20 mm. The impact rate of striker is ~8.5 m/s. The cell volume fraction is ~60%. The entire cell size range under investigation is divided into two regions: Nano-region (solid diamonds with magenta background) and Regular-region (open diamonds with cyan background).
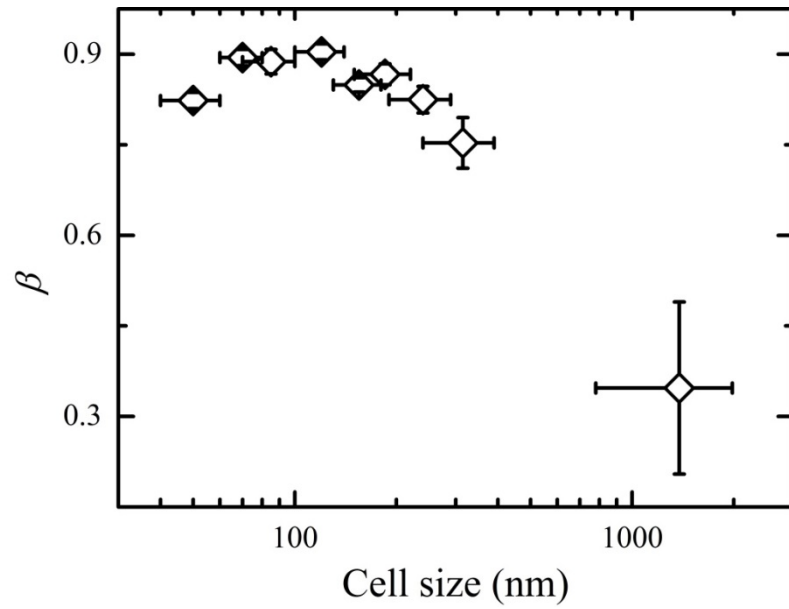
Figure 5.10: The energy dissipation factor, *β*, as functions of the average cell size. The shear gap width is 0.20 mm. The impact rate of striker is ~8.5 m/s. The cell volume fraction is ~60%.
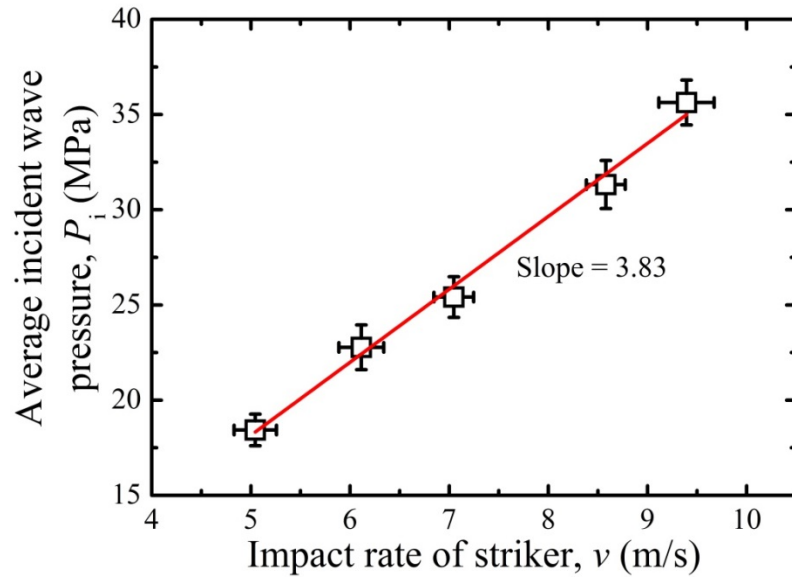
Figure 5.11: Relationship between the impact rate of striker and the average incident wave pressure.
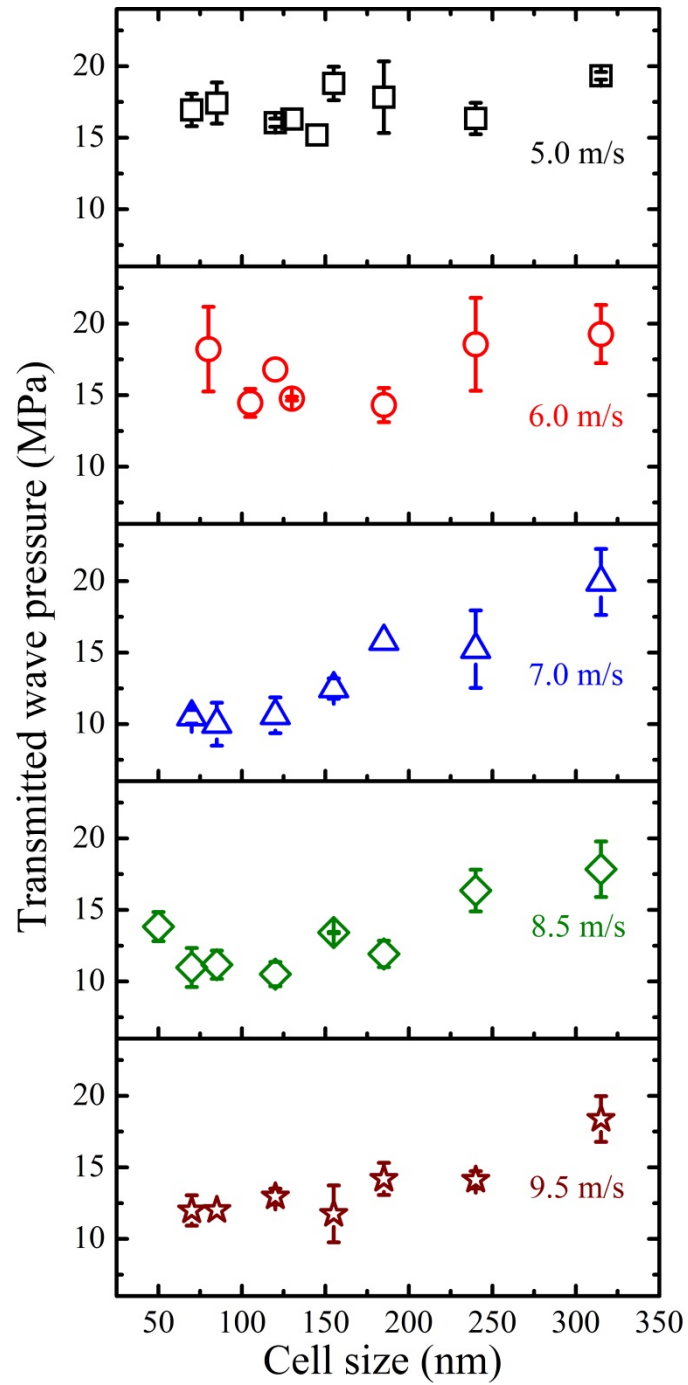
Figure 5.12: Transmitted wave pressure of SCC-treated cellular silica under different impact rates of the titanium tube striker. The shear gap width is 0.20 mm. The cell volume fraction is ~60%.
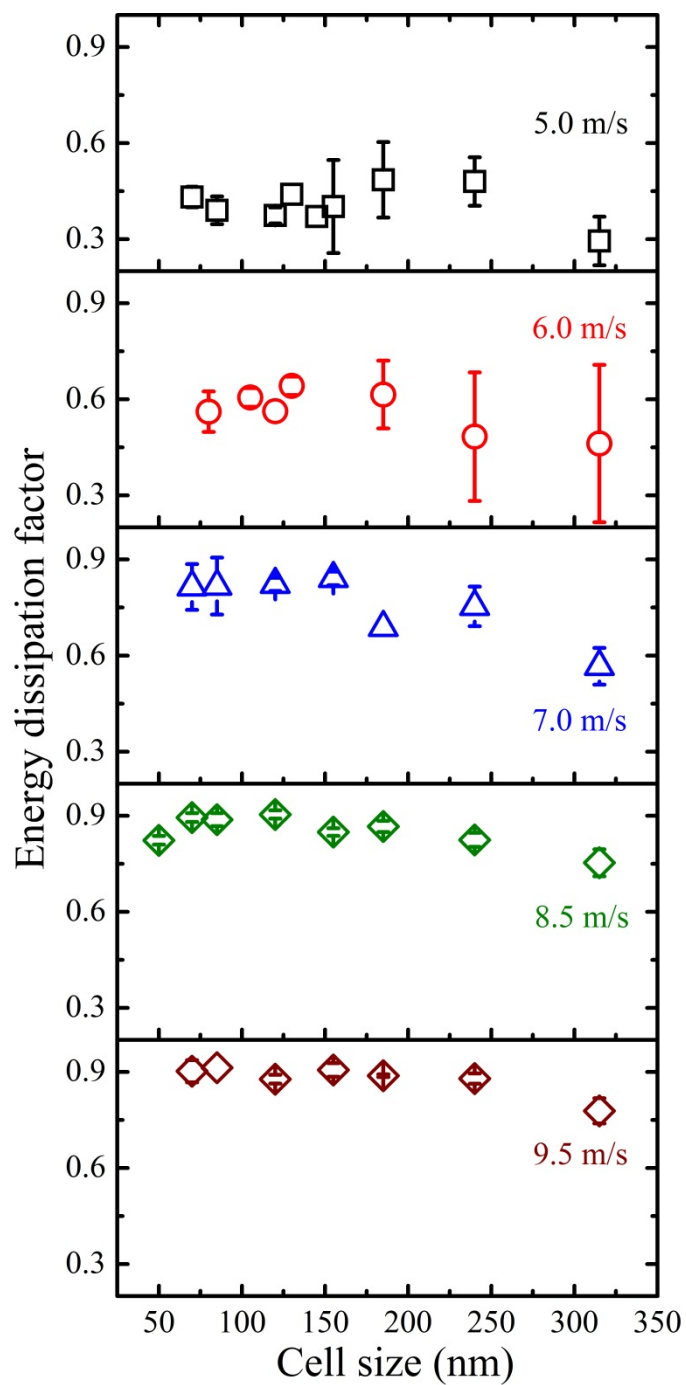
Figure 5.13: Energy dissipation factor of SCC-treated cellular silica under different impact rates of the titanium tube striker. The shear gap width is 0.20 mm. The cell volume fraction is ~60%.
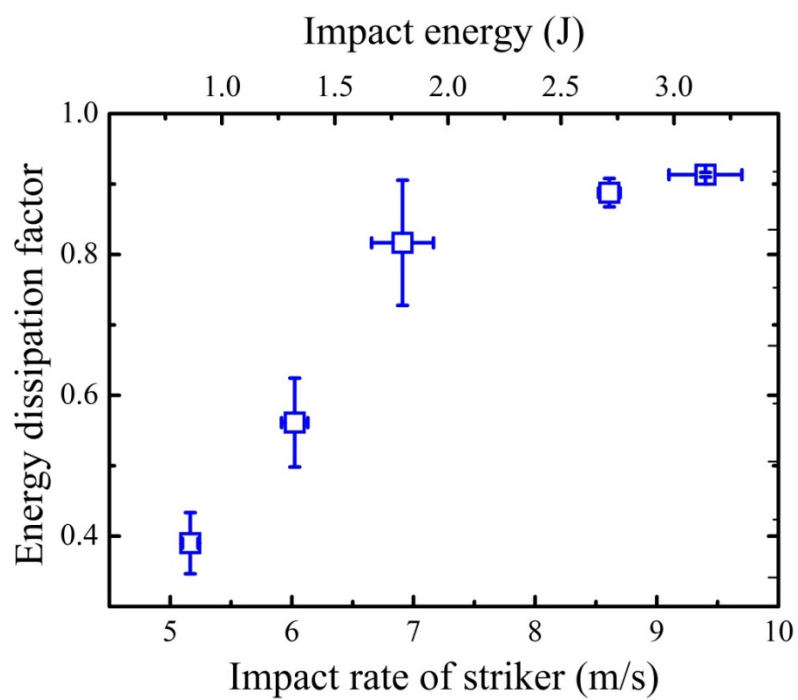
Figure 5.14: Energy dissipation factor of SCC-treated cellular silica with the average cell size of 85 nm. The shear gap width is 0.20 mm. The cell volume fraction is ~60%.
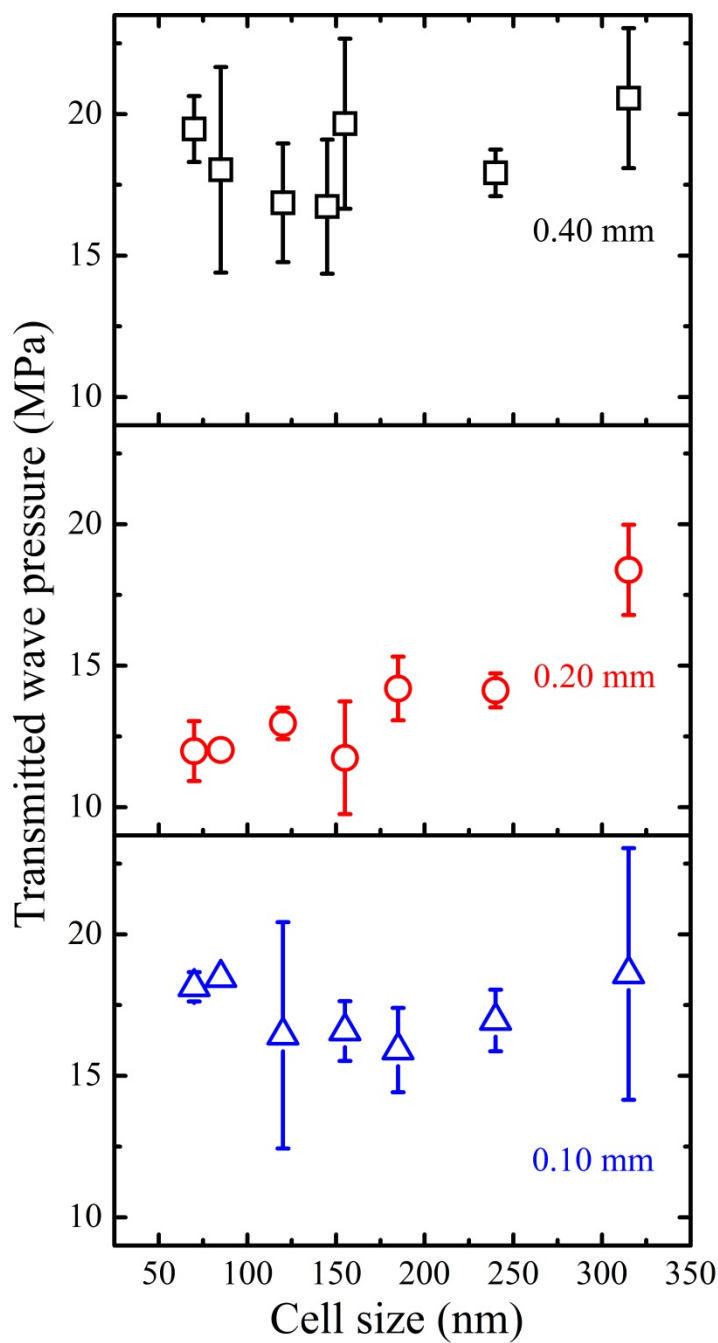
Figure 5.15: Transmitted wave pressure of SCC-treated cellular silica under different shear gap widths. The impact rate of striker is ~9.5 m/s. The cell volume fraction is ~60%.
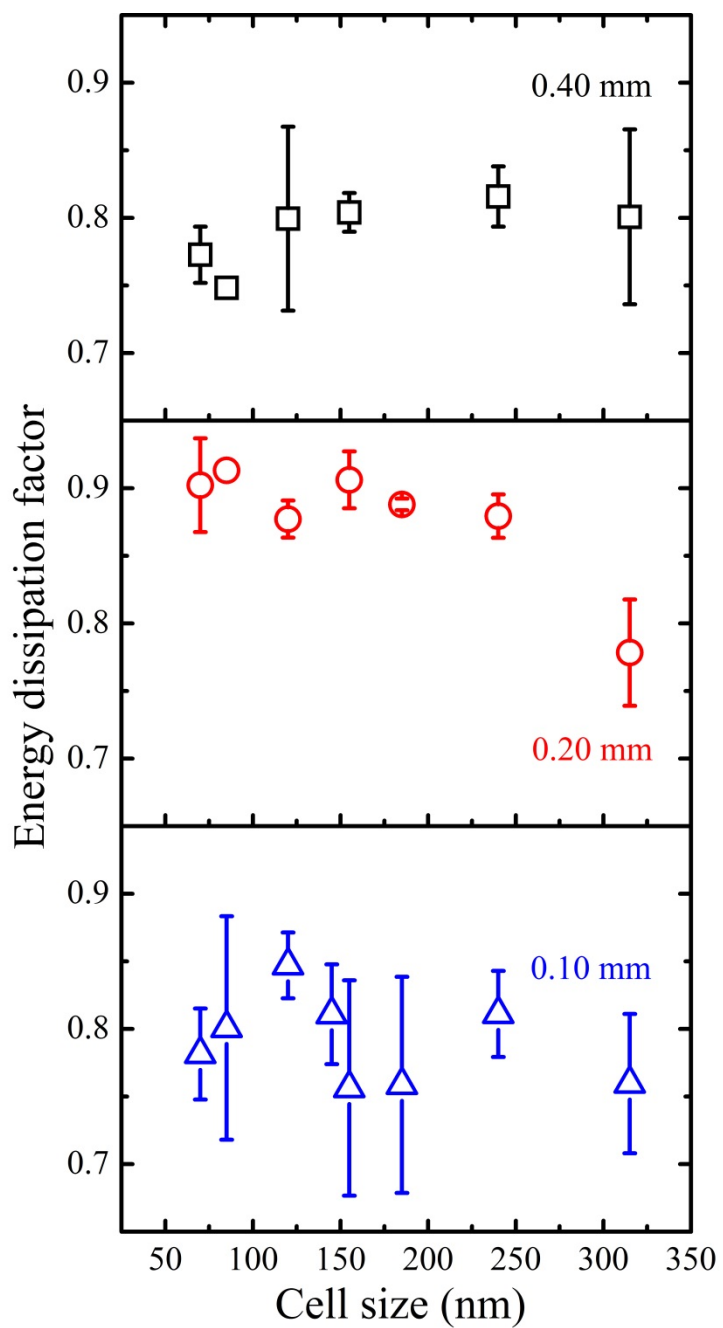
Figure 5.16: Energy dissipation factor of SCC-treated cellular silica under different shear gap widths. The impact rate of striker is ~9.5 m/s. The cell volume fraction is ~60%.
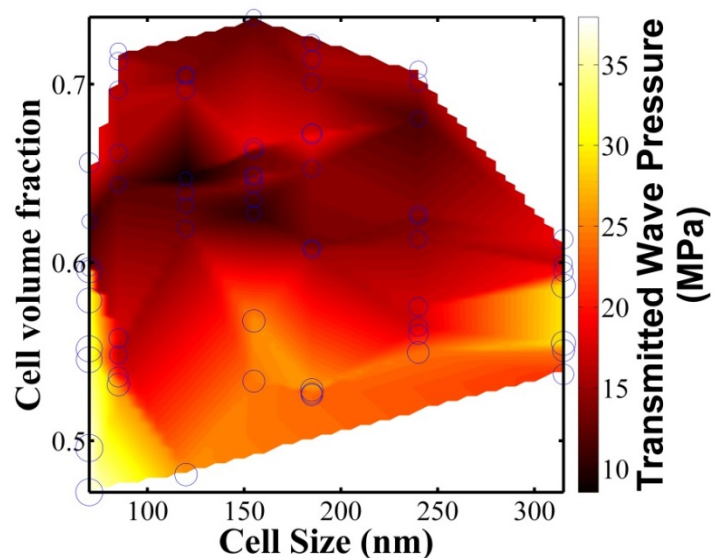
Figure 5.17: Transmitted wave pressure of SCC-treated cellular silica with various cell volume fractions. The blue circles show the experimental data. The impact rate of striker is ~9.5 m/s. The shear gap width is 0.20 mm.
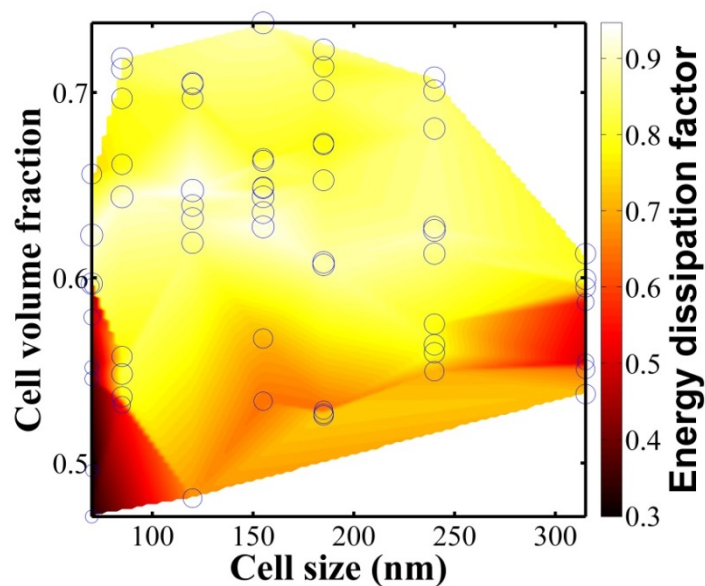
Figure 5.18: Energy dissipation factor of SCC-treated cellular silica with various cell volume fractions. The blue circles show the experimental data. The impact rate of striker is ~9.5 m/s. The shear gap width is 0.20 mm.
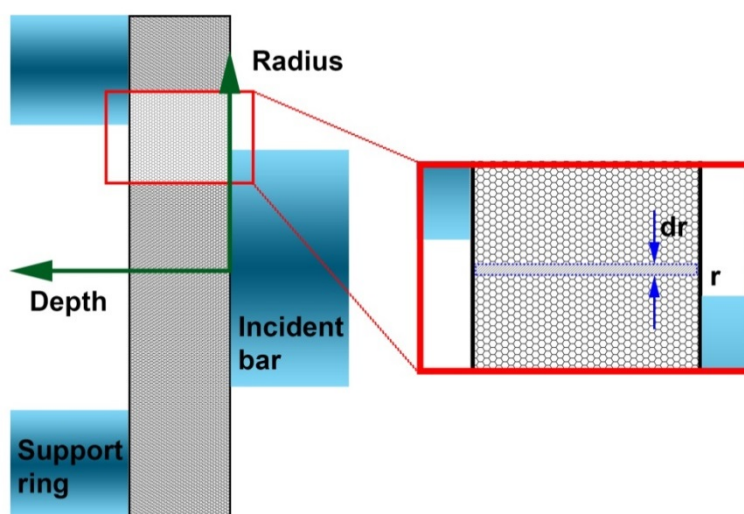
Figure 5.19: Schematic of shear deformation zone for the derivation of shear band width under dynamic loading.
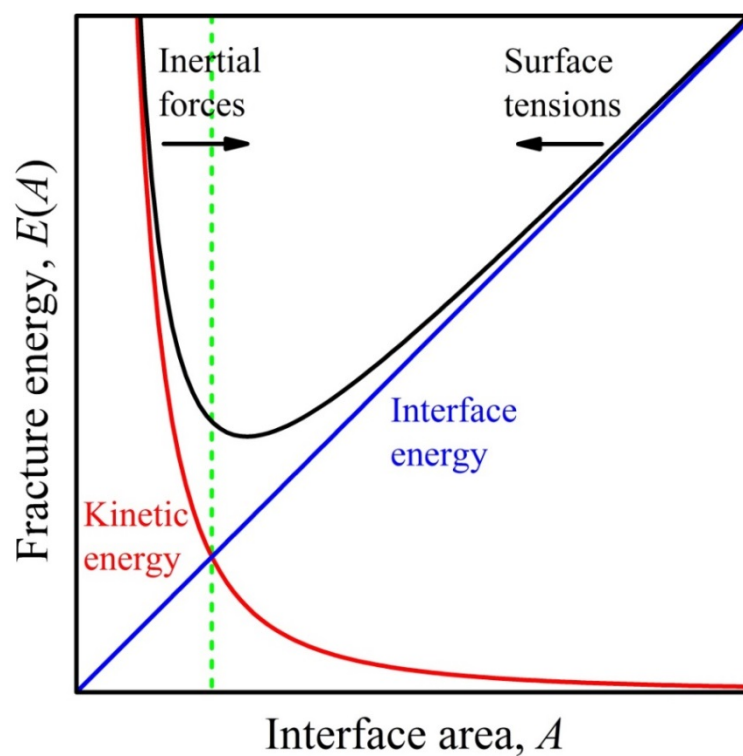
Figure 5.20: Equilibrium between kinetic energy and interface energy.
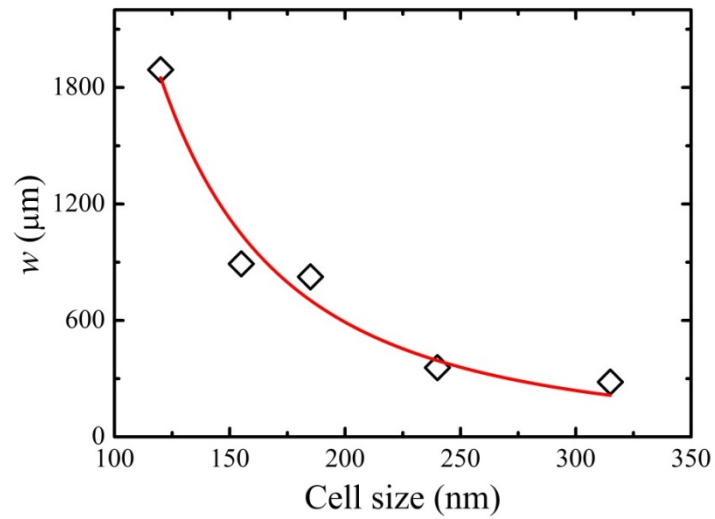
Figure 5.21: The average shear deformation zone (SDZ) size, *w*, as a function of the average cell size, *d*, fitted with the power law form of $w \propto d^{1-2\chi}$. The diamonds show the testing data; the solid line is the regressed curve.

CHAPTER 6

DYNAMIC INDENTATION TESTS ON

CELLULAR SILICA

6.1. Introduction

According to the classic theory (Gibson and Ashby, 1982; Gibson and Ashby, 1997), the mass density of a cellular material, ρ, is proportional to (1-p), with p being the cell volume fraction; the strength, Y, the hardness, H, and the stiffness, E, are proportional to (1-p)$^\alpha$, where α is a system constant; all of them are independent of the cell size, d. In many applications, a low mass density is desirable and therefore, the cell volume fraction must be maximized (Bhattacharya et al., 2002; Minakuchi et al., 1996; Svec and Fréchet, 1992), which however leads to a low strength or hardness. While in some cases using weak cellular materials are acceptable. In general, the material must exhibit a sufficiently high strength; otherwise they cannot meet the increasingly high

requirements on structural integrity (Leventis et al., 2002). In fact, because $\rho \propto (1\text{-}p)$ and $H \propto (1\text{-}p)^{\alpha}$, very often the cell volume fraction has to be sacrificed to reach the required strength or hardness; these cellular materials are heavy and/or low-performance(Gibson and Ashby, 1982; Luo and Stevens, 1999).

Over the years, people were searching for solutions for lightweight and hard cellular materials, ideally harder than solids. Particularly, under the most critical loading conditions, i.e. when the cellular material is impacted, the classic relationship of $H \propto (1\text{-}p)^{\alpha}$ should be broken down. A number of beneficial size effects on the nanometer (nm) scale were investigated: carbon nanotubes (Treacy et al., 1996), copper nanopillars (Jennings et al., 2010), and nanowires (Wu et al., 2005). They have excellent strengths compared with bulk materials, thanks to the low defect density and the beneficial surface phenomena. However, they are small-sized. When they collectively form large cellular structures, e.g. carbon nanotube forests (Ren et al., 1998), the deformation mechanisms would change and the nm-scale strength may not be proportionally amplified. Nanoporous gold has demonstrated a higher strength than bulk gold (Hakamada and Mabuchi, 2007; Hodge et al., 2006), due to the hardening effect associated with the small ligament length; yet, this mechanism is most efficient when the network material is inherently soft and ductile. No conclusive results have been obtained for intrinsically hard monolithic cellular materials, e.g. cellular ceramics or glass.

6.2.   Preparation of Cellular and Solid Silica Samples

In the current study, we investigated nanocellular silica monoliths. The cells were created by using sol-gel methods (Miyamoto et al., 2013; Nakanishi, 1997; Shoup, 1976), and the cellular morphology was conditioned by a subcritical calcination (SCC) process, as described in Chapter 2. Solid silica disks were employed as reference samples. They were processed through a similar procedure while the firing was fully conducted to reach the density of 2.2 g/cm^3 (Brinker and Scherer, 1990). The processing conditions and key material parameters of cellular and solid silica samples were listed in Table 6.1. X-ray diffraction analysis confirmed that the solid samples had the same amorphous phase as the cellular silica, as shown in Figure 6.1. The testing samples were in disk form, with the diameter of 23-24 mm and the thickness of 4.50 mm. Figure 6.2 shows the morphology. The cell volume fraction of all the samples was maintained at ~60%; the cells were interconnected and of similar configurations; the average cell size ranged from ~50 nm to ~700 nm, with relatively narrow cell size distributions. The ligament length was nearly proportional to the cell size.

6.3.   Experimental Measurements

6.3.1. Quasi-static Indentation

Quasi-static indentation tests were conducted by compressing a tungsten carbide (TC) hemispherical indenter into the surface of cellular/solid silica disk, with the loading/unloading rate of 0.01 mm/min, as discussed in Chapter 3. The indenter was obtained from Bal-tec Company, with the diameter of 4.75 mm, the hardness of 91 HRA,

and the surface roughness of 0.7 micro inch Ra maximum. The peak loading was $F_{max} = 300$ N. The typical force-displacement curves are shown in Figure 6.3. For each type of silica, four samples were tested.

After the indenter was removed, the sample surface was characterized by a Keyence VHX-1000 Digital Microscope. Through its built-in function of "3D Image Stitching", the depth profiles of indentations were scanned, with the scanning range slightly broader than the difference between the highest and the lowest focusing points, and the scanning resolution of less than 2 μm per step. The depth profiles are shown in Figure 6.4. From the sample surface (Figure 6.5), the indentation radius, R, was measured, and the results were shown in Figure 6.6. For self-comparison purpose, effective quasi-static indentation resistance was defined as

$$H_0 = F_{max}/\pi R^2 \tag{6.1}$$

where F_{max} is the maximum loading. The results were shown in Figure 6.7.

6.3.2. Dynamic Indentation

The Split Hopkinson Bar (SHB) setup (Chapter 3) was employed to test the samples under a more critical, dynamic loading condition. A titanium (Ti) tube striker was projected by a gas chamber to impact a stainless steel incident bar. For all the tests the striker speed was maintained at ~8.5 m/s. As shown in Chapter 3, the incident bar compressed a TC hemispherical indenter into the silica disk sample. The silica sample was firmly supported by a stainless steel substrate, followed by the transmission bar. The diameter of the indenter was 4.75 mm. The diameters of the incident and the transmission

bars were the same, 12.7 mm. The loading mode was similar with that in the quasi-static indentation experiment, while the loading rate was much higher. The typical incident, reflected and transmitted stress wave profiles were shown in Figure 6.8. For each type of silica, 3-5 samples were tested.

After the impact test, the sample surface was observed by the Keyence VHX-1000 Digital Microscope. The dynamic indentation profile was scanned, with the scanning parameters same as those for the quasi-statically indented samples. The scanned profiles were shown in Figure 6.9. From the sample surface in Figure 6.10, the indentation size, R, was measured, and the results were shown in Figure 6.11. For self-comparison purpose, effective dynamic indentation resistance was defined as

$$H = P_{\text{IW}} A_0 / \pi R^2 \tag{6.2}$$

where A_0 is the cross-section area of the incident bar and P_{IW} is the average incident wave pressure, measured by a set of Vishay WK-13-250BF-10C strain gauges mounted on the incident bar. The results are given in Figure 6.12.

6.3.3. Dynamic Cell-Deformation Zone

After dynamic indentation, the lateral inner surfaces of selected silica samples were exposed by cleaving along their diameters, as shown in Figure 6.13 (a), and were observed under a FEI-XL30 environmental scanning electron microscope (SEM) at 20kV, with a spot size of 3.0. The SEM samples had been coated with iridium using an Emitech K575X sputter coater at 85 mA for 6 seconds prior to the observation. Areas

underneath and near the indentations were scanned, as shown in Figure 6.13 (b-d) and Table 6.2-4. Table 6.5 showed the morphology of dynamically indented solid silica.

6.4.   Cell Size Effect

From Figure 6.3 to Figure 6.6, it can be seen that under the quasi-static indentation loading, the responses of all the cellular silica samples are similar. No clear correlation can be identified between the indentation size, R, and the cell size, d. The indentation created in solid silica under the same loading is much smaller, which should be attributed to its much higher quasi-static indentation resistance. For all the cellular silica samples, regardless of the cell size, the indentation size, R, is around 650 μm. The indentation size of solid silica is nearly 250 μm, nearly 40% of that of cellular silica, as predicted by the conventional theory (Gibson and Ashby, 1997) for the cell volume fraction of ~60%. As shown in Figure 6.7, the effective quasi-static indentation resistance of solid silica is around 1.55 GPa, and that of cellular silica is nearly 200 MPa; the latter is about 13% of the former, approximately fitting with the classic relationship of

$$H_0 \propto (1 - p)^2 \tag{6.3}$$

As the loading rate increases, the behaviors of cellular silica samples significantly change. As shown in Figure 6.8 to Figure 6.11, cell size becomes an important factor. When the cell size is larger than 165 nm, the dynamic indentation size of the cellular silica is larger than that of solid silica, which somewhat agrees with the quasi-static testing result: With the large cell volume fraction, cellular silica tends to be softer than its solid counterpart. However, as the cell size is reduced to below 165 nm, the indentation

size rapidly decreases with d; the cellular silica of a smaller cell size tends to be harder. Eventually, when d is smaller than 105 nm, the dynamic indentation in cellular silica is smaller than that in solid silica sample, suggesting that the cellular silica is effectively harder. Figure 6.12 indicates that the effective indentation resistance of solid silica subjected to dynamic loading is around 1 GPa, lower than but comparable with the quasi-static value. For cellular silica samples, as the cell size decreases from 700 nm to 165 nm, the effective dynamic indentation resistance is increased while the change is within the data scatter. As the cell size changes from 145 nm to 50 nm, the value of H largely rises from ~0.9 MPa to ~1.4 GPa by more than 50%. Particularly, as the cell size is below ~80 nm, the effective dynamic indentation resistance of cellular silica is higher than that of solid silica.

This "counter-intuitive" cell size effect indicates that under the dynamic indentation loading and when the cell size is below 100 nm, the classic theory breaks down. In Figure 6.13 (b-d), the SEM images of lateral surfaces of dynamically indented cellular silica samples are analyzed. Underneath the indentation, the material is compacted and the cells are highly deformed. The local area where more than 50% of local cells are crashed, as shown in Table 6.2, is defined as the cell deformation zone (CDZ) and their boundaries are marked by the solid squares in Figure 6.13; in the far fields, the cells are perfect and are not influence by the indentation, as shown in Table 6.4, and the boundaries are shown by the hollow squares in Figure 6.13. In between the far field and the CDZ, there is a transition zone (TZ) where the cell deformation is relatively mild (Table 6.3). For all the cell sizes under investigation, the depth of CDZ is quite similar, around 1500 µm, regardless of the cell size. The CDZ width decreases with

the cell size, following the trend of indentation radius. A major difference between the larger cell size above 165 nm and the smaller cell size below 105 nm is associated with the TZ: When the cell size is relatively large, the volume of TZ is negligible compared with CDZ; when the cell size is relatively small, TZ becomes much broader. When the cell sizes are ~105 nm and ~50 nm, the depths and the widths of TZ are 350-450 μm and 200-350 μm, respectively. The existence of the transition zone implies that, as the indenter impacts the sample, the resistance to the motion of the indenter comes from not only the CDZ, but also the transition zone. For small cells, every moment when the indenter moves a little, it has to overcome the extra resistance provided by a much larger volume of material in the transition zone. Consequently, the indentation depth and size becomes smaller when the cell size is relatively small. The results of the effective dynamic indentation resistance measurement (Figure 6.12) and the SEM image analysis (Figure 6.13) agree with each other quite well. Compared with cellular silica, the dynamically indented solid silica, as shown in Table 6.5, shows typical hackle markings (Bradt and Tressler, 1994; Gash, 1971). Note that the structure of TZ is somewhat similar with the "cold" boundary layer observed in granular materials (Kostyukov, 1991; Kusubov et al., 1989; Nesterenko et al., 1994a); however, the mechanisms of dynamic deformation of cellular and granular materials are fundamentally different.

The loading mode of dynamic indentation is highly nonlinear, since the cells in CDZ are crashed and the material properties are permanently changed; and highly heterogeneous, since the impact front is non-uniform (Meyers, 1994; Nesterenko, 2001). When the cell size is relatively small, the presence of the transition zone and the associated increase in the resistance force lead to an effective local hardening

phenomenon. With a certain strain rate, the compaction of smaller cells is completed faster and more localized. Firstly, when the cell size is relatively small (e.g. much smaller than the characteristic length scale of the indentation front), the cell collapse would result in local condensation, instead of local deflection; as the compacted cells are harder than the initial cellular structure, the local resistance to indentation would rise. Secondly, as the area underneath the indentation is compacted, the material deformation tends to develop along the lateral directions that offer less resistance, so that the TZ becomes wider. The combination of these mechanisms of small cells results in a higher local indentation resistance, which leads to a smaller indentation size and depth.

6.5. Influence of Strain Rate

The cell size effect, as discussed previously, only works under dynamic conditions. When a cellular silica sample is subjected to quasi-static indentation, the indentation size and the effective indentation resistance are only dependent on its cell volume fraction, exhibiting little correlation with its cell size. However, when the same cellular silica sample is indented dynamically, the effective indentation resistance would increase with the reduction in cell size. For the silica sample with the cell volume fraction of ~60%, when the cell size is below ~100 nm, the effective indentation resistance could be higher than that of solid silica.

In order to further understand the role of the strain rate, we varied the impact rate of the striker. The parameters of the indenter, including the indenter material and the indenter size, were the same for all the tests. The cell volume fractions of all the tested

samples were ~60%. The cell size ranged from ~50 nm to ~275 nm. The impact rate of the striker spanned from ~4 m/s to ~10 m/s. The testing results were shown in Figure 6.14. Overall, for the silica samples with a similar cell size, the effective indentation resistance decreases with the increase in impact rate; for the silica samples with a similar impact rate, the effective indentation resistance increases with the reduction in cell size. When the impact rate is within the range of ~7 m/s to ~9 m/s, and when the cell size is within the range of ~50 nm to ~120 nm, there is a peak (yellow surrounded by orange marks in Figure 6.14) where the effective indentation resistance is higher than that of solid silica (~1 GPa). Noted that, the effective quasi-static indentation resistance shown in Figure 6.7 is ~200 MPa, while the minimum effective indentation resistance shown in Figure 6.14 is ~600 MPa, so for a specific cell size, there should be a maximum effective indentation resistance when the impact rate varies. As shown in the left-hand side of Figure 6.14, for the silica samples with a relatively small cell size, e.g. ~100 nm, the effective indentation resistance first increases, and then decreases with the increase in impact rate.

As discussed in Section 6.4, under a dynamic loading, the resistance offered by a small-cell-sized sample to the indenter comes from not only the cell deformation zone (CDZ), but also the transition zone (TZ). When the impact rate is relatively low, the TZ could provide high enough resistance to help stop the motion of the indenter. However, when the impact rate is relative high, the indenter might not be stopped until the kinetic energy is fully dissipated by cell deformation, resulting in the increase in indentation size and the decrease in effective indentation resistance.

In brief, the strain rate has a great influence on the cell size effect. Only when the strain rate is appropriate can the effective dynamic indentation resistance of cellular silica be higher than that of solid silica. The strain rate should be related with the formation of the local hardened layer.

6.6.   Influence of Cell Volume Fraction

As shown in Equation (6.3), the quasi-static indentation resistance of an open cellular material is a function of its cell volume fraction and independent of the cell size. With the increase of the cell volume fraction, the indentation resistance would decrease. In Chapter 5, it is shown that the cell volume fraction has a great influence under dynamic shear loading.

We processed a set of cellular silica samples through similar procedures as described in Chapter 2; however, the samples were fired at different temperatures slightly higher than the glass transition point to obtain different cell volume fractions, ranging from ~55% to ~65%. As discussed in Chapter 2, compared with the cell volume fraction, the cell size was much less sensitive to the calcination temperature. Thus, as the cell volume fraction varied, the cell sizes of the silica samples with the same initial component mass ratio remained similar. The average cell size was ~80 nm. The indenter diameter was 4.75 mm. The impact rate of the striker was ~8.5 m/s.

Figure 6.15 shows the effective indentation resistance of cellular silica samples with similar cell size but various cell volume fractions. Within the range of cell volume fraction from ~55% to 65%, with the increase in cell volume fraction, the effective

indentation resistance is almost a constant, ~1075 MPa, while theoretically the quasi-static indentation resistance at the cell volume fraction of 55% should be more than 50% higher than that of 65%. This unique phenomenon should be attributed to the cell size effect. Under the impact rate of ~8.5 m/s, with the cell size of ~80 nm, and within the investigated cell volume fraction range, compared with the cell volume fraction, the effective indentation resistance is much more sensitive to the cell size: (1) The cell volume fraction is in the appropriate range so that local hardening can take place, which has been demonstrated in Chapter 5; (2) the impact rate is in the appropriate range so that the local hardened layer could dissipate the impact force or energy into the transition zone, a much larger volume of material being involved in resisting the motion of the indenter.

6.7. Dimensional Analysis for Dynamic Indentation Resistance

The experimental data suggested that the effective dynamic indentation resistance, H, is dependent on the cell size (d) and the loading rate (v), and is also related to the effective quasi-static indentation resistance (H_0):

$$H = f(d, K, H_0) \tag{6.4}$$

where K is the impact energy and f is a certain function. According to the Π-theorem (Bridgman, 1922),

$$H/H_0 = f(H_0 d^3/K) \tag{6.5}$$

If f is taken as a power law and it is assumed that

$$K \propto v^2 \qquad (6.6)$$

We have

$$\widetilde{H} \propto \left(\frac{v^2}{d^3}\right)^{\beta} (1-p)^{2-2\beta} \qquad (6.7)$$

where

$$\widetilde{H} = H/H_{\text{sq}} \qquad (6.8)$$

where H_{sq} is the effective quasi-static indentation resistance of solid material, and $\beta = 0.10 \pm 0.01$ is a system parameter determined through data fitting in Figure 6.16.

Clearly, $\widetilde{H}$, which reflects the dynamic indentation resistance of cellular silica, is fundamentally different from $H_0 \propto (1-p)^2$, the quasi-static indentation resistance: Not only the influence of the cell volume fraction, p, is weaker by a power of 2β, but also a new factor of v^2/d^3 comes in. While as p rises $\widetilde{H}$ tends to decrease, if v is sufficiently high and d is sufficiently small, $\widetilde{H}$ can be larger than 1; i.e. $H > H_{\text{sq}}$ – Under this condition, a cellular material is effectively harder/stronger than a solid.

6.8.   Diagram of Cell Size Effect

The experimental results of dynamic indentation showed that: (1) When the cell volume fraction is ~60%, the impact rate of the striker is ~8.5 m/s, as the cell size is below ~100 nm, cellular silica is harder than solid silica; (2) When the cell volume fraction is ~60%, if the impact rate is within the range of ~7 m/s to ~9 m/s, and when the cell size is within the range of ~50 nm to ~120 nm, there is an optimum cell size that offers the highest effective dynamic indentation resistance, higher than that of solid silica;

(3) When the cell size is ~80 nm and the impact rate of the striker is ~8.5 m/s, as the cell volume fraction is within the range of ~55% to ~65%, the cellular silica samples have a similar effective dynamic indentation resistance, slightly higher than that of solid silica. In addition, it is reasonable to assume that (4) When the cell volume fraction approaches zero, regardless of the cell size and the impact rate, the behavior of cellular silica converges to that of solid silica; and (5) When the cell volume fraction is close to 100%, regardless of the cell size and the impact rate, the cellular silica offers little strength/hardness.

Based on these facts and assumptions, a diagram was drawn, as shown in Figure 6.17. The space is divided into three regions: solid-like material region, regular cellular material (RCM) region, and nano-cellular material (NCM) region. The boundary between the RCM and the NCM regions is determined by the critical points where the cellular silica is harder than solid silica. The NCM region exists only under dynamic loadings: the impact rate or the kinetic energy must be sufficiently high.

6.9.   Summary and Conclusion

Under a dynamic loading, a nano-cellular silica could be harder than solid silica, as the cell size is smaller than ~100 nm. If the loading is applied quasi-statically, the indentation resistance of the same nano-cellular silica fits well with the classic theory, having no relationship with the cell size. We attribute this dynamic size effect to the local hardening that happens when the cell size is sufficiently small and the cell deformation is sufficiently fast, and the formation of transition zone that offers additional resistance to

the motion of the indenter. The optimum cell size associated with the maximum effective dynamic indentation resistance is dependent on the strain rate. Upon a specific strain rate, the cellular silica samples with the cell size of ~80 nm and the cell volume fraction in the range of ~55% to ~ 65% have a similar dynamic indentation resistance, slightly higher than solid silica does. Dimensional analysis is carried out the capture the effects of cell size and strain rate; a new factor, v^2/d^3, comes in. A diagram of the cell size effect is developed to summarize the testing results.

Chapter 6, in part, has been submitted for publication in Nature, and co-authored by Yu Qiao; in part, is currently being prepared for submission for publication of the material, and co-authored by Yu Qiao. The dissertation author was the primary investigator and author of this work.

Table 6.1: Processing conditions and properties of cellular and solid silica samples.

Component mass ratio	TMOS to PEG				Colloidal silica to potassium silicate				
	4.8:1.0	5:95	10:90	15:85	18.5:81.5	25:75	30:70	40:60	25:75
SCC temperature (°C)	1210	1249	1254	1247	1236	1236	1229	1224	1250 (12h)
Average cell size (nm)	700±440	275±90	210±60	165±45	145±30	105±15	80±15	50±10	solid silica
Cell volume fraction (%)	59.7±1.0	60.7±1.2	59.9±0.6	59.8±1.2	60.6±1.1	61.4±1.4	60.5±0.5	60.5±0.5	<1.0
Thickness (mm)	4.52±0.01	4.54±0.01	4.53±0.01	4.54±0.01	4.53±0.01	4.54±0.01	4.53±0.01	4.54±0.01	4.54±0.01

Table 6.2: Cell structures in the cell deformation zone of dynamically indented cellular samples. The cell volume fraction is ~60%. The indenter diameter is 4.75 mm. The impact rate of striker is ~8.5 m/s.
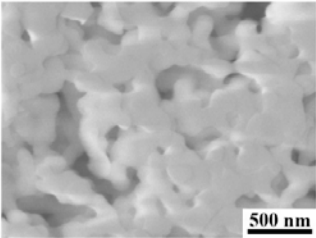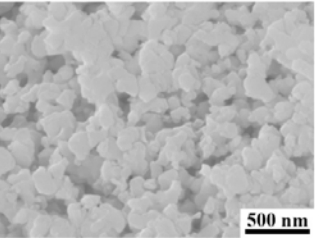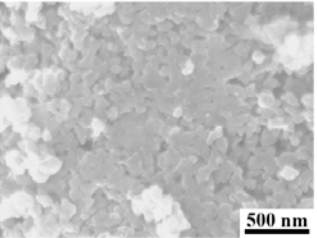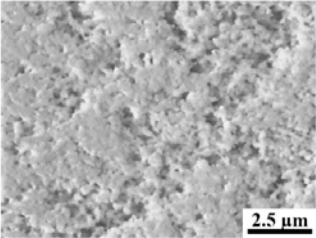
Magni-fication	Cell Size		
	275 nm	165 nm	105 nm
50000 X	500 nm	500 nm	500 nm
10000 X	2.5 μm	2.5 μm	2.5 μm
1000 X	25 μm	25 μm	25 μm
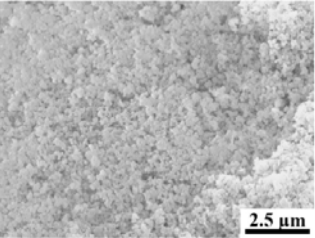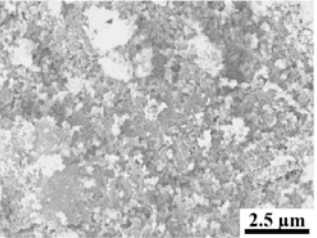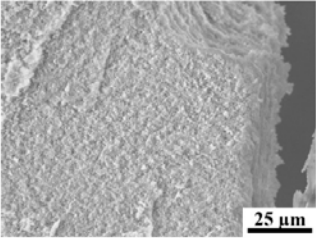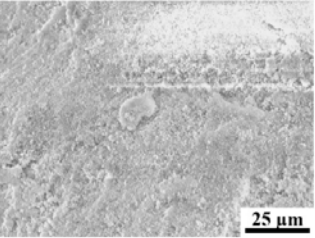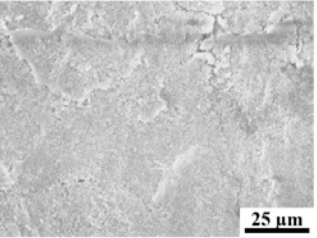
Table 6.3: Cell structures in the transition zone of dynamically indented cellular samples. The cell volume fraction is ~60%. The indenter diameter is 4.75 mm. The impact rate of striker is ~8.5 m/s.
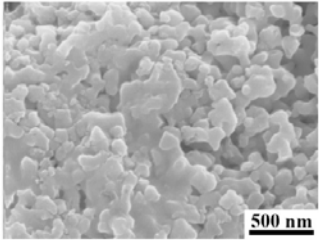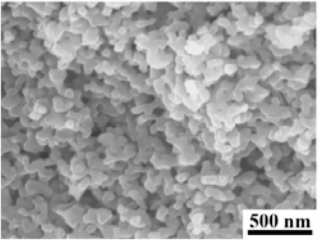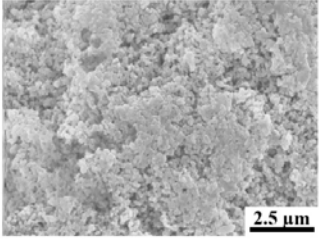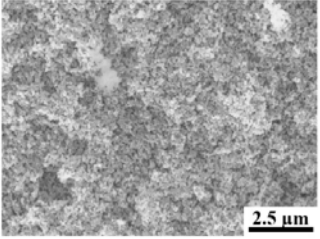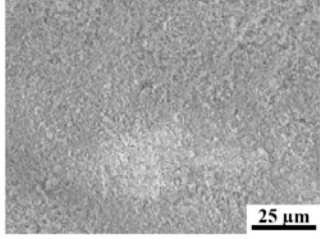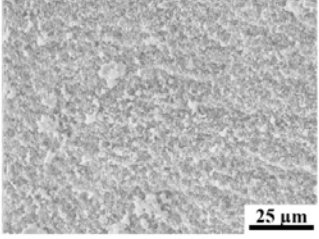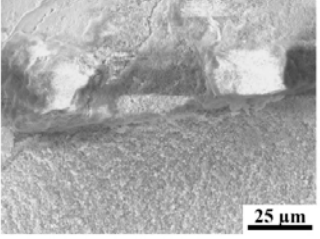
Magni-fication	Cell Size		
	275 nm	165 nm	105 nm
50000 X			
10000 X			
1000 X			

Table 6.4: Cell structures in the far field of dynamically indented cellular samples. The cell volume fraction is ~60%. The indenter diameter is 4.75 mm. The impact rate of striker is ~8.5 m/s.
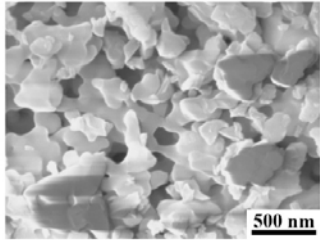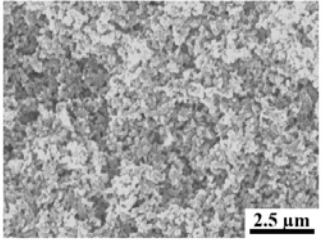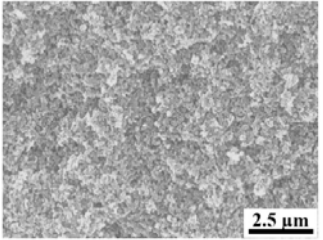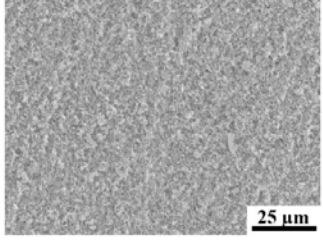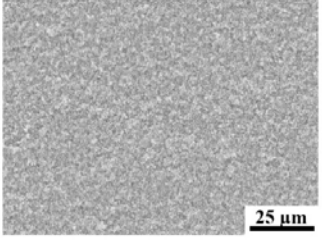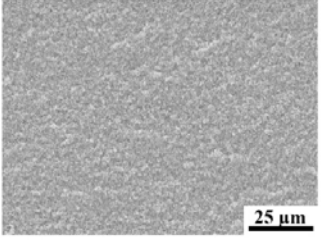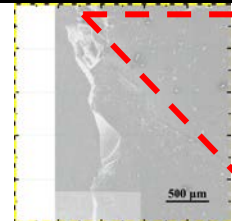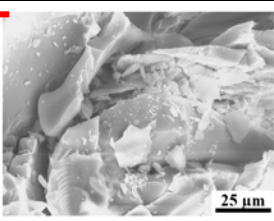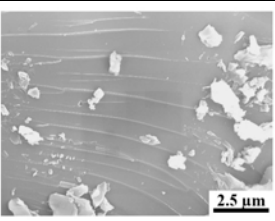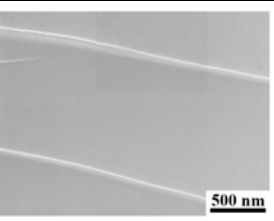
Magni-fication	Cell Size		
	275 nm	165 nm	105 nm
50000 X			
10000 X			
1000 X			

Table 6.5: Morphology of dynamically indented solid silica. The indenter diameter is 4.75 mm. The impact rate of striker is ~8.5 m/s.
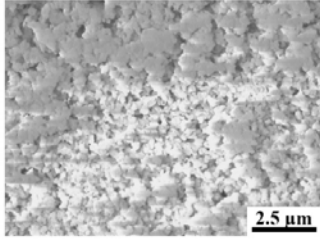
SEM Magnification			
50 X	1000 X	10000 X	50000 X

Figure 6.1: Typical x-ray diffraction curves of cellular and solid silica samples.
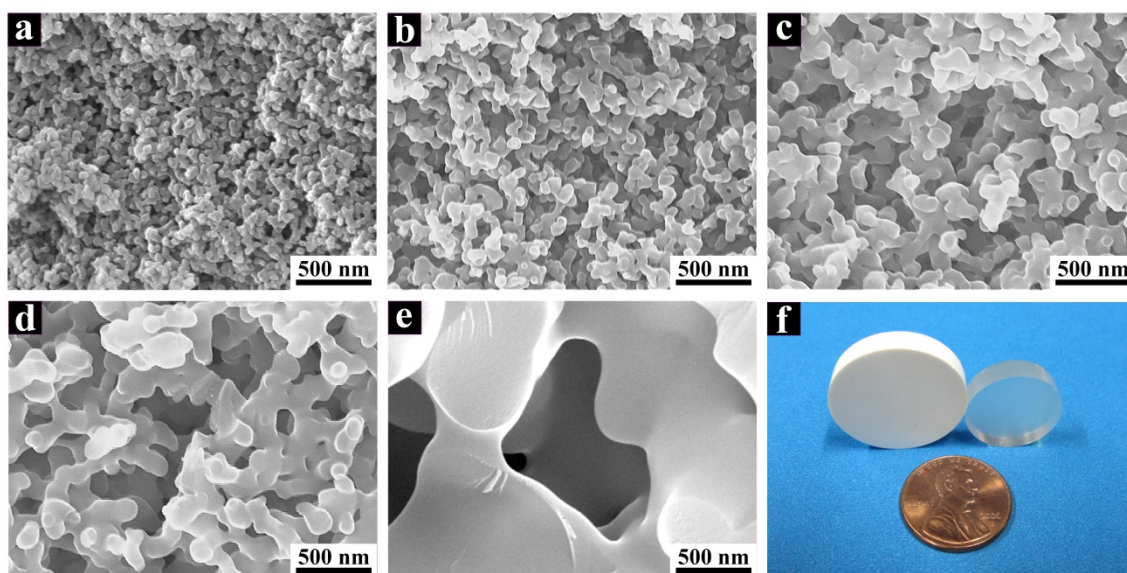
Figure 6.2: Cellular and solid silica samples. SEM images of cellular silica samples with the cell sizes of (a) 50 nm, (b) 105 nm, (c) 165 nm, (d) 275 nm, and (e) 700 nm, respectively. (f) Photo of cellular (left) and solid (right) silica samples. The cell volume fraction of cellular silica is ~60%. The cell volume fraction of solid silica is less than 1%.
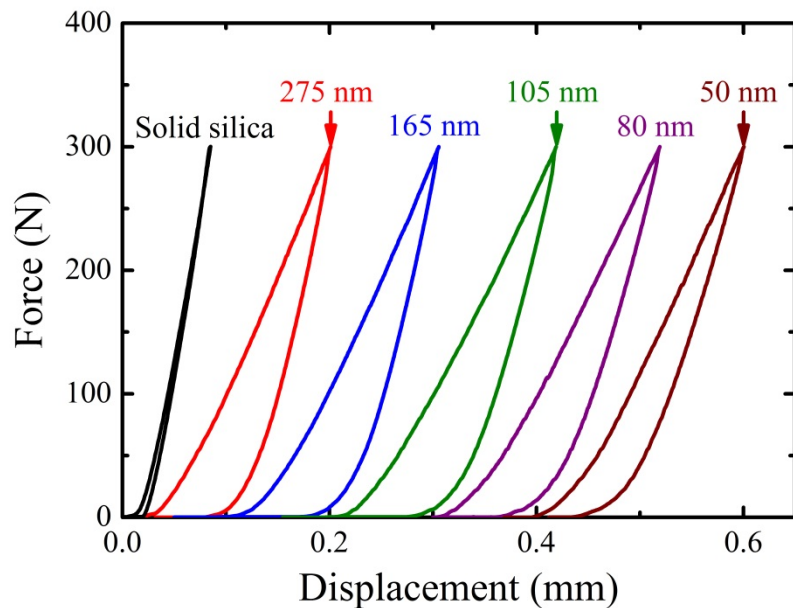
Figure 6.3: Typical quasi-static indentation curves. The loading/unloading rate is 0.01 mm/min. The indenter diameter is 4.75 mm. The cell volume fraction is ~60%. The curves have been shifted along the horizontal axis. The arrows indicate the average cell sizes.
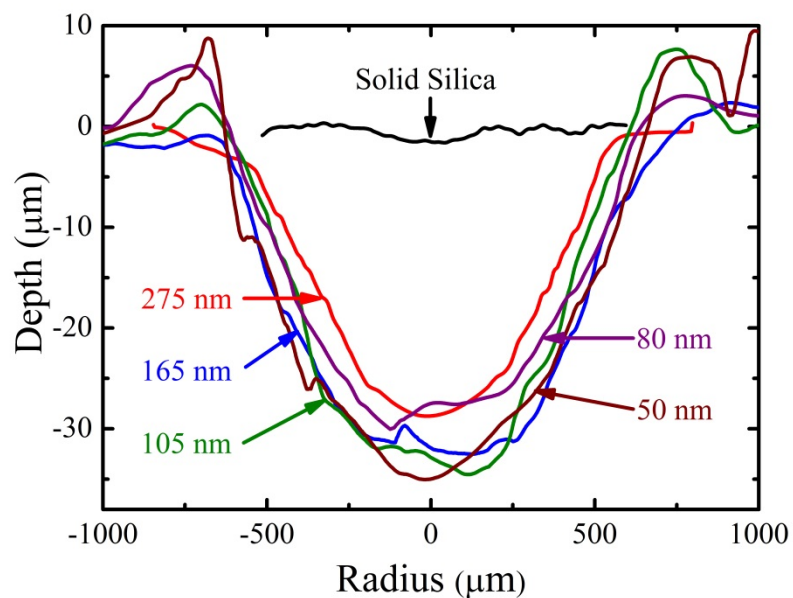
Figure 6.4: Typical quasi-static indentation profiles. The loading/unloading rate is 0.01 mm/min. The maximum loading is 300 N. The indenter diameter is 4.75 mm. The cell volume fraction is ~60%.
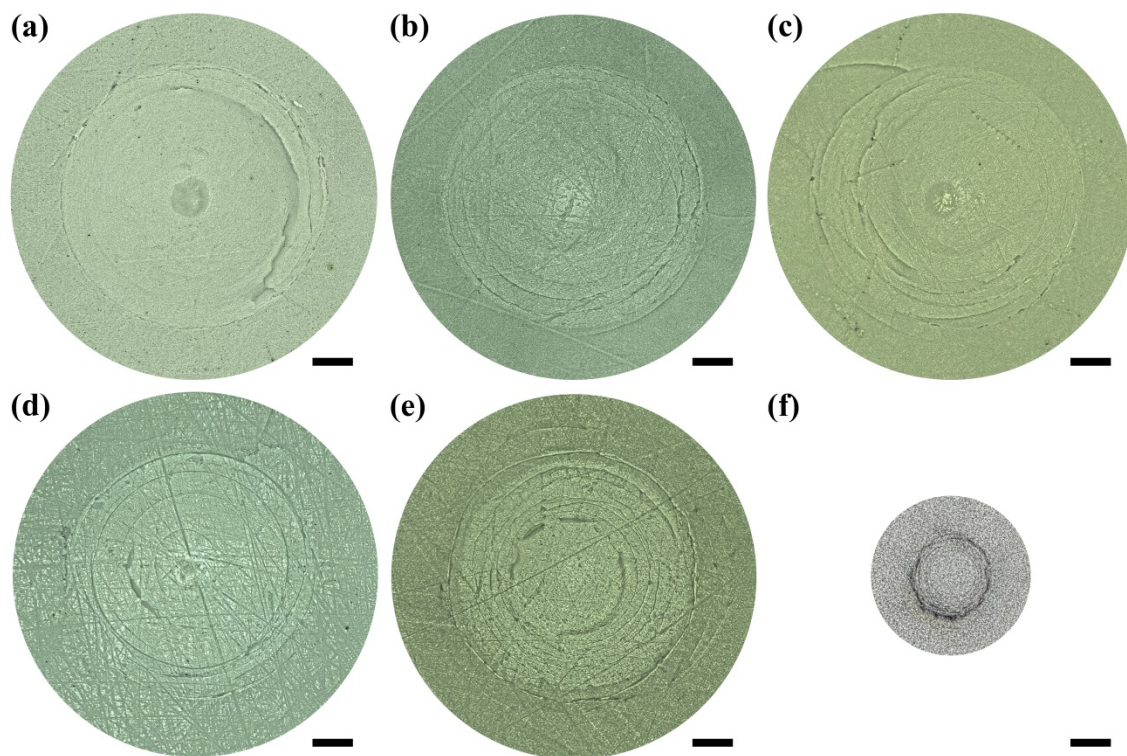
Figure 6.5: Photos of quasi-statically indented cellular silica samples, with the cell sizes of (a) 275 nm, (b) 165 nm, (c) 105 nm, (d) 80 nm, and (e) 50 nm, respectively; and (f) a quasi-statically indented solid silica sample. The loading/unloading rate is 0.01 mm/min. The maximum loading is 300 N. The indenter diameter is 4.75 mm. The cell volume fraction is ~60%. All the scale bars are 250 µm.
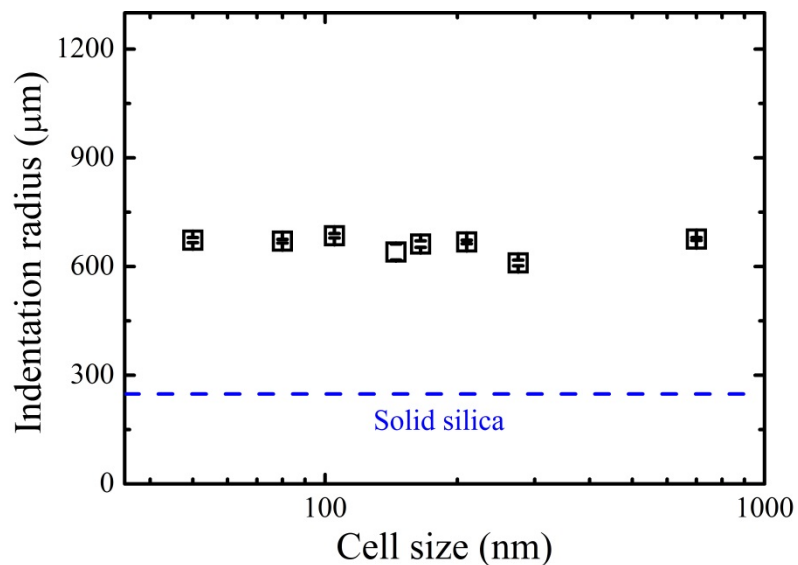
Figure 6.6: Quasi-static indentation radius as a function of the average cell size. The loading/unloading rate is 0.01 mm/min. The maximum loading is 300 N. The indenter diameter is 4.75 mm. The blue dash line shows the average indentation radius of solid silica samples, with the standard derivation less than 2 μm.
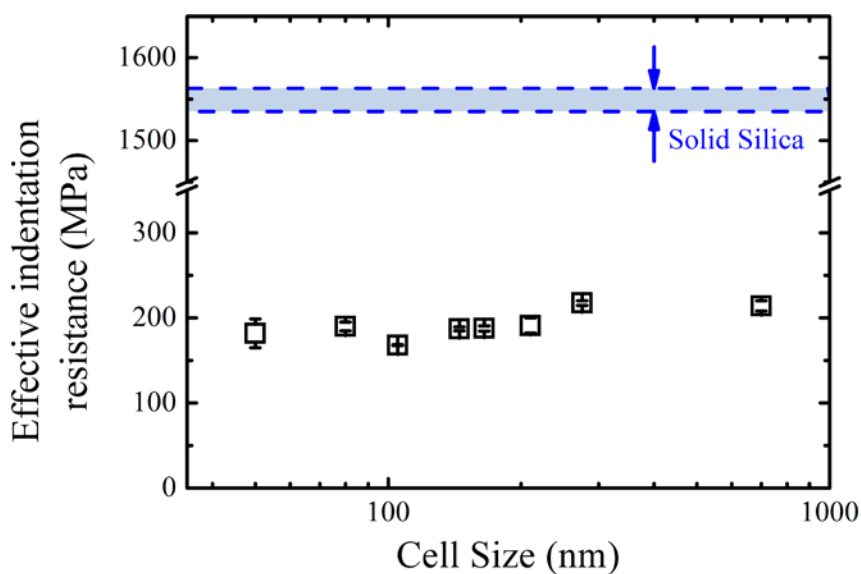
Figure 6.7: Effective quasi-static indentation resistance as a function of the average cell size. The loading/unloading rate is 0.01 mm/min. The maximum loading is 300 N. The indenter diameter is 4.75 mm. The cell volume fraction is ~60%. The blue bands in the blue dash lines mark the ranges of effective indentation resistance of solid silica.
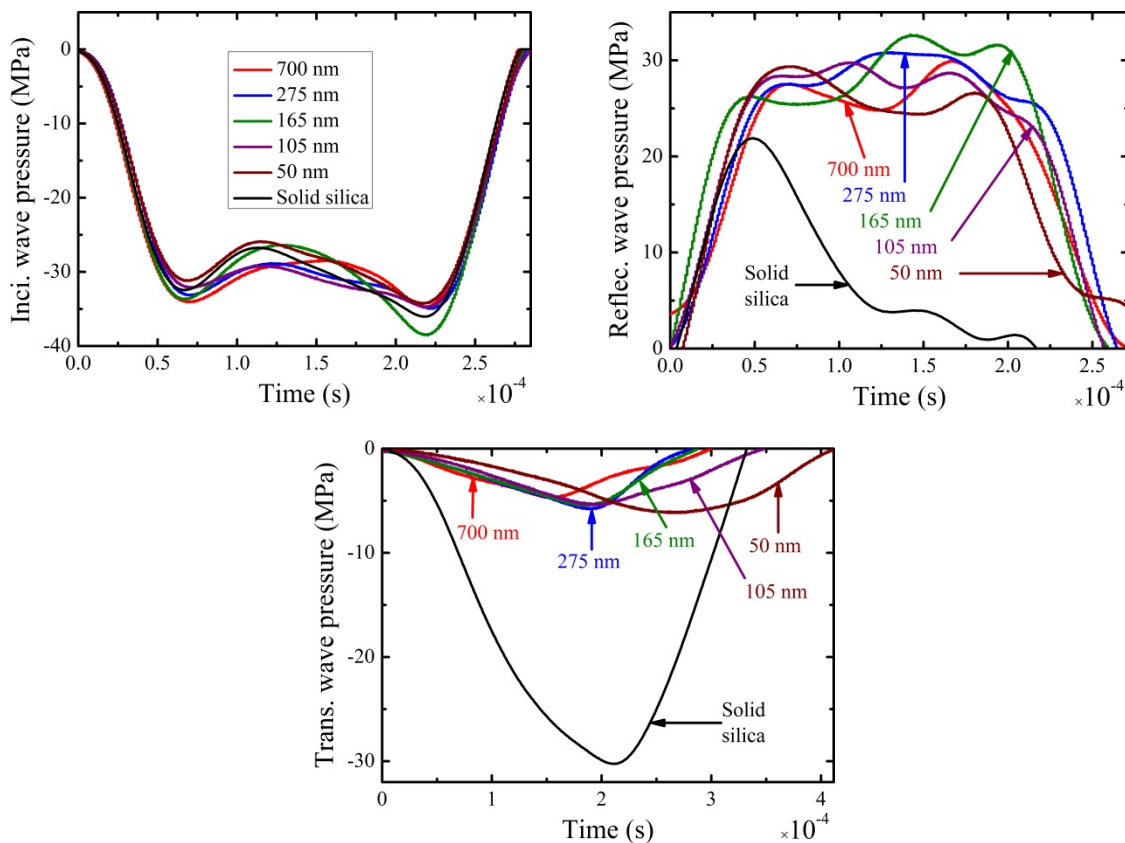
Figure 6.8: Typical incident (upper left), reflected (upper right) and transmitted (bottom) stress wave profiles in the dynamic indentation tests. The cell volume fraction is ~60%. The indenter diameter is 4.75 mm. The arrows indicate the cell sizes.
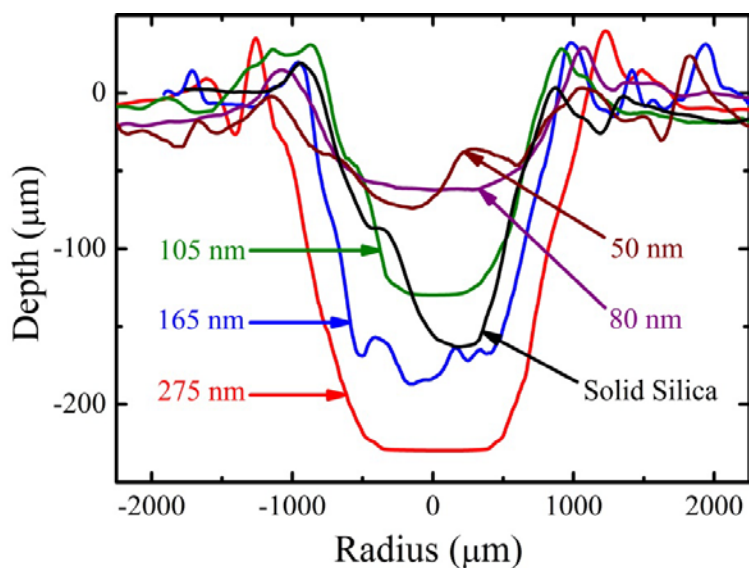
Figure 6.9: Typical dynamic indentation profiles. The cell volume fraction is ~60%. The indenter diameter is 4.75 mm. The impact rate of striker is ~8.5 m/s.
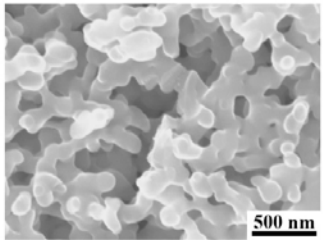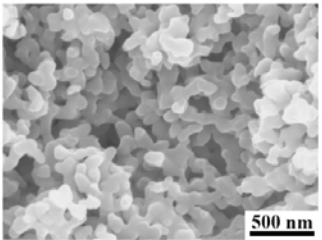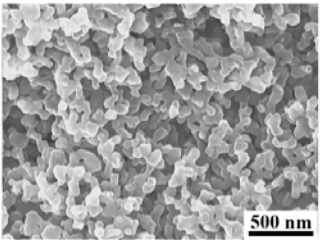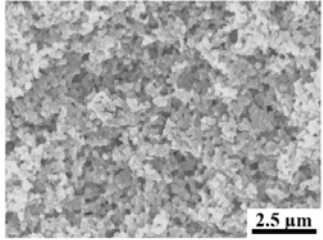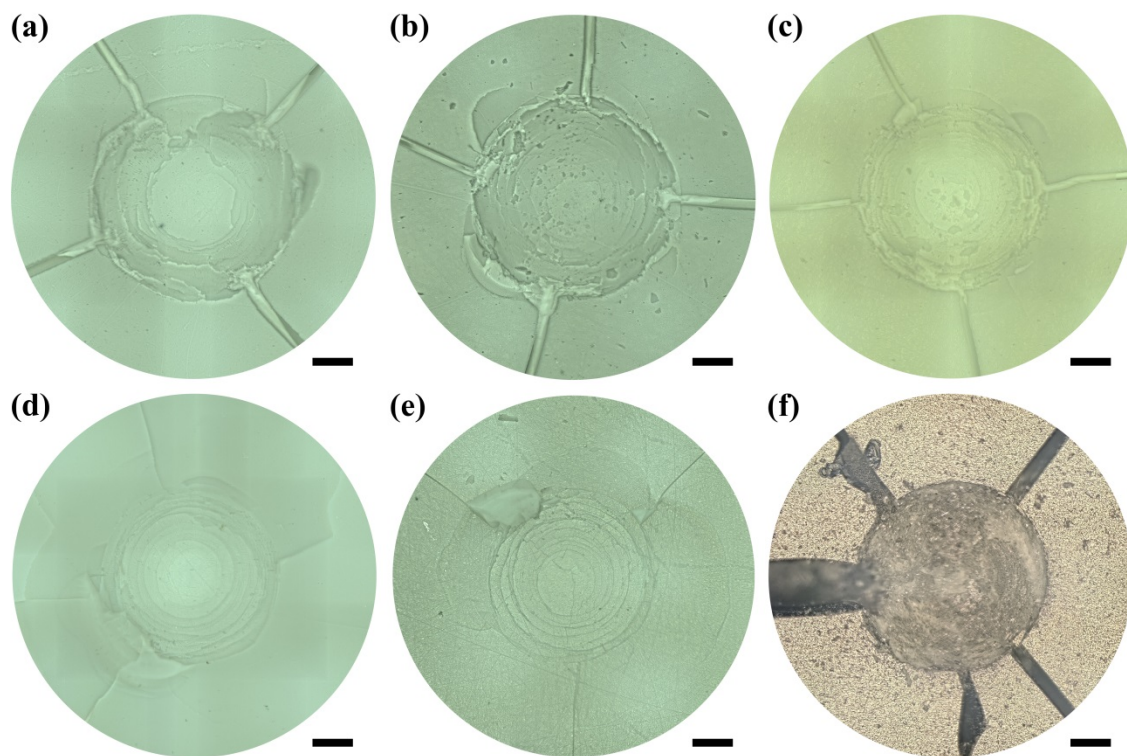
Figure 6.10: Photos of dynamically indented silica samples, with the cell sizes of (a) 275 nm, (b) 165 nm, (c) 105 nm, (d) 80 nm , and (e) 50nm, respectively; and (f) a solid silica sample. The cell volume fraction is ~60%. The indenter diameter is 4.75 mm. The impact rate of striker is ~8.5 m/s. All the scale bars are 500 µm.
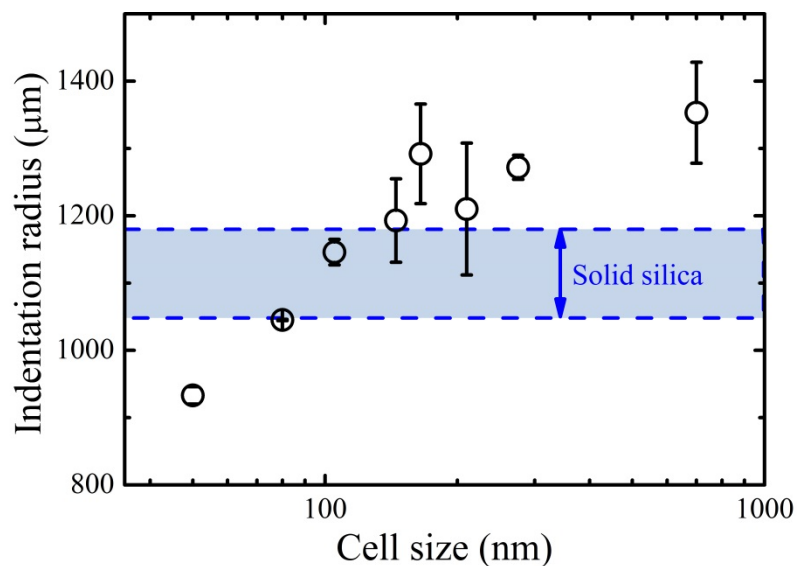
Figure 6.11: Dynamic indentation radius as a function of the average cell size. The cell volume fraction is ~60%. The indenter diameter is 4.75 mm. The impact rate of striker is ~8.5 m/s. The zone within the blue dash lines marks the range of indentation radius of solid silica.
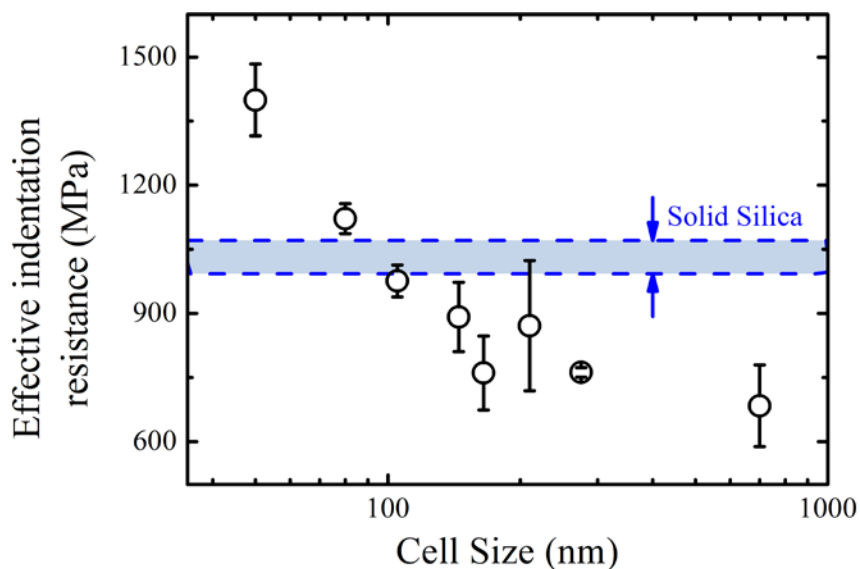
Figure 6.12: Effective dynamic indentation resistance as a function of the average cell size. The cell volume fraction is ~60%. The indenter diameter is 4.75 mm. The impact rate of striker is ~8.5 m/s. The blue bands in the blue dash lines mark the ranges of effective indentation resistance of solid silica.
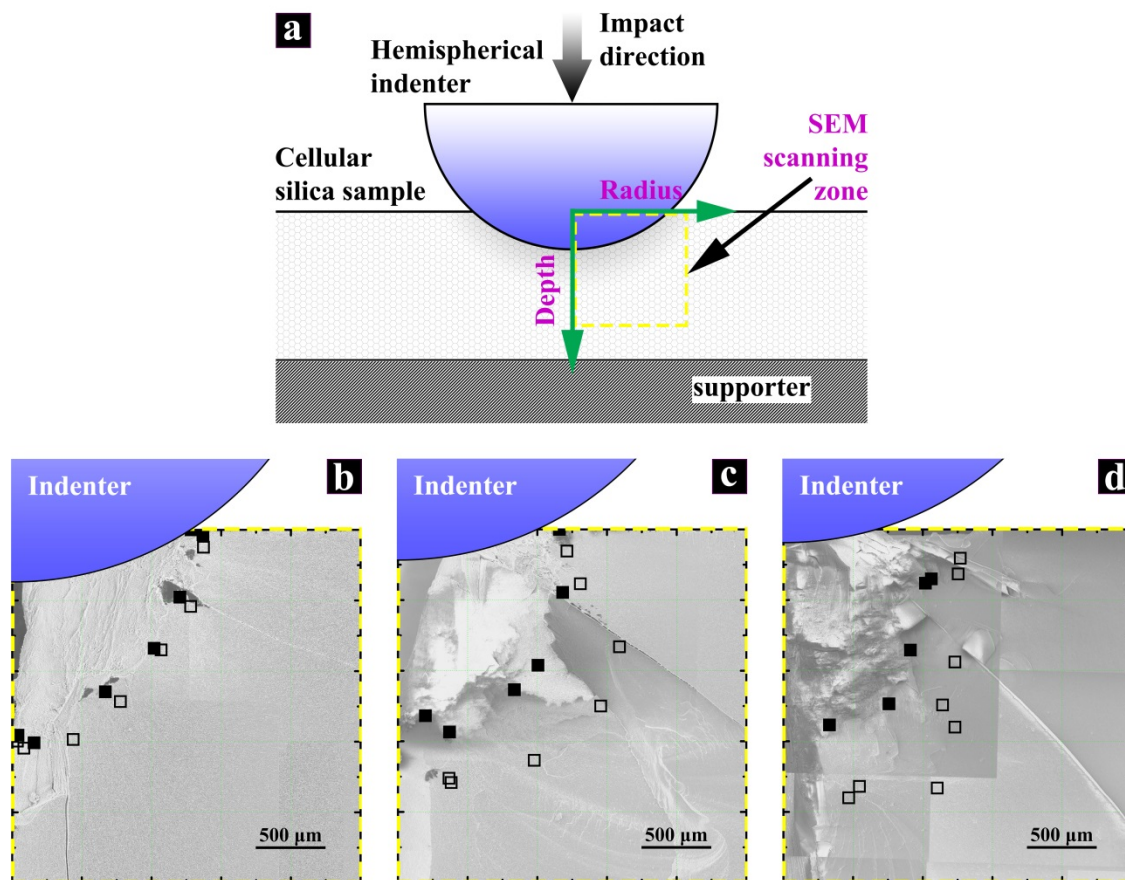
Figure 6.13: SEM images of dynamically indented cellular silica samples. (a) Schematic of the SEM scanning zone. SEM images of cellular silica samples with the cell sizes of (b) 275 nm, (c) 105 nm, and (d) 50 nm, respectively. The cell volume fraction is ~60%. The indenter diameter is 4.75 mm. The impact rate of striker is ~8.5 m/s. The positions of the indenter indicate the maximum indentation depths. The solid squares mark the boundaries of cell deformation zones (CDZ); the hollow squares mark the boundaries of transition zone (TZ).
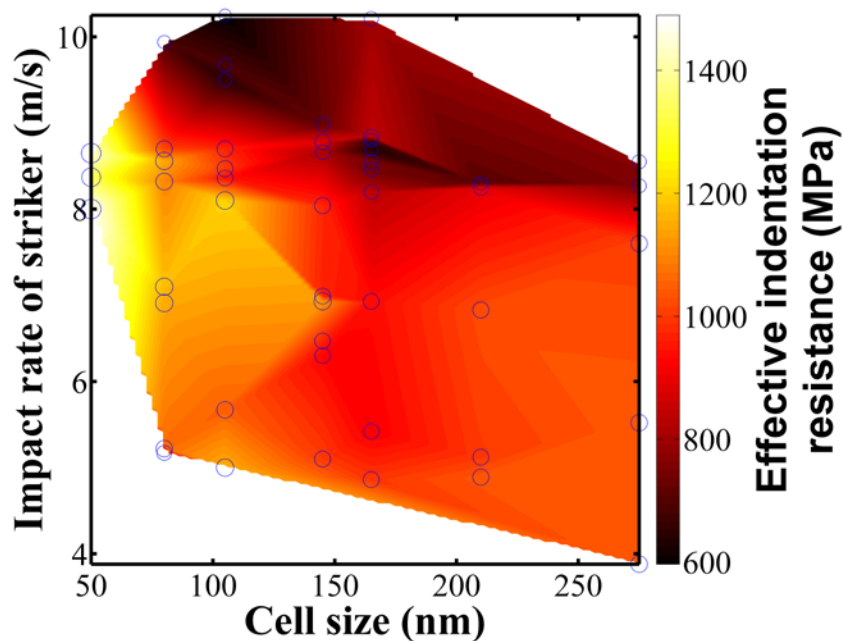
Figure 6.14: Effective indentation resistance of SCC-treated cellular silica under various impact rates of striker. The blue circles show the experimental data. The cell volume fraction is ~60%. The indenter diameter is 4.75 mm.
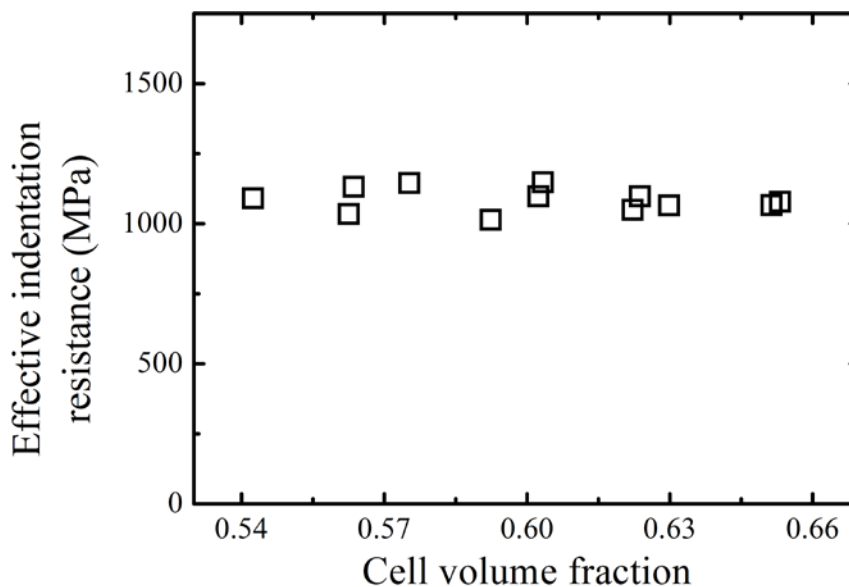
Figure 6.15: Effective indentation resistance of SCC-treated cellular silica with various cell volume fractions. The average cell size is ~80 nm; the impact rate of striker is ~8.5 m/s. The indenter diameter is 4.75 mm.
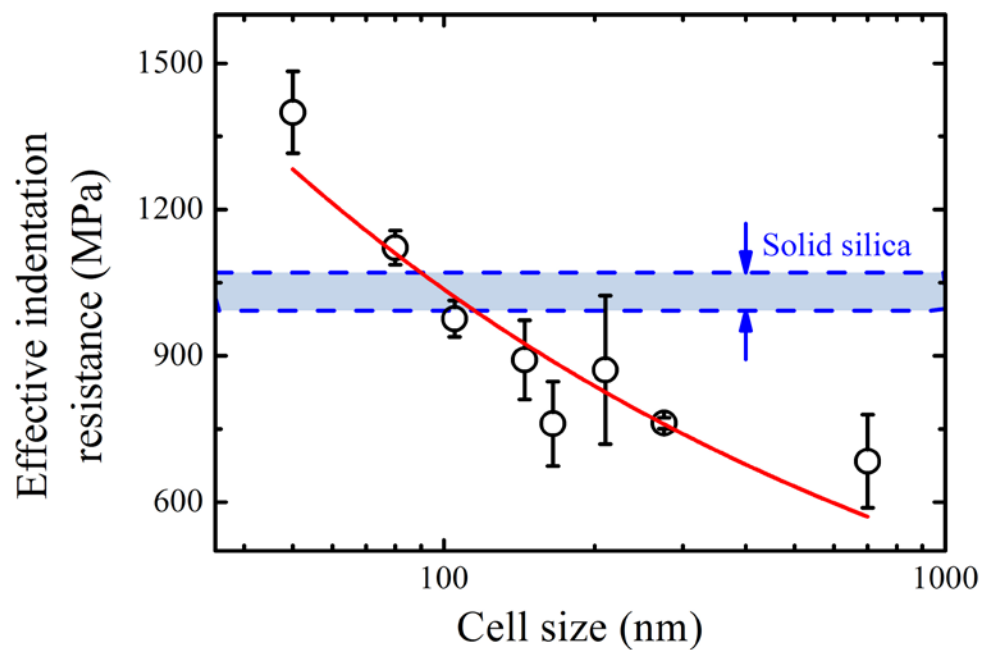
Figure 6.16: Effective dynamic indentation resistance as a function of the average cell size. The open circles show the experimental data. The red solid line is the regressed curve.
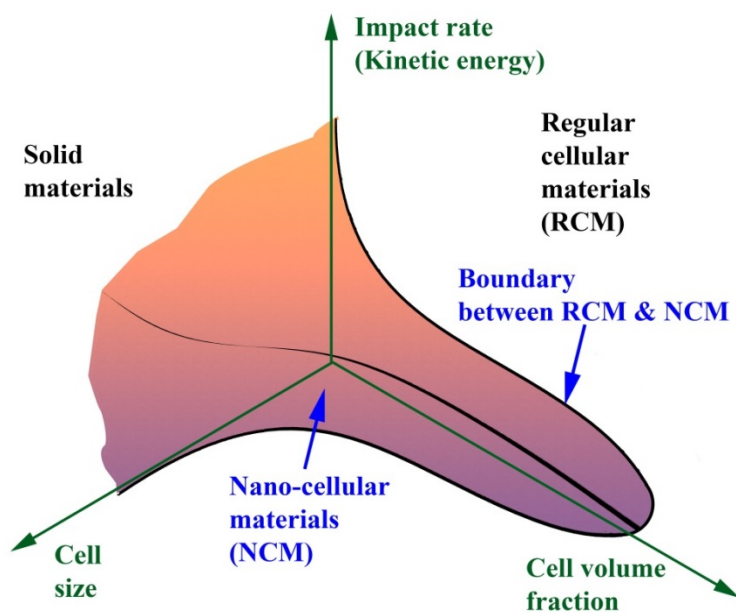
(a)
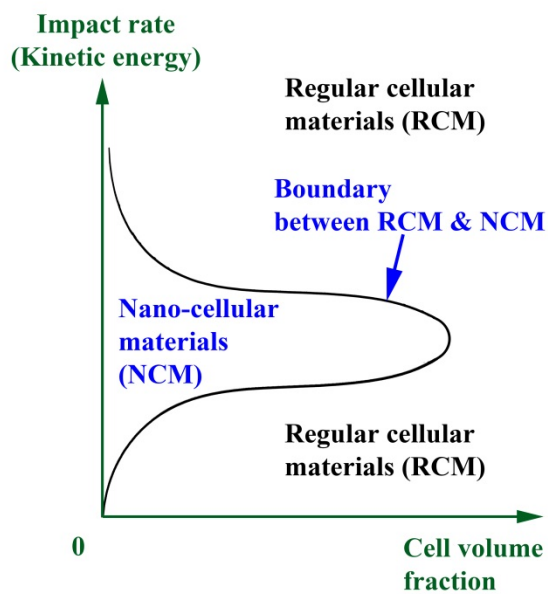
(b)

Figure 6.17: Diagram of dynamic indentation of cellular materials. The boundary between RCM and NCM is determined by the critical points where cellular silica becomes harder than solid silica.

CHAPTER 7

SUMMARY AND CONCLUSIONS

Through the current study, dynamic behaviors of cellular silica were experimentally investigated. The factors of cell size, cell volume fraction, strain rate, and loading mode were analyzed systematically. Under dynamic shearing, when the cell size is relatively small, the shear localization could be significantly suppressed. Under dynamic indentation, the effective indentation resistance of nano-cellular silica could be higher than that of solid silica.

These unique phenomena of nano-cellular silica could be attributed to the local hardening that happens when the cell size is sufficiently small and the cell deformation is sufficiently fast, and the formation of transition zone surrounding the local hardening area. The fast compaction of nano-cells caused by highly heterogeneous stress waves (e.g. in dynamic shearing) or highly non-uniform impact loading (e.g. in dynamic indentation) leads to the fast increase in local resistance. Consequently, bulk energy dissipation is

considerably promoted. Compared with dynamic indentation, dynamic shear loading is much more heterogeneous, since the cell deformation is concentrated in a thin layer near the intersection circle of the incident bar and the support ring. Dynamic indentation may be viewed as a mixed loading mode of dynamic shearing and compression.

Based on dimensional and theoretical analyses, two models were developed to describe the cell size effect on the deformation zone size in dynamic shearing and on the effective indentation resistance in dynamic indentation, respectively. They agree well with the experimental results. A diagram of cell size effect, accounting for the factors of cell size, cell volume fraction, and kinetic energy, was drawn to distinguish the nano-cellular materials from regular-cellular materials.

APPENDIX A

MECHANICAL DRAWINGS OF TESTING

APPARATUS

A.1   Shear Promotion Support Ring

As described in Section 3.2 in Chapter 3, the shear promotion support ring (SPSR) includes a front part, a rear part, and several mounting parts (e.g. cap screws, spring washers and hex nuts). Figure.A.1 and Figure.A.2 show the mechanical drawings of the front and the rear part, respectively.

A.2   Indentation System

The indentation system is similar as the SPSR, designed to reduce the potential bending during the testing. The difference lies in the rear part; for SPSR, there is a hole acting as the support ring; for indentation system, the rear part is solid, acting as the

support substrate. The spherical indenter is firmly attached to one end of a 17-4 PH stainless steel cylinder by VISHAY M-Bond 200 adhesive. The mechanical drawings of the front part, the rear part and the indenter were shown in Figure.A.3, Figure.A.4 and Figure.A.5, respectively.
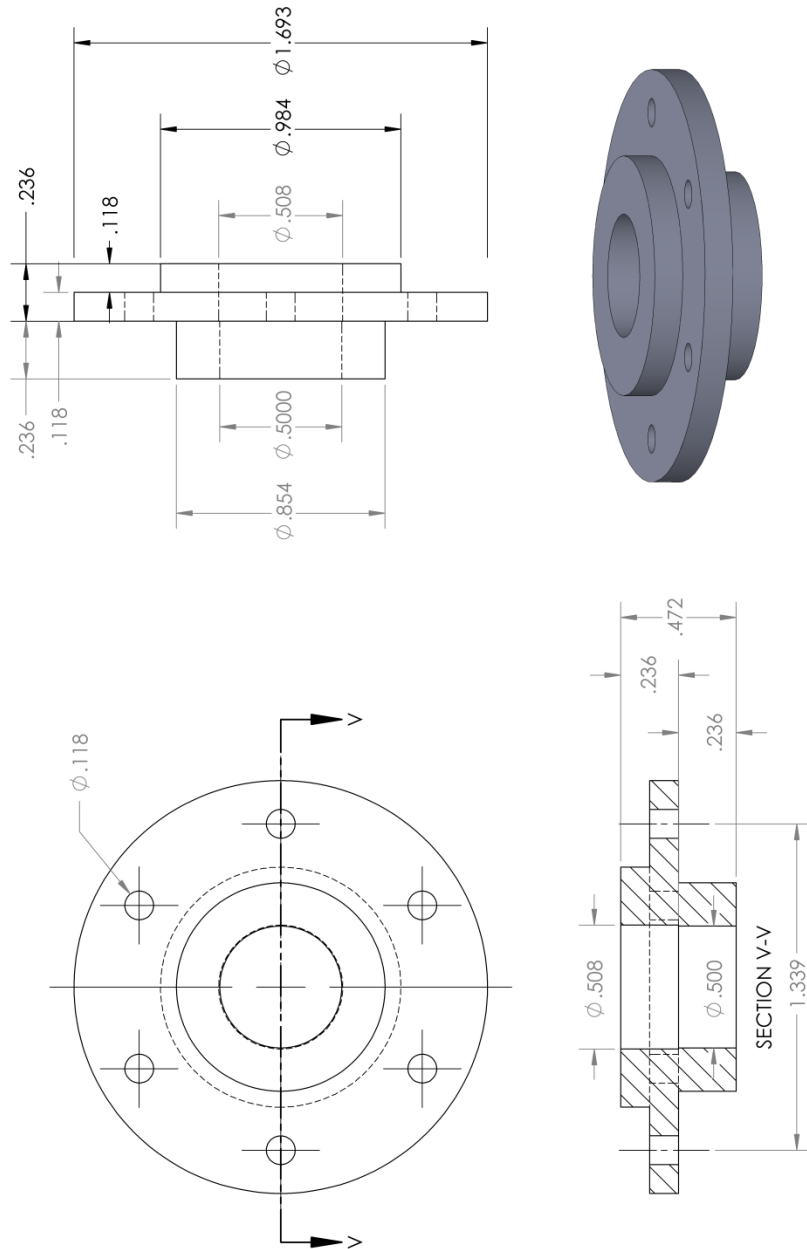
Figure A.1: Front part of shear promotion support ring.
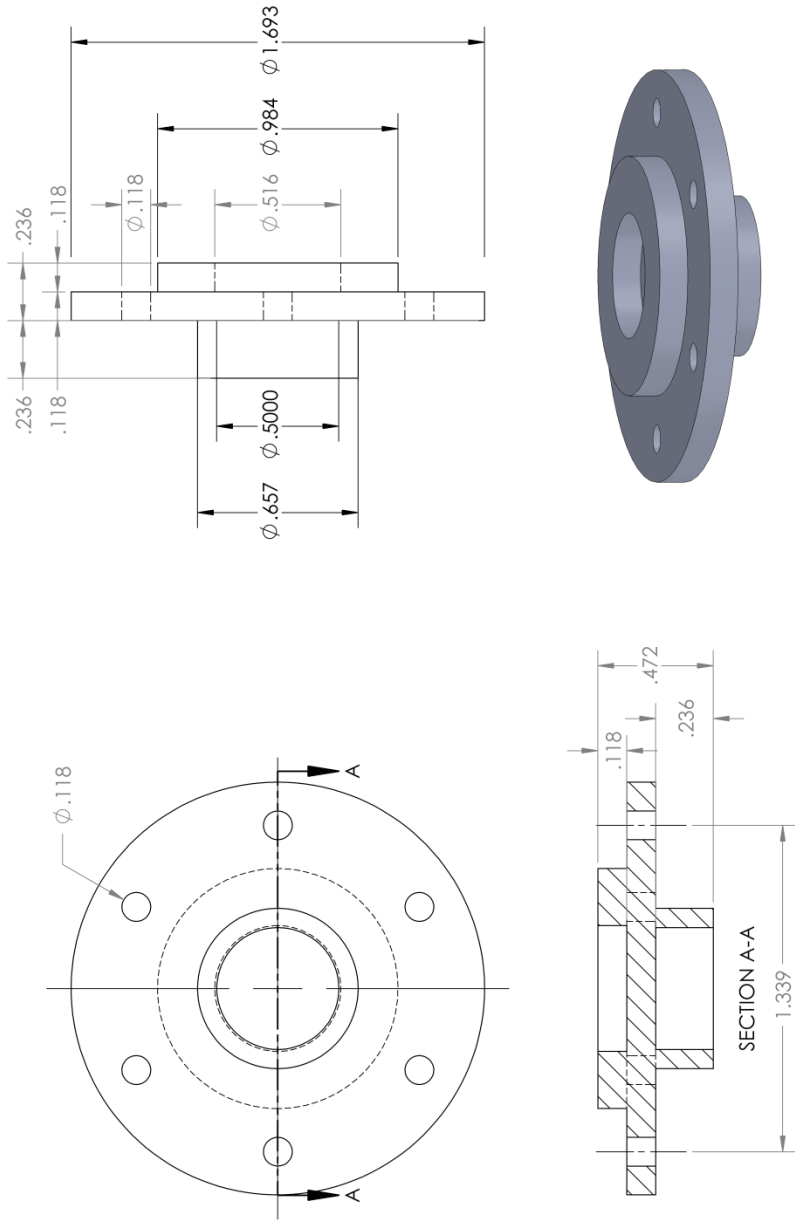
Figure A.2: Rear part of shear promotion support ring.
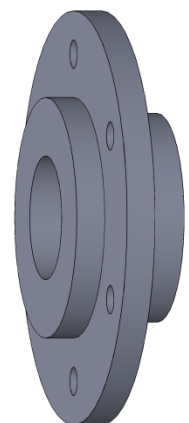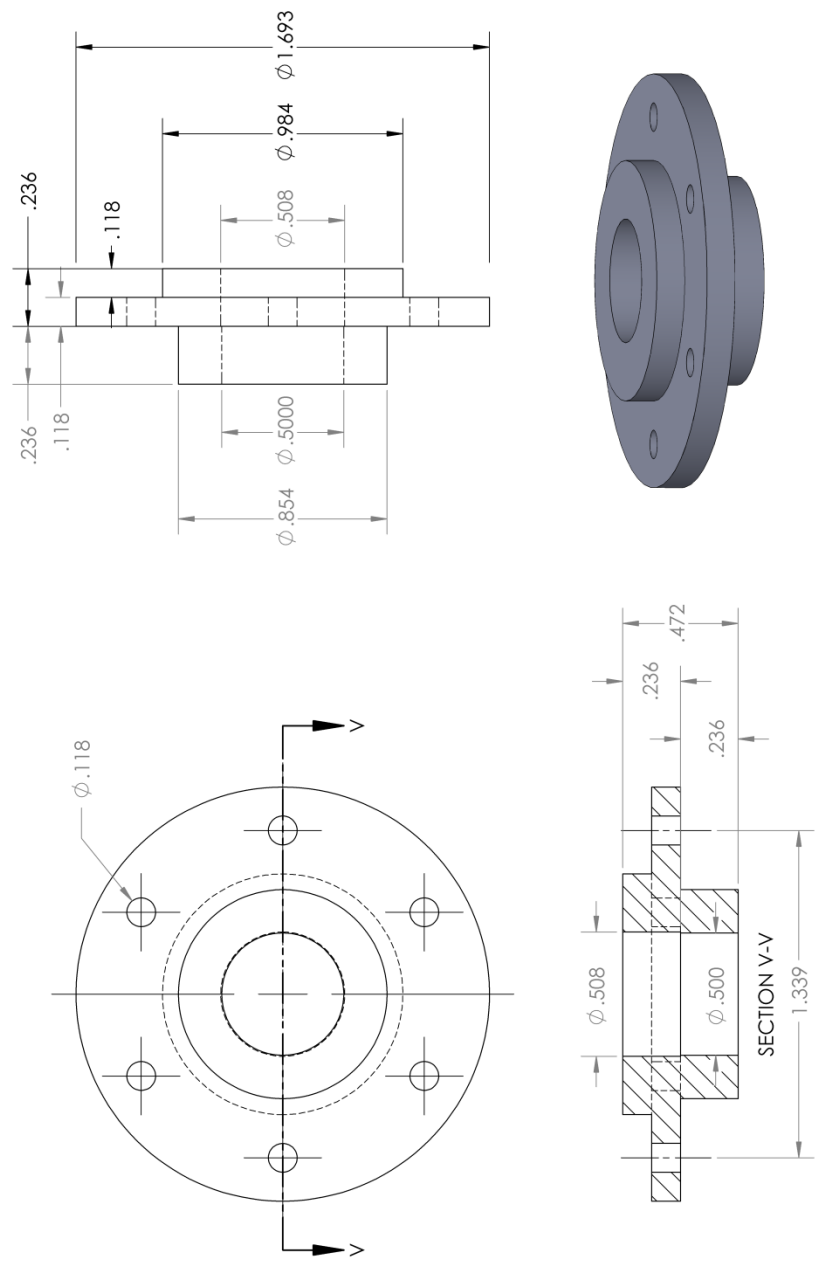
University of California, San Diego	Name	Indentation System	Material	17-4 PH Stainless Steel	Designer	Cang Zhao
Department of Structural Engineering	DWG#	IS-01	Unit	inch	Email	zcngu2011@gmail.com

Figure A.3: Front part of the indentation system.
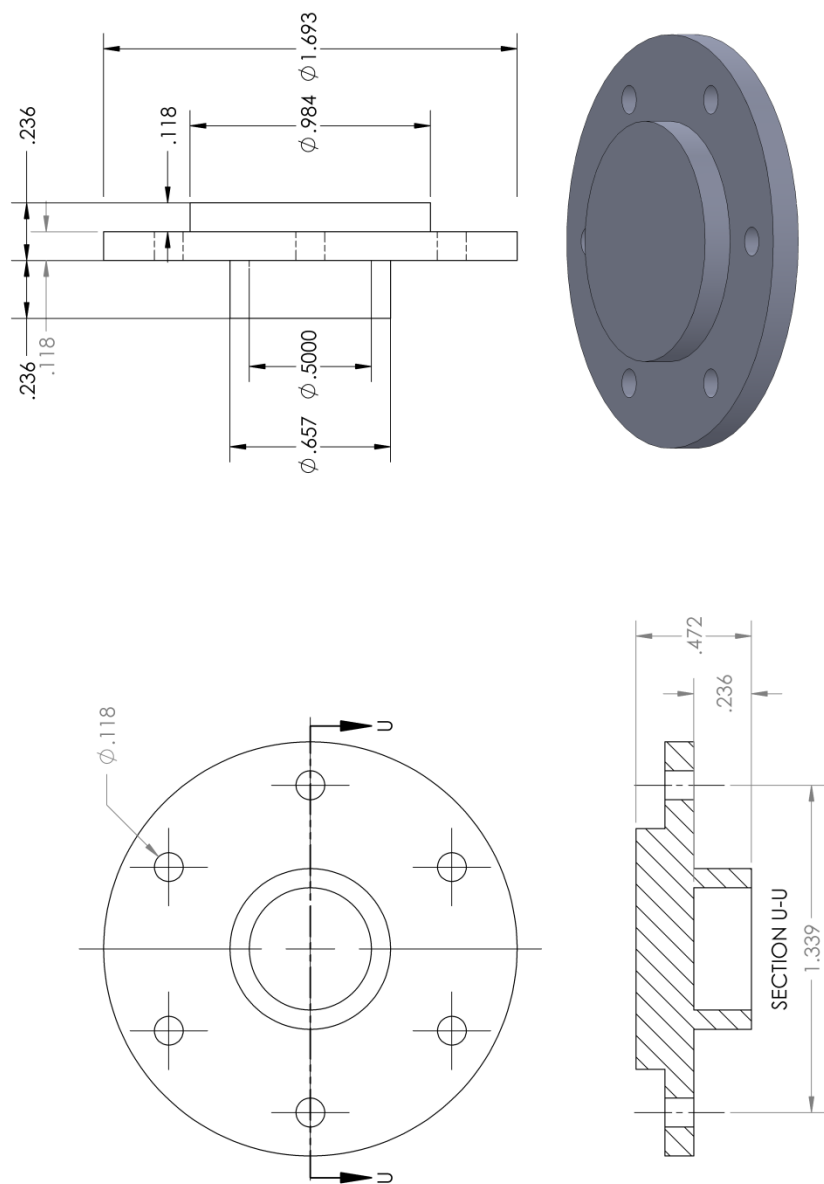
University of California, San Diego	Name	Indentation System	Material	17-4 PH Stainless Steel	Designer	Cang Zhao
Department of Structural Engineering	DWG#	IS-02	Unit	inch	Email	zcngu2011@gmail.com

SECTION U-U

Figure A.4: Rear part of the indentation system.
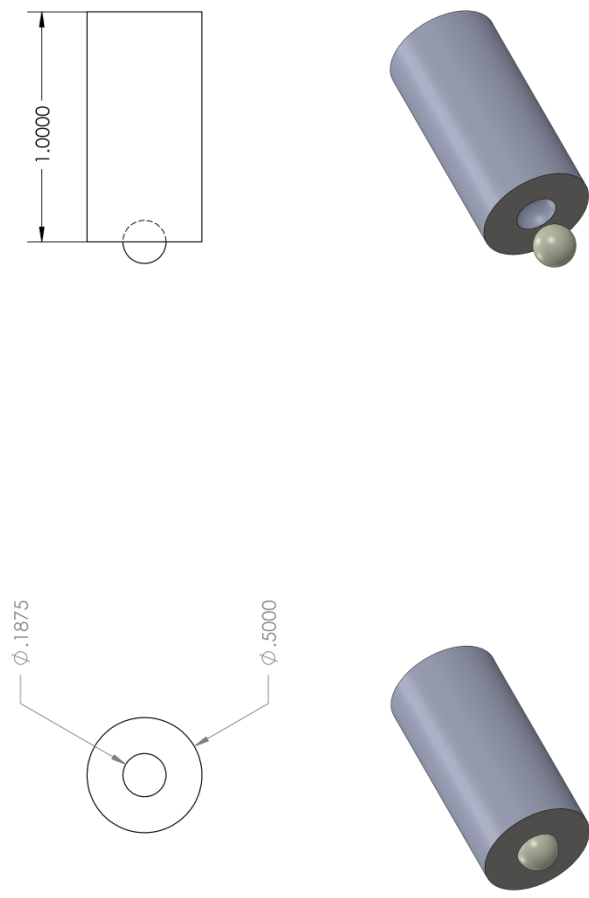
University of California, San Diego	Name	Indentation System	Material	Tungsten Carbide (Ball)	Designer	Cang Zhao
Department of Structural Engineering	DWG#	IS-03	Unit	inch	Email	zcngu2011@gmail.com

Figure A.5: Spherical indenter of the indentation system.

APPENDIX B

CODES FOR SEM IMAGE ENHANCEMENT

This appendix provides the main codes for the massive SEM image analysis through the software of Image-Pro Plus, described in Chapter 4. The input file has a format of "SilicaFoam12102013_#06-11-01_R01_01_01.tif", and the output file has a format of "SilicaFoam12102013_#06-11-01_R01_01_01_StdDev.tif".

```
Option Explicit

Sub SIECZ()

Dim i As Integer
Dim j As Integer
Dim k As Integer
Dim N As Integer

Dim Temp_Arr2 As String
Dim Temp_Path2 As String
```

```
Dim GrayImage As String
Dim OutputGrayImage As String
Dim fname(50) As String

For i = 1 To 50
        If i < 10 Then
                fname(i) = "0" & Str(i)
        ElseIf i <= 49 Then
                fname(i) = Str(i)
        Else
                fname(i) = "00"
        End If
Next i

For i = 1 To 50
        For j = 1 To 50
                For k = 1 To 10

                        GrayImage =
                        "C:\Users\zcngu\CalAP\Original\SilicaFoam12102013_#06-
                        11-01_R" & fname(i) & "_" & fname(j) & "_" & fname(k)
                        & ".tif"

                        OutputGrayImage =
                        "C:\Users\zcngu\CalAP\StdDev\SilicaFoam12102013_#06-
                        11-01_R" & fname(i) & "_" & fname(j) & "_" & fname(k)
                        & "_StdDev.tif"

                        GrayImage = Replace(GrayImage, " ", "")
                        OutputGrayImage = Replace(OutputGrayImage, " ", "")

                        If Dir(GrayImage) = "" Then
```

```
                    Else

                            ret = IpWsLoad(GrayImage,"TIF")
                            ret = IpAoiShow(FRAME_NONE)
                            ipRect.Left = 1
                            ipRect.top = 1
                            ipRect.Right = 645
                            ipRect.bottom = 482
                            ret = IpAoiCreateBox(ipRect)
                            ret = IpWsCopy()
                            ret = IpFltLocHistEq(60, 1, 6, 0.5)
                            ret = IpFltMedian(5, 2)
                            ret = IpFltGauss(5, 10, 1)
                            ret = IpFltClose(MORPHO_5x5OCTAGON, 2)
                            ret = IpFltShow(0)
                            ret = IpAoiShow(FRAME_NONE)
                            ret = IpWsSaveAs(OutputGrayImage, "tif")
                            ret = IpDocClose()

                    End If

            Next k
        Next j
Next i

End Sub
```

REFERENCES

Achenbach, J., 2012. Wave propagation in elastic solids. Elsevier.

Ajayan, P.M., Zhou, O.Z., 2001. Applications of carbon nanotubes, Carbon nanotubes. Springer, pp. 391-425.

Alshibli, K.A., Sture, S., 1999. Sand shear band thickness measurements by digital imaging techniques. Journal of computing in civil engineering 13, 103-109.

Andrade, U., Meyers, M.A., Vecchio, K.S., Chokshi, A.H., 1994. Dynamic recrystallization in high-strain, high-strain-rate plastic deformation of copper. Acta Metallurgica et Materialia 42, 3183-3195.

Argon, A., 1979. Plastic deformation in metallic glasses. Acta metallurgica 27, 47-58.

Asefa, T., Duncan, C.T., Sharma, K.K., 2009. Recent advances in nanostructured chemosensors and biosensors. Analyst 134, 1980-1990.

Ashley, C.E., Carnes, E.C., Phillips, G.K., Padilla, D., Durfee, P.N., Brown, P.A., Hanna, T.N., Liu, J., Phillips, B., Carter, M.B., Carroll, N.J., Jiang, X., Dunphy, D.R., Willman, C.L., Petsev, D.N., Evans, D.G., Parikh, A.N., Chackerian, B., Wharton, W., Peabody, D.S., Brinker, C.J., 2011. The targeted delivery of multicomponent cargos to cancer cells by nanoporous particle-supported lipid bilayers. Nat Mater 10, 389-397.

Bai, Y., 1981. A criterion for thermo-plastic shear instability, Shock Waves and High-Strain-Rate Phenomena in Metals. Springer, pp. 277-284.

Bai, Y., Xuc, Q., Xu, Y., Shen, L., 1994. Characteristics and microstructure in the evolution of shear localization in Ti-6A1-4V alloy. Mechanics of materials 17, 155-164.

Balch, D.K., O'Dwyer, J.G., Davis, G.R., Cady, C.M., Gray, G.T., Dunand, D.C., 2005. Plasticity and damage in aluminum syntactic foams deformed under dynamic and quasi-static conditions. Materials Science and Engineering: A 391, 408-417.

Bardet, J., Proubet, J., 1992. Shear-band analysis in idealized granular material. Journal of Engineering mechanics 118, 397-415.

Barton, T.J., Bull, L.M., Klemperer, W.G., Loy, D.A., McEnaney, B., Misono, M., Monson, P.A., Pez, G., Scherer, G.W., Vartuli, J.C., Yaghi, O.M., 1999. Tailored Porous Materials. Chemistry of Materials 11, 2633-2656.

Bhattacharya, A., Calmidi, V.V., Mahajan, R.L., 2002. Thermophysical properties of high porosity metal foams. International Journal of Heat and Mass Transfer 45, 1017-1031.

Bradt, R.C., Tressler, R.E., 1994. Fractography of glass. Springer.

Bridgman, P.W., 1922. Dimensional analysis. Yale University Press.

Brinker, C.J., Scherer, G.W., 1990. Sol-gel science: the physics and chemistry of sol-gel processing. Gulf Professional Publishing.

Carretero-González, R., Khatri, D., Porter, M.A., Kevrekidis, P., Daraio, C., 2009. Dissipative solitary waves in granular crystals. Physical review letters 102, 024102.

Chambers, S.D., Holcombe, T.W., Svec, F., Fréchet, J.M.J., 2011a. Porous Polymer Monoliths Functionalized through Copolymerization of a C_{60} Fullerene-Containing Methacrylate Monomer for Highly Efficient Separations of Small Molecules. Analytical Chemistry 83, 9478-9484.

Chambers, S.D., Svec, F., Fréchet, J.M.J., 2011b. Incorporation of carbon nanotubes in porous polymer monolithic capillary columns to enhance the chromatographic separation of small molecules. Journal of Chromatography A 1218, 2546-2552.

Chen, W.W., Song, B., 2010. Split Hopkinson (Kolsky) bar: design, testing and applications. Springer Science & Business Media.

Cheng, I.C., Hodge, A.M., 2013. Strength scale behavior of nanoporous Ag, Pd and Cu foams. Scripta Materialia 69, 295-298.

Clifton, R., 1983. Dynamic plasticity. Journal of Applied Mechanics 50, 941-952.

Clifton, R.J., 1974. III - Plastic Waves: Theory and Experiment, in: Nemat-Nasser, S. (Ed.), Mechanics Today. Pergamon, pp. 102-167.

Culver, R.S., 1973. Thermal instability strain in dynamic plastic deformation, Metallurgical effects at high strain rates. Springer, pp. 519-530.

Dannemann, K.A., Lankford, J., 2000. High strain rate compression of closed-cell aluminium foams. Materials Science and Engineering: A 293, 157-164.

Danquah, M.K., Forde, G.M., 2008. Large-volume methacrylate monolith for plasmid purification: Process engineering approach to synthesis and application. Journal of Chromatography A 1188, 227-233.

Daraio, C., Nesterenko, V., Herbold, E., Jin, S., 2005. Strongly nonlinear waves in a chain of Teflon beads. Physical Review E 72, 016603.

Daraio, C., Nesterenko, V.F., Herbold, E.B., Jin, S., 2006. Energy Trapping and Shock Disintegration in a Composite Granular Medium. Physical Review Letters 96, 058002.

Dario Arrua, R., Nordborg, A., Haddad, P.R., Hilder, E.F., 2013. Monolithic cryopolymers with embedded nanoparticles. I. Capillary liquid chromatography of proteins using neutral embedded nanoparticles. Journal of Chromatography A 1273, 26-33.

Dauchot, O., Marty, G., Biroli, G., 2005. Dynamical Heterogeneity Close to the Jamming Transition in a Sheared Granular Material. Physical Review Letters 95, 265701.

Davison, L., Graham, R.A., 1979. Shock compression of solids. Physics Reports 55, 255-379.

Deshpande, V.S., Fleck, N.A., 2000. High strain rate compressive behaviour of aluminium alloy foams. International Journal of Impact Engineering 24, 277-298.

Diao, Y., Harada, T., Myerson, A.S., Alan Hatton, T., Trout, B.L., 2011. The role of nanopore shape in surface-induced crystallization. Nat Mater 10, 867-871.

Dodd, B., 1992. Adiabatic shear localization: occurrence, theories, and applications. Pergamon Press.

Dodd, B., Bai, Y., 1989. Width of adiabatic shear bands formed under combined stresses. Materials science and technology 5, 557-559.

Dodd, B., Bai, Y., 2012. Adiabatic shear localization: frontiers and advances. Elsevier.

Donovan, P., Stobbs, W., 1981. The structure of shear bands in metallic glasses. Acta Metallurgica 29, 1419-1436.

Du, J., Kang, D.J., 2008. A template-free and green route to synthesize macroporous silver monoliths and their catalytic properties. Materials Letters 62, 3185-3188.

Elmer, T.H., 1991. Porous and reconstructed glasses. ASM International, Engineered Materials Handbook. 4, 427-432.

Falk, M., Langer, J., 1998. Dynamics of viscoplastic deformation in amorphous solids. Physical Review E 57, 7192.

Fang, Y., Tolley, H.D., Lee, M.L., 2010. Simple capillary flow porometer for characterization of capillary columns containing packed and monolithic beds. Journal of Chromatography A 1217, 6405-6412.

Field, J., Walley, S., Proud, W., Goldrein, H., Siviour, C., 2004. Review of experimental techniques for high rate deformation and shock studies. International Journal of Impact Engineering 30, 725-775.

Fressengeas, C., Molinari, A., 1987. Instability and localization of plastic flow in shear at high strain rates. Journal of the Mechanics and Physics of Solids 35, 185-211.

Gash, P.J.S., 1971. A study of surface features relating to brittle and semibrittle fracture. Tectonophysics 12, 349-391.

Gibson, L.J., Ashby, M.F., 1982. The Mechanics of Three-Dimensional Cellular Materials.

Gibson, L.J., Ashby, M.F., 1997. Cellular solids: structure and properties. Cambridge university press.

Gibson, L.J., Ashby, M.F., 1999. Cellular solids: structure and properties. Cambridge university press.

Grady, D., 1982. Local inertial effects in dynamic fragmentation. Journal of Applied Physics 53, 322-325.

Grady, D., 1992. Properties of an adiabatic shear-band process zone. Journal of the Mechanics and Physics of Solids 40, 1197-1215.

Grady, D., 1994. Dissipation in adiabatic shear bands. Mechanics of materials 17, 289-293.

Grady, D., Kipp, M., 1987. The growth of unstable thermoplastic shear with application to steady-wave shock compression in solids∗. Journal of the Mechanics and Physics of Solids 35, 95-119.

Grady, D., Olsen, M., 2003. A statistics and energy based theory of dynamic fragmentation. International Journal of Impact Engineering 29, 293-306.

Grant, N.C., Cooper, A.I., Zhang, H., 2010. Uploading and Temperature-Controlled Release of Polymeric Colloids via Hydrophilic Emulsion-Templated Porous Polymers. ACS Applied Materials & Interfaces 2, 1400-1406.

Hakamada, M., Mabuchi, M., 2007. Mechanical strength of nanoporous gold fabricated by dealloying. Scripta Materialia 56, 1003-1006.

Haller, W., 1965. Chromatography on glass of controlled pore size.

Hartmann, K.-H., Kunze, H.-D., Meyer, L., 1981. Metallurgical effects on impact loaded materials, Shock waves and high-strain-rate phenomena in metals. Springer, pp. 325-337.

Hayes, J.R., Nyce, G., Kuntz, J., Satcher, J., Hamza, A., 2007. Synthesis of bi-modal nanoporous Cu, CuO and Cu_2O monoliths with tailored porosity. Nanotechnology 18, 275602.

Hedrick, J.L., Carter, K.R., Labadie, J.W., Miller, R.D., Volksen, W., Hawker, C.J., Yoon, D.Y., Russell, T.P., McGrath, J.E., Briber, R.M., 1999. Nanoporous Polyimides, in: Kricheldorf, H.R. (Ed.), Progress in Polyimide Chemistry II. Springer Berlin Heidelberg, pp. 1-43.

Hill, R., 1962. Acceleration waves in solids. Journal of the Mechanics and Physics of Solids 10, 1-16.

Hodge, A.M., Hayes, J.R., Caro, J.A., Biener, J., Hamza, A.V., 2006. Characterization and Mechanical Behavior of Nanoporous Gold. Advanced Engineering Materials 8, 853-857.

Huang, H.-Y., Lin, C.-L., Wu, C.-Y., Cheng, Y.-J., Lin, C.-H., 2013. Metal organic framework–organic polymer monolith stationary phases for capillary electrochromatography and nano-liquid chromatography. Analytica Chimica Acta 779, 96-103.

Huang, R., Suo, Z., Prevost, J., Nix, W., 2002. Inhomogeneous deformation in metallic glasses. Journal of the Mechanics and Physics of Solids 50, 1011-1027.

Hutchinson, J.W., 2000. Plasticity at the micron scale. International Journal of Solids and Structures 37, 225-238.

Iler, R.K., 1979. The chemistry of silica: solubility, polymerization, colloid and surface pro perties, and biochemistry. Wiley.

Jennings, A.T., Burek, M.J., Greer, J.R., 2010. Microstructure versus Size: Mechanical Properties of Electroplated Single Crystalline Cu Nanopillars. Physical Review Letters 104, 135503.

Jiang, M., Wang, W., Dai, L., 2009. Prediction of shear-band thickness in metallic glasses. Scripta Materialia 60, 1004-1007.

Jiang, W., Atzmon, M., 2006. Mechanically-assisted nanocrystallization and defects in amorphous alloys: A high-resolution transmission electron microscopy study. Scripta materialia 54, 333-336.

Johnson, G.R., Cook, W.H., 1983. A constitutive model and data for metals subjected to large strains, high strain rates and high temperatures, Proceedings of the 7th International Symposium on Ballistics. The Netherlands, pp. 541-547.

Kanazawa, T., Matsuda, Y., Tasaka, S., 2010. Fabrication of a porous structure of poly (tetrafluoroethylene) from a mixture with fumaric acid. Polymer journal.

Kawaguchi, T., Iura, J., Taneda, N., Hishikura, H., Kokubu, Y., 1986. Structural changes of monolithic silica gel during the gel-to-glass transition. Journal of Non-Crystalline Solids 82, 50-56.

Kaye, G.W.C., Laby, T.H., 1921. Tables of physical and chemical constants: and some mathematical functions. Longmans, Green and Company.

Ketov, S., Louzguine-Luzgin, D., 2013. Localized shear deformation and softening of bulk metallic glass: stress or temperature driven? Scientific reports 3.

Kiefer, W., Sura, M., 1986. Heating mixture of sinterable, leachable material, sintering, cooling, and leaching. Google Patents.

Kim, K., Das, J., Lee, M., Yi, S., Fleury, E., Zhang, Z., Wang, W., Eckert, J., 2008. Propagation of shear bands in a $Cu_{47.5}Zr_{47.5}Al_5$ bulk metallic glass. Journal of Materials Research 23, 6-12.

Kinslow, R., 2012. High-velocity impact phenomena. Elsevier.

Klopp, R., Clifton, R., Shawki, T., 1985. Pressure-shear impact and the dynamic viscoplastic response of metals. Mechanics of Materials 4, 375-385.

Kolsky, H., 1963. Stress waves in solids. Courier Corporation.

Kostyukov, N., 1991. Physical causes and mechanisms of the formation of boundary regions in the two-dimensional explosive compaction of powdered materials. Journal of applied mechanics and technical physics 32, 967-973.

Kusubov, A., Nesterenko, V., Wilkins, M., Resugh, J., 1989. Dynamic deformation of powdered materials as a function of particle size, Proceedings of International Seminar on High Energy Working of Rapidly Solidified and High-Temperature Superconducting Materials, p. 139.

Lee, J.-H., Wang, L., Kooi, S., Boyce, M.C., Thomas, E.L., 2010. Enhanced Energy Dissipation in Periodic Epoxy Nanoframes. Nano Letters 10, 2592-2597.

Leonard, A., Daraio, C., 2012. Stress Wave Anisotropy in Centered Square Highly Nonlinear Granular Systems. Physical Review Letters 108, 214301.

Leventis, N., Sotiriou-Leventis, C., Zhang, G., Rawashdeh, A.-M.M., 2002. Nanoengineering Strong Silica Aerogels. Nano Letters 2, 957-960.

Levitz, P., Ehret, G., Sinha, S.K., Drake, J.M., 1991. Porous vycor glass: The microstructure as probed by electron microscopy, direct energy transfer, small-angle scattering, and molecular adsorption. The Journal of Chemical Physics 95, 6151-6161.

Lu, G., Yu, T., 2003. Energy absorption of structures and materials. Elsevier.

Luo, J., Stevens, R., 1999. Porosity-dependence of elastic moduli and hardness of 3Y-TZP ceramics. Ceramics International 25, 281-286.

Mühlhaus, H., Vardoulakis, I., 1987. The thickness of shear bands in granular materials. Geotechnique 37, 271-283.

Mackenzie, J., 1964. High-pressure Effects on Oxide Glasses: III, Densification in Nonrigid State. Journal of the American Ceramic Society 47, 76-80.

Marchand, A., Duffy, J., 1988. An experimental study of the formation process of adiabatic shear bands in a structural steel. Journal of the Mechanics and Physics of Solids 36, 251-283.

Masumoto, T., Maddin, R., 1971. The mechanical properties of palladium 20 a/o silicon alloy quenched from the liquid state. Acta metallurgica 19, 725-741.

Md Jani, A.M., Losic, D., Voelcker, N.H., 2013. Nanoporous anodic aluminium oxide: Advances in surface engineering and emerging applications. Progress in Materials Science 58, 636-704.

Me-Bar, Y., Shechtman, D., 1983. On the adiabatic shear of Ti_6Al_4V ballistic targets. Materials Science and Engineering 58, 181-188.

Meyer, L., Staskewitsch, E., Burblies, A., 1994. Adiabatic shear failure under biaxial dynamic compression/shear loading. Mechanics of materials 17, 203-214.

Meyers, M.A., 1994. Dynamic behavior of materials. John Wiley & Sons.

Meyers, M.A., Chawla, K.K., 2009. Mechanical behavior of materials. Cambridge university press Cambridge.

Meyers, M.A., Murr, L.E., 1981. Shock waves and high-strain-rate phenomena in metals, Proc. Int. Conf. on Metallurgical Effects of High-Strain-Rate and Fabrication, Plenum Press, New York.

Meyers, M.A., Murr, L.E., Staudhammer, K.P., 1992. Shock-wave and high-strain-rate phenomena in materials. CRC.

Meyers, M.A., Nesterenko, V.F., LaSalvia, J.C., Xue, Q., 2001. Shear localization in dynamic deformation of materials: microstructural evolution and self-organization. Materials Science and Engineering: A 317, 204-225.

Meyers, M.A., Subhash, G., Kad, B.K., Prasad, L., 1994. Evolution of microstructure and shear-band formation in α-hcp titanium. Mechanics of Materials 17, 175-193.

Meyers, M.A., Xu, Y.B., Xue, Q., Pérez-Prado, M.T., McNelley, T.R., 2003. Microstructural evolution in adiabatic shear localization in stainless steel. Acta Materialia 51, 1307-1325.

Minakuchi, H., Nakanishi, K., Soga, N., Ishizuka, N., Tanaka, N., 1996. Octadecylsilylated porous silica rods as separation media for reversed-phase liquid chromatography. Analytical chemistry 68, 3498-3501.

Mishra, A., Martin, M., Thadhani, N., Kad, B., Kenik, E.A., Meyers, M., 2008. High-strain-rate response of ultra-fine-grained copper. Acta materialia 56, 2770-2783.

Misra, A., Greer, J.R., Daraio, C., 2009. Strain Rate Effects in the Mechanical Response of Polymer-Anchored Carbon Nanotube Foams. Advanced Materials 21, 334-338.

Miyamoto, R., Ando, Y., Kurusu, C., Bai, H.z., Nakanishi, K., Ippommatsu, M., 2013. Fabrication of large-sized silica monolith exceeding 1000 mL with high structural homogeneity. Journal of separation science 36, 1890-1896.

Nakanishi, K., 1997. Pore structure control of silica gels based on phase separation. Journal of Porous Materials 4, 67-112.

Nakanishi, K., 2010. Synthesis Concepts and Preparation of Silica Monoliths, Monolithic Silicas in Separation Science: Concepts, Syntheses, Characterization, Modeling and Applications. John Wiley & Sons, p. 11.

Nemat-Nasser, S., Isaacs, J.B., Starrett, J.E., 1991. Hopkinson techniques for dynamic recovery experiments. Proceedings of the Royal Society of London. Series A: Mathematical and Physical Sciences 435, 371-391.

Nesterenko, V., 1994. Localization of deformation in collapse of a thick walled cylinder. Combustion, Explosion and Shock Waves 30, 500-509.

Nesterenko, V., Daraio, C., Herbold, E., Jin, S., 2005a. Anomalous wave reflection at the interface of two strongly nonlinear granular media. Physical review letters 95, 158702.

Nesterenko, V., Lazaridi, A., Pershin, S., 1989. Localization of deformation in copper by explosive compression of hollow cylinders. Fizika Goreniya i Vzryva 25, 154e155.

Nesterenko, V., Luk'yanov, Y.L., Bondar', M., 1994a. Deformation of the contact zone in the formation of a "cold" boundary layer. Combustion, Explosion, and Shock Waves 30, 693-695.

Nesterenko, V., Meyers, M., Chen, H., 1996. Shear localization in high-strain-rate deformation of granular alumina. Acta materialia 44, 2017-2026.

Nesterenko, V., Meyers, M., LaSalvia, J., Bondar, M., Chen, Y., Lukyanov, Y., 1997. Shear localization and recrystallization in high-strain, high-strain-rate deformation of tantalum. Materials Science and Engineering: A 229, 23-41.

Nesterenko, V.F., 2001. Dynamics of heterogeneous materials. Springer Science & Business Media.

Nesterenko, V.F., Bondar, M.P., Ershov, I.V., 1994b. Instability of plastic flow at dynamic pore collapse. AIP Conference Proceedings 309, 1173-1176.

Nesterenko, V.F., Daraio, C., Herbold, E.B., Jin, S., 2005b. Anomalous Wave Reflection at the Interface of Two Strongly Nonlinear Granular Media. Physical Review Letters 95, 158702.

Nevejans, F., Verzele, M., 1985. Swelling propensity (SP factor) of semi-rigid chromatographic packing materials. Journal of Chromatography A 350, 145-150.

Nordborg, A., Svec, F., Fréchet, J.M.J., Irgum, K., 2005. Extending the array of crosslinkers suitable for the preparation of polymethacrylate-based monoliths. Journal of Separation Science 28, 2401-2406.

Nyce, G.W., Hayes, J.R., Hamza, A.V., Satcher, J.H., 2007. Synthesis and characterization of hierarchical porous gold materials. Chemistry of materials 19, 344-346.

Otsu, N., 1975. A threshold selection method from gray-level histograms. Automatica 11, 23-27.

Pauly, S., Gorantla, S., Wang, G., Kühn, U., Eckert, J., 2010. Transformation-mediated ductility in CuZr-based bulk metallic glasses. Nature Materials 9, 473-477.

Pekarskaya, E., Kim, C., Johnson, W., 2001. In situ transmission electron microscopy studies of shear bands in a bulk metallic glass based composite. Journal of Materials Research 16, 2513-2518.

Penner, N.A., Nesterenko, P.N., Ilyin, M.M., Tsyurupa, M.P., Davankov, V.A., 1999. Investigation of the properties of hypercrosslinked polystyrene as a stationary phase for high-performance liquid chromatography. Chromatographia 50, 611-620.

Peters, E.C., Svec, F., Fréchet, J.M.J., 1997. Preparation of Large-Diameter "Molded" Porous Polymer Monoliths and the Control of Pore Structure Homogeneity. Chemistry of Materials 9, 1898-1902.

Pinto, J., Dumon, M., Pedros, M., Reglero, J., Rodriguez-Perez, M.A., 2014. Nanocellular CO_2 foaming of PMMA assisted by block copolymer nanostructuration. Chemical Engineering Journal 243, 428-435.

Pirard, R., Alie, C., Pirard, J.-P., 2005. Specific behavior of sol-gel materials in mercury porosimetry: collapse and intrusion. Handbook of Sol-Gel Science and Technology. Volume II: Characterization of Sol-Gel materials and Products, 211-233.

Poirier, J., 1980. Shear localization and shear instability in materials in the ductile field. Journal of Structural Geology 2, 135-142.

Porter, M.A., Daraio, C., Szelengowicz, I., Herbold, E.B., Kevrekidis, P., 2009. Highly nonlinear solitary waves in heterogeneous periodic granular media. Physica D: Nonlinear Phenomena 238, 666-676.

Queheillalt, D.T., Wadley, H.N., 2005. Cellular metal lattices with hollow trusses. Acta Materialia 53, 303-313.

Rahman, T., Liu, R., Ortel, E., Kraehnert, R., Antoniou, A., 2014. Mechanical behavior of mesoporous titania thin films. Applied Physics Letters 104, -.

Rao, C.R., Govindaraj, A., 2011. Nanotubes and nanowires. Royal Society of Chemistry.

Recht, R., 1964. Catastrophic thermoplastic shear. Journal of Applied Mechanics 31, 189-193.

Reddy, K.M., Liu, P., Hirata, A., Fujita, T., Chen, M.W., 2013. Atomic structure of amorphous shear bands in boron carbide. Nat Commun 4.

Reinhardt, B., Enke, D., Syrowatka, F., 2012. Preparation of Porous, Hierarchically Organized Glass Monoliths via Combination of Sintering and Phase Separation. Journal of the American Ceramic Society 95, 461-465.

Ren, Z.F., Huang, Z.P., Xu, J.W., Wang, J.H., Bush, P., Siegal, M.P., Provencio, P.N., 1998. Synthesis of Large Arrays of Well-Aligned Carbon Nanotubes on Glass. Science 282, 1105-1107.

Reyes-Aldasoro, C.C., 2009. Retrospective shading correction algorithm based on signal envelope estimation. Electronics letters 45, 454-456.

Rice, J.R., 1976. The localization of plastic deformation. Division of Engineering, Brown University.

Ritchie, R.O., 2011. The conflicts between strength and toughness. Nat Mater 10, 817-822.

Roscoe, K.H., 1970. The influence of strains in soil mechanics. Geotechnique 20, 129-170.

Scheffler, M., Colombo, P., 2006. Cellular ceramics: structure, manufacturing, properties and applications. John Wiley & Sons.

Scheve, J., 1982. Poröse Gläser Herstellung, Eigenschaften und Anwendung Von F. Janowski und W. Heyer; Leipzig, VEB Deutscher Verlag für Grundstoffindustrie 1982; 274 Seiten mit 77 Bildern und 32 Tabellen; Format 14,5 × 21,5 cm; Pappband 48,– M Bestell-Nr.: 5416958. Zeitschrift für Chemie 22, 396-396.

Schmid, G., Bäumle, M., Geerkens, M., Heim, I., Osemann, C., Sawitowski, T., 1999. Current and future applications of nanoclusters. Chemical Society Reviews 28, 179-185.

Schmidt, M., Schwertfeger, F., 1998. Applications for silica aerogel products. Journal of Non-Crystalline Solids 225, 364-368.

Schnabel, R., Langer, P., 1991. Controlled-pore glass as a stationary phase in chromatography. Journal of Chromatography A 544, 137-146.

Semiatin, S., Staker, M., Jonas, J., 1984. Plastic instability and flow localization in shear at high rates of deformation. Acta metallurgica 32, 1347-1354.

Sen, S., Hong, J., Bang, J., Avalos, E., Doney, R., 2008. Solitary waves in the granular chain. Physics Reports 462, 21-66.

Shih, C., Meyers, M., Nesterenko, V., 1998a. High-strain-rate deformation of granular silicon carbide. Acta materialia 46, 4037-4065.

Shih, C., Nesterenko, V., Meyers, M., 1998b. High-strain-rate deformation and comminution of silicon carbide. Journal of applied physics 83, 4660-4671.

Shoup, R.D., 1976. Controlled pore silica bodies gelled from silica sol-alkali silicate mixtures, in: Kerker, M. (Ed.), Colloid and Interface Science. Academic Press, New York, pp. 63-69.

Shoup, R.D., Wein, W.J., 1980. Method of making controlled-pore silica structures for high temperature insulation. Google Patents.

Song, B., Chen, W., 2004. Loading and unloading split Hopkinson pressure bar pulse-shaping techniques for dynamic hysteretic loops. Experimental Mechanics 44, 622-627.

Song, B., Chen, W., 2006. Energy for specimen deformation in a split Hopkinson pressure bar experiment. Experimental mechanics 46, 407-410.

Spaepen, F., 1977. A microscopic mechanism for steady state inhomogeneous flow in metallic glasses. Acta metallurgica 25, 407-415.

Spaepen, F., 2006. Metallic glasses: Must shear bands be hot? Nature Materials 5, 7-8.

Starosvetsky, Y., Vakakis, A.F., 2010. Traveling waves and localized modes in one-dimensional homogeneous granular chains with no precompression. Physical Review E 82, 026603.

Surani, F.B., Kong, X., Panchal, D.B., Qiao, Y., 2005. Energy absorption of a nanoporous system subjected to dynamic loadings. Applied Physics Letters 87, 163111.

Svec, F., Fréchet, J.M., 1992. Continuous rods of macroporous polymer as high-performance liquid chromatography separation media. Analytical Chemistry 64, 820-822.

Svec, F., Frechet, J.M., 1995. Kinetic control of pore formation in macroporous polymers. Formation of" molded" porous materials with high flow characteristics for separations or catalysis. Chemistry of materials 7, 707-715.

Tan, P., Reid, S., Harrigan, J., Zou, Z., Li, S., 2005. Dynamic compressive strength properties of aluminium foams. Part I—experimental data and observations. Journal of the Mechanics and Physics of Solids 53, 2174-2205.

Tappan, B.C., Huynh, M.H., Hiskey, M.A., Chavez, D.E., Luther, E.P., Mang, J.T., Son, S.F., 2006. Ultralow-Density Nanostructured Metal Foams: Combustion Synthesis, Morphology, and Composition. Journal of the American Chemical Society 128, 6589-6594.

Tappan, B.C., Steiner, S.A., Luther, E.P., 2010. Nanoporous Metal Foams. Angewandte Chemie International Edition 49, 4544-4565.

Tejchman, J., Wu, W., 1993. Numerical study on patterning of shear bands in a Cosserat continuum. Acta Mechanica 99, 61-74.

Theocharis, G., Boechler, N., Kevrekidis, P.G., Job, S., Porter, M.A., Daraio, C., 2010. Intrinsic energy localization through discrete gap breathers in one-dimensional diatomic granular crystals. Physical Review E 82, 056604.

Timothy, S.P., Hutchings, I.M., 1985. The structure of adiabatic shear bands in a titanium alloy. Acta Metallurgica 33, 667-676.

Tokudome, Y., Fujita, K., Nakanishi, K., Miura, K., Hirao, K., 2007. Synthesis of monolithic Al_2O_3 with well-defined macropores and mesostructured skeletons via the sol-gel process accompanied by phase separation. Chemistry of materials 19, 3393-3398.

Treacy, M.M.J., Ebbesen, T.W., Gibson, J.M., 1996. Exceptionally high Young's modulus observed for individual carbon nanotubes. Nature 381, 678-680.

Vlakh, E.G., Tennikova, T.B., 2013. Flow-through immobilized enzyme reactors based on monoliths: I. Preparation of heterogeneous biocatalysts. Journal of Separation Science 36, 110-127.

Vukovic, I., Brinke, G.t., Loos, K., 2013. Block copolymer template-directed synthesis of well-ordered metallic nanostructures. Polymer 54, 2591-2605.

Walsh, D., Arcelli, L., Ikoma, T., Tanaka, J., Mann, S., 2003. Dextran templating for the synthesis of metallic and metal oxide sponges. Nat Mater 2, 386-390.

Washburn, E.W., 1921. The Dynamics of Capillary Flow. Physical Review 17, 273-283.

Wolfgang, H., 1970. Material and method for performing steric separations. Google Patents.

Wright, W.J., Hufnagel, T., Nix, W., 2003. Free volume coalescence and void formation in shear bands in metallic glass. Journal of applied physics 93, 1432-1437.

Wu, B., Heidelberg, A., Boland, J.J., 2005. Mechanical properties of ultrahigh-strength gold nanowires. Nat Mater 4, 525-529.

Xie, S., Svec, F., Fréchet, J.M.J., 1997. Rigid porous polyacrylamide-based monolithic columns containing butyl methacrylate as a separation medium for the rapid hydrophobic interaction chromatography of proteins. Journal of Chromatography A 775, 65-72.

Xin, P., Qi, L., Zhang, R., Yao, C., Wei, X., Yang, G., Chen, Y., 2010. Well-defined skeletal macroporous polymer monoliths fabricated with a novel type of amphiphilic diblock copolymer as a phase separator. Polymer 51, 3410-3415.

Xu, Y., Zhang, J., Bai, Y., Meyers, M.A., 2008. Shear localization in dynamic deformation: microstructural evolution. Metallurgical and materials transactions A 39, 811-843.

Xu, Y.B., Zhong, W.L., Chen, Y.J., Shen, L.T., Liu, Q., Bai, Y.L., Meyers, M.A., 2001. Shear localization and recrystallization in dynamic deformation of 8090 Al–Li alloy. Materials Science and Engineering: A 299, 287-295.

Xue, Q., Meyers, M., Nesterenko, V., 2002. Self-organization of shear bands in titanium and Ti–6Al–4V alloy. Acta materialia 50, 575-596.

Xue, Q., Nesterenko, V., Meyers, M., 2003. Evaluation of the collapsing thick-walled cylinder technique for shear-band spacing. International journal of impact engineering 28, 257-280.

Yang, C., Wei, Y., Zhang, Q., Zhang, W., Li, T., Hu, H., Zhang, Y., 2005. Preparation and evaluation of a large-volume radial flow monolithic column. Talanta 66, 472-478.

Zener, C., Hollomon, J.H., 1944. Effect of Strain Rate Upon Plastic Flow of Steel. Journal of Applied Physics 15, 22-32.

Zhou, M., Rosakis, A., Ravichandran, G., 1996. Dynamically propagating shear bands in impact-loaded prenotched plates—I. Experimental investigations of temperature signatures and propagation speed. Journal of the Mechanics and Physics of Solids 44, 981-1006.

Zukas, J., 1982. Impact dynamics. John Wiley & Sons, Inc, 605 Third Ave, New York, N. Y. 10158, U. S. A, 1982. 452.

Zurek, A.K., 1994. The study of adiabatic shear band instability in a pearlitic 4340 steel using a dynamic punch test. Metallurgical and Materials Transactions A 25, 2483-2489.